Photosensitizer Activation by Ionizing Radiation

Bing Xu 徐冰

Photosensitizer Activation by Ionizing Radiation

Photosensitizer Activation by Ionizing Radiation

Dissertation

For the purpose of obtaining the degree of doctor
at Delft University of Technology,
by the authority of the Rector Magnificus Prof.dr.ir. H. Bijl,
chair of the Board for Doctorates,
to be defended publicly on
Friday 8 May 2026 at 10:00 am

by

Bing XU

This dissertation has been approved by the promotors.

Composition of the doctoral committee:

Rector Magnificus,	Chairperson
Prof.dr.ir. A.G. Denkova	Delft University of Technology, promotor
Prof.dr. R. Eelkema	Delft University of Technology, promotor

Independent members:

Prof.dr. L.D.A. Siebbeles	Delft University of Technology
Prof.dr. H.T. Wolterbeek	Delft University of Technology
Prof.dr. D.W.P.M. Löwik	Radboud University
Dr. K. Djanashvili	Delft University of Technology
Dr. S. van Lith	Radboud University Medical Center

The research presented in this thesis was performed in the Applied Radiation and Isotopes section of the department of Radiation Science and Technology and the Advanced Soft Matter group of the department of Chemical Engineering, Faculty of Applied Sciences, Delft University of Technology, the Netherlands. This research was funded by the China Scholarship Council (CSC No. 202106920019)

Cover designed by vgen@Mooi_Fei (mszhaoyw@gmail.com)
Printed by Proefschriftspecialist

ISBN 978-94-6518-305-3

Printed in the Netherlands

长风破浪会有时

A time will come to ride the wind and cleave the waves

— 李白

CONTENTS

SUMMARY

Radiation therapy uses ionizing radiation to kill tumor cells by damaging DNA and other biomolecules either directly or via reactive oxygen species generated during water radiolysis. However, radiation effectiveness is often limited by normal tissue tolerance and tumor radioresistance, which motivates the use of radiosensitizers to enhance tumor response. Photosensitizers are being explored as radiosensitizers because they can promote the formation of additional reactive oxygen species and other reactive species under ionizing radiation. However, the mechanisms by which photosensitizers respond to ionizing radiation remain unclear, and reported radiosensitizing outcomes are not always consistent. This thesis therefore investigates the mechanism of how photosensitizers generate reactive oxygen species under different radiation conditions and assesses their potential as radiosensitizers across radiation therapy modalities with different dose rates.

Based on earlier observations that Chlorin e6 can generate singlet oxygen in water under X-ray irradiation, Chapter 2 investigates how radiation energy and dose rate influence singlet oxygen formation, and the possible mechanism of the activation. We found that singlet oxygen formation increased with total dose, but the increase was disproportionate to dose rate, with lower dose rates producing more singlet oxygen. Comparing radiation energies under conditions where Cerenkov light emission is expected or absent showed that Cerenkov light is not essential for singlet oxygen generation. Scavenger experiments further demonstrated that radiation generated superoxide anions participate in singlet oxygen formation. Taken together, these results suggest an ionization driven mechanism in which radiation ionizes the photosensitizer to form a radical cation, which then oxidizes superoxide anions to produce singlet oxygen.

Nevertheless, an alternative mechanism has also been suggested in which Auger electrons or secondary electrons directly excite photosensitizers and promote singlet oxygen formation. We therefore tested this possibility for Chlorin e6 *in vitro* by using iodine-125 (^{125}I) radiolabeled gold nanoparticles to create a high Auger electron density region near the nanoparticle surface and attached Chlorin e6 there. We found that attaching Chlorin e6 to the nanoparticle surface did not lead to cell killing. In contrast, simply mixing ^{125}I radiolabeled nanoparticles with Chlorin e6 achieved a clear increase in cell killing. These results indicate that direct excitation of Ce6 is unlikely under these conditions.

After establishing that radiation conditions like dose rate influence singlet oxygen formation at the mechanistic level, Chapters 4 and 5 address a clinically relevant question of how dose rate changes the radiosensitizing behavior of photosensitizer based strategies, especially in settings relevant to brachytherapy and radionuclide therapy. Because Chlorin e6 has limited tumor selectivity, the thesis shifts to 5-aminolevulinic acid (5-ALA), which is converted intracellularly into an endogenous protoporphyrin IX that can accumulate in certain tumor cells. In Chapter 4, an yttrium-90 foil is used to deliver low dose rates and the combined treatment in glioblastoma and prostate cancer cell lines is evaluated. We found that the radiosensitizing effect seen under conventional external beam irradiation (X-ray, 1.5 Gy/min) also applies for ^{90}Y at 2 Gy/h, but progressively diminishes as the dose rate decreases further (1 Gy/h to 0.3 Gy/h).

Chapter 5 extends the dose rate range below 2 Gy/h down to 0.05 Gy/h using the radionuclide lutetium-177 (^{177}Lu). We used Monte Carlo simulations to convert ^{177}Lu activity into dose and dose rate. The radiosensitizing effect of 5-ALA was evaluated using a 2D clonogenic survival assay and 3D spheroid growth models in prostate cancer cells. In the 2D clonogenic assay, we found a clear inverse dose rate dependence, with 5-ALA enhancing ^{177}Lu induced cell killing only at dose rates below 0.1 Gy/h, while no radiosensitizing effect was observed at dose rates above 2 Gy/h. In preliminary 3D spheroid experiments, the combination of ^{177}Lu and 5-ALA reduced spheroid growth compared with ^{177}Lu alone at selected activity levels.

Overall, this thesis links mechanistic insights to the radiobiological response of photosensitizer mediated radiosensitization. We proposed an ionization-driven mechanism where singlet oxygen forms when photosensitizer radical cations react with superoxide anions, and singlet oxygen formation was enhanced at low dose rates. However, photosensitizer mediated radiosensitization in cells did not fully follow this low dose rate dependence, likely because dose rate also changes cellular defense and repair responses. These results provide guidance for applying photosensitizers as radiosensitizers and show that dose rate is a key factor to consider when designing treatment strategies.

SAMENVATTING

Bij radiotherapie wordt ioniserende straling gebruikt om tumorcellen te doden door het beschadigen van DNA en andere biomoleculen via directe interacties of via reactieve radicalen die tijdens waterradiolyse worden gegenereerd. De effectiviteit van de bestraling wordt echter vaak gelimiteerd door de stralingsresistentie van tumoren en een beperkte tolerantie van normaal weefsel, wat aanleiding geeft tot het gebruik van stralingssensibilisatoren ter verbetering van de tumorrespons. Fotosensibilisatoren worden onderzocht als radiosensibilisatoren omdat ze onder ioniserende straling de vorming van meer radicalen kunnen bevorderen. De mechanismen waarmee fotosensibilisatoren op ioniserende straling reageren, blijven echter onduidelijk en de gerapporteerde resultaten op het gebied van radiosensibilisatie zijn niet altijd consistent. In dit proefschrift wordt daarom onderzocht hoe fotosensibilisatoren onder verschillende stralingsomstandigheden reactieve deeltjes genereren en wordt hun potentieel als radiosensibilisatoren bij verschillende vormen van radiotherapie met verschillende dosissen beoordeeld.

Op basis van eerdere waarnemingen waaruit blijkt dat Chlorin e6 bij blootstelling aan röntgenstraling singletzuurstof in water kan genereren, onderzoekt hoofdstuk 2 hoe stralingsenergie en dosistempo de vorming van singletzuurstof beïnvloeden en wat het mogelijke mechanisme van de activering is. We ontdekten dat de vorming van singletzuurstof toenam met de totale dosis, maar dat de toename niet propotioneel was met het dosistempo: bij lagere dosistempi werd meer singletzuurstof geproduceerd. Uit een vergelijking van bestralingsenergieën onder omstandigheden waarin Cerenkov-lichtemissie wordt verwacht of afwezig is, bleek dat Cerenkov-licht niet essentieel is voor de vorming van singletzuurstof. Scavenger-experimenten toonden verder aan dat door straling gegenereerde superoxide-anionen deelnemen aan de vorming van singletzuurstof. Samen suggereren deze resultaten een door ionisatie aangedreven mechanisme waarbij straling de fotosensibilisator ioniseert om een radicaal kation te vormen, dat vervolgens superoxide-anionen oxideert om singletzuurstof te produceren.

Er is echter ook een alternatief mechanisme voorgesteld, waarbij Auger-elektronen of secundaire elektronen fotosensibilisatoren direct exciteren en de vorming van singletzuurstof bevorderen. We hebben deze mogelijkheid daarom getest voor Chlorin e6 *in vitro*, waarbij we met jodium-125 (^{125}I) radioactief gelabelde gouden nanodeeltjes hebben gebruikt om een gebied met een hoge Auger-elektronendichtheid te creëren nabij het oppervlak van de

nanodeeltjes en daar Chlorin e6 aan hebben gehecht. We ontdekten dat het hechten van Chlorin e6 aan het oppervlak van de nanodeeltjes niet leidde tot celdood. Daarentegen leidde het eenvoudig mengen van ^{125}I radioactief gelabelde nanodeeltjes met Chlorin e6 tot een duidelijke toename in celdood. Deze resultaten geven aan dat directe excitatie van Chlorin e6 onder onze omstandigheden onwaarschijnlijk is.

Nadat is vastgesteld dat stralingsomstandigheden zoals dosistempo de vorming van singletzuurstof op mechanistisch niveau beïnvloeden, behandelen hoofdstukken 4 en 5 een klinisch relevante vraag, namelijk hoe dosistempo het radiosensibiliserende gedrag van op fotosensibilisatoren gebaseerde strategieën verandert, met name in situaties die relevant zijn voor brachytherapie en radionuclidetherapie. Omdat Chlorin e6 een beperkte tumorselectiviteit heeft, verschuift de focus van het proefschrift naar 5-aminolevulinezuur (5-ALA), dat intracellulair wordt omgezet in een endogeen protoporfyrine dat zich in bepaalde tumorcellen kan ophopen. In hoofdstuk 4 wordt een yttrium-90 folie gebruikt om lage dosistempi toe te dienen en wordt de gecombineerde behandeling in glioblastoom- en prostaatkankercellijnen geëvalueerd. We hebben vastgesteld dat het radiosensibiliserende effect dat wordt waargenomen bij conventionele externe bestraling (röntgenstraling, 1,5 Gy/min) ook geldt voor ^{90}Y bij 2 Gy per uur, maar geleidelijk afneemt naarmate het dosistempo verder daalt (1 Gy/h tot 0,3 Gy/h).

Hoofdstuk 5 breidt het dosistempo bereik verder uit tot zeer lage dosistempi met behulp van lutetium-177 (^{177}Lu). Met behulp van Monte Carlo-simulaties hebben we de activiteit van ^{177}Lu omgerekend naar dosis en dosistempo. Het radiosensibiliserende effect van 5-ALA werd geëvalueerd met behulp van een clonogene test en driedimensionale sferoïde groeimodellen in prostaatkankercellen. In de clonogene test werd een duidelijke omgekeerde dosistempoafhankelijkheid waargenomen, waarbij 5-ALA de door ^{177}Lu geïnduceerde celdoding alleen versterkte bij dosissnelheden onder 0,1 Gy per uur.

Over het geheel genomen koppelt dit proefschrift mechanistische inzichten aan de radiobiologische respons van door fotosensibilisatoren gemedieerde radiosensibilisatie. We stellen een door ionisatie aangestuurd mechanisme voor waarbij singletzuurstof wordt gevormd wanneer radicale kationen van fotosensibilisatoren reageren met superoxide-anionen. Daarnaast tonen de resultaten aan dat dosistempo een belangrijke factor is bij het ontwerpen van radiotherapieën.

Chapter 1

Introduction

1.1 Radiation Therapy

Cancer remains a leading cause of death around the world, with about 20 million new cases and 10 million deaths each year.[1] Traditional cancer treatments involve surgery, radiotherapy and systemic therapy (e.g., chemotherapy and hormonal treatment). The selection of treatment regimen is based on both the characteristics of the cancer and the individual patient, with the primary goal being either to cure the disease, to prolong survival or to alleviate discomfort. Radiation therapy (RT), as one of the primary modalities in cancer treatment, employs high-energy radiation to eliminate or shrink malignant tumors while preserving surrounding healthy tissue. Currently, RT plays a crucial role in the management of more than half of all cancer patients, either as a standalone treatment or combined with other therapeutic approaches.[2,3]

1.1.1 Overview

RT is generally categorized into two main modalities: external beam radiation therapy (EBRT) and internal radiation therapy (Fig. 1.1).[4] EBRT delivers targeted radiation from outside the body, making it the standard treatment for locally advanced solid tumors such as head and neck, breast, and lung cancers. The radiation used in EBRT includes photons, electrons and heavy charged particles. Photon radiation, comprising X-rays (generated by linear accelerators) and gamma rays (typically from ^{60}Co), represents the most widely used modality due to its deep tissue penetration, ease of dose modulation, and widespread availability of treatment infrastructure.[5] Electron beams are employed for superficial lesions due to their limited penetration depth and sharp dose fall-off beyond the target.[6] Charged particle therapy, including protons and carbon ions, offers highly localized dose delivery for deep-seated tumors through the Bragg peak effect but remains confined to specialized centers due to their high cost and complex equipment.[7]

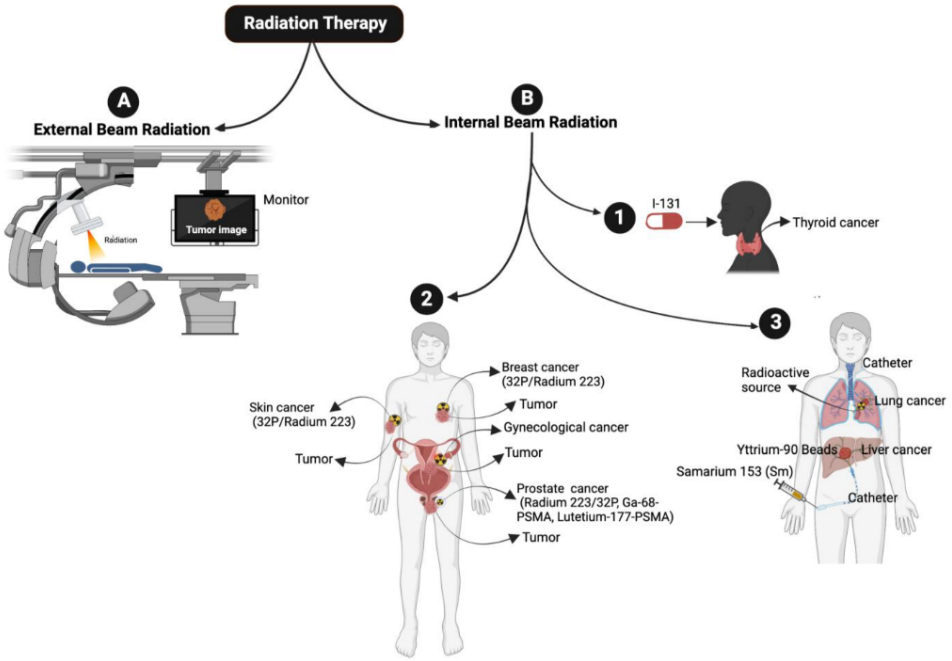

Figure 1.1. Classification of radiation therapy modalities: external beam radiation therapy (A), radionuclide therapy (B1-2), and brachytherapy (B3). Reproduced from Reference 4.

Internal radiation therapy comprises two main approaches: brachytherapy (BT) and radionuclide therapy (RNT). Both modalities use radioisotopes as radiation sources. BT involves placing encapsulated radioactive sources near or directly within the tumor. In BT, radionuclides that emit low-energy radiation with a steep dose fall-off are preferred, as they enable localized high-dose delivery while minimizing exposure to surrounding healthy tissues. Low-energy photon emitters are commonly employed in clinical practice. For example, iodine-125 (^{125}I) and cesium-131 (^{131}Cs) are used in permanent implants for prostate and cervical cancers and for recurrent malignant neoplasms, respectively.[8-10] Iridium-192 (^{192}Ir), in contrast, is used in temporary BT for the treatment of prostate and head and neck cancers.[11] Beta-minus emitters (β^-) are also utilized in specialized applications, for example yttrium-90 (^{90}Y), a high-energy β^- emitter, has been applied in the form of glass or resin microspheres for radioembolization of hepatocellular carcinoma[12,13], and is under investigation for brain tumors[14]. Radionuclide therapy (RNT) utilizes systemically administered radiopharmaceuticals for cancer treatment. Iodine-131 (^{131}I) is the most widely used radionuclide in RNT, particularly for treating thyroid cancer due to the specific uptake of iodine by thyroid tissue.[15]

For the treatment of metastatic tumors, radionuclides are typically conjugated to targeting moieties via carrier molecules. In such cases, the most extensively used radionuclide is lutetium-177 (^{177}Lu). Radiopharmaceuticals such as [^{177}Lu]Lu-DOTATATE and [^{177}Lu]Lu-PSMA-617 have been used for the treatment of neuroendocrine tumors and metastatic prostate cancer, respectively.[16,17]

1.1.2 Dose delivery and dose rate differences

While EBRT and internal radiation therapy share the common goal of tumor eradication through ionizing radiation, they differ in how radiation is delivered to target tissues and the resulting dose rate differences (Table 1.1). EBRT administers radiation in fractions, typically 1.8 to 2 Gy per session delivered over several weeks to achieve cumulative doses from 35 up to 80 Gy depending on the treatment plan.[18] This fractionation strategy takes advantage of the different recovery rates between tumor and normal tissues, helping to reduce adverse side effects. During each treatment session, EBRT maintains a constant dose rate, generally ranging from 0.1 to 10 Gy/min, depending on the accelerator specifications and delivery technique.[19]

BT has two general modalities: high-dose-rate BT (HDR-BT) and low-dose-rate BT (LDR-BT). HDR-BT is typically delivered as a boost treatment in conjunction with EBRT, with radiation administrated in fractions (3 to 15 Gy per fraction) over weeks at dose rates exceeding 12 Gy/h.[20] Due to the high dose rate and fractionated dose delivery, the radiobiological effects of HDR-BT are comparable to those of EBRT. LDR-BT involves permanent seeds implantation and delivers doses of more than 100 Gy over the complete physical decay of the radionuclide at an initial dose rate lower than 2 Gy/h.[21]

RNT involves the most complex mode of dose delivery, as it is governed by both pharmacokinetic behavior and radioactive decay. The absorbed dose distribution depends on the temporal biodistribution of the radiopharmaceutical, its retention in tumor and normal tissues, and the physical decay properties of the radionuclide. For example, in ^{177}Lu-based therapies, patients typically receive about 7.4 GBq per cycle over four to six administrations at roughly two-month intervals, with reported tumor absorbed doses ranging from approximately 1.4 to 14.5 Gy/GBq per cycle.[22-25] However, unlike the relatively uniform dose distributions achieved in EBRT and HDR-BT, RNT shows strong dose heterogeneity due to variations in radiopharmaceutical tumor uptake and retention, making the dose rate difficult to define precisely.

Table 1.1. *Modalities, radiation dose distribution and dose rate variations in the different radiation therapies*

Modalities	Source example	Energy	Approximate Dose	(Initial) Dose rate
EBRT	Photons, electrons, protons	4-25 MV, X-rays 4-250 MV, protons 1.17 and 1.33 MeV, γ-rays	1.8-2 Gy per fraction, ~ 80 Gy	0.1-10 Gy/min
HDR-BT	^{192}Ir	0.397 MeV (average)	3-15 Gy per fraction, ~ 50 Gy	> 12 Gy/h
LDR-BT	^{125}I, ^{137}Cs	< 0.03 MeV (average)	Over 100 Gy	0.4-2 Gy/h
RNT	^{177}Lu	0.149 MeV (average)	~ 10 to 40 Gy per cycle, up to 6 cycles	~0.1 Gy/h

1.1.3 Challenges of radiation therapy

Although radiation therapy (RT) is recognized as an effective cancer treatment, several physical and biological factors limit its efficiency in achieving optimal tumor control. RT techniques all rely on ionizing radiation to damage cancer cells, yet each modality faces distinct clinical challenges arising from differences in dose distribution, dose rate, and surrounding healthy tissue tolerance. Most clinically used radiation types, such as photons and β^- particles, have low linear energy transfer (LET). LET describes the energy deposited per unit distance along the particle track. Low-LET radiation produces sparse ionization events rather than dense ionization tracks, which makes it less effective at inducing complex DNA damage in tumor cells. In EBRT or HDR-BT, the total dose is often constrained by the tolerance of surrounding normal tissues, which prevents dose escalation to resistant tumor regions. LDR-BT delivers radiation continuously at a low dose rate, potentially allowing tumor cells to repair sublethal DNA damage during treatment.[26] In radionuclide therapy (RNT), the non-uniform distribution of radiopharmaceuticals results in heterogeneous dose delivery within the tumor, where some regions may receive insufficient radiation dose, reducing overall tumor control.[27] These limitations are especially challenging for radioresistant tumors, which require higher doses for better therapeutic outcomes and are typically able to recover from radiation damage. In such cases treatment can fail and also lead to tumor recurrence.

Therefore, developing effective radiosensitizers is necessary and essential to enhance the efficacy of RT without harming surrounding healthy tissue, especially those with minimal systemic toxicity yet capable of enhancing radiation-induced tumor damage. This thesis is

therefore related to the use of such compounds, specifically photosensitizers (PSs), and aims to unravel their mechanisms and explore their potential application as radiosensitizers in different modalities of RT.

1.2 Radioresistance and radiosensitizers

Before investigating how PSs interact with ionizing radiation and function as radiosensitizer, it is essential to first understand how ionizing radiation damages tumor cells, how these cells resist to such damage, and how radiosensitizers can be strategically employed to enhance therapeutic efficacy.

1.2.1 From ionizing radiation events to cellular damage

Ionizing radiation interacts with matter through two primary mechanisms, depending on the type of radiation. For charged particles, including electrons (or positrons), protons and α particles, interactions with matter primarily occur through electrostatic forces, undergoing both elastic and inelastic collisions with the atoms or molecules in the medium. Inelastic collisions dominate the overall energy loss process, transferring energy to orbital electrons and leading to ionization or excitation.[28] Photons, however, interact with matter through the photoelectric effect, Compton scattering, or pair production, depending on the atomic number of the medium and the photon energy. Through these processes, the photon transfers its energy to electrons bound to atoms in the medium, ejecting them from their shells. The ejected electrons then lose their kinetic energy through further ionization and excitation of surrounding atoms or molecules.[29] In biological systems, these physical interactions may cause the direct ionization of DNA, generating radical cations and anions on its backbone and bases. These reactive intermediates can subsequently trigger strand breaks or chemical modifications, leading to both structural and functional damage to the DNA.[30,31] The number of direct ionization events in DNA strongly depends on the LET of the radiation, with high LET creates more ionizing events (Fig. 1.2(a)). However, since low-LET radiations such as X-rays, γ-rays, and β^- particles are most commonly used in radiotherapy, the contribution of direct DNA damage is considerably less than that of indirect damage arising from reactive species produced during water radiolysis in cells.[32]

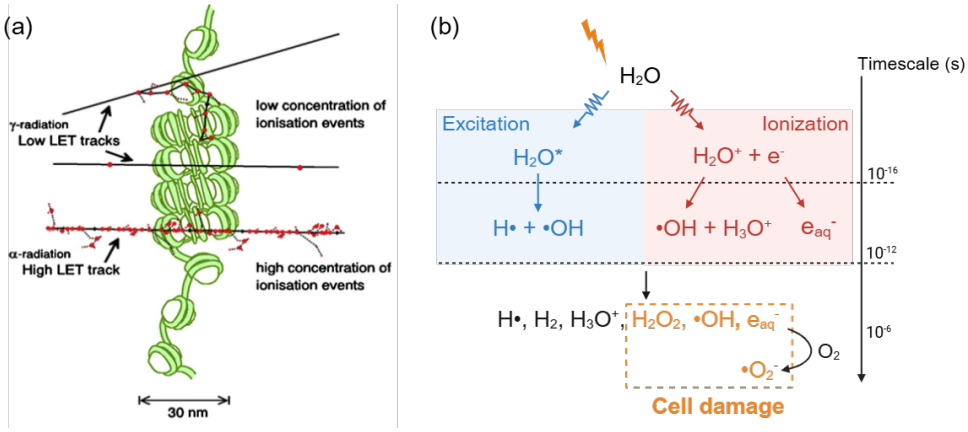

Figure 1.2. (a) Spatial distribution of ionization events (red dots) caused by a single radiation track at low and high LET in relation to DNA. Reproduced from Reference 32. (b) The time scale of water radiolysis at low LET and biological effects. Adapted from References 32-34.

When ionizing radiation interacts with water, it produces both excited and ionized water molecules together with ejected secondary electrons. These short-lived species rapidly undergo reorganization that trigger a series of subsequent chemical reactions. As a result, a variety of reactive species such as hydrated electrons (e_{aq}^-), hydroxyl radicals (·OH), hydrogen radicals (·H), and hydrogen peroxide (H_2O_2) are formed.[33] In aerobic biological environments, e_{aq}^- rapidly react with dissolved molecular oxygen to generate superoxide anions ($\cdot O_2^-$). Consequently, the major reactive oxygen species (ROS) accounting for cellular damage are mainly $\cdot O_2^-$, ·OH and H_2O_2 (Fig. 1.2(b)), which can destroy cellular components, particularly DNA.[34] Ionizing radiation can also activate cellular nitric oxide synthase (NOS), leading to the production of nitric oxide (·NO), which can further react with $\cdot O_2^-$ to form the highly reactive peroxynitrite anion ($ONOO^-$) that can attack biomolecules.[35] In addition, organic radicals (R·) can also be formed. These carbon-centered radicals could react with oxygen to form peroxyl radicals ($RO_2\cdot$) and abstract hydrogen from neighboring molecules, initiating chain reactions such as lipid peroxidation and protein oxidation that amplify radiation-induced oxidative damage.[36] The extent of these reactive species formation is dependent on the LET of radiation, with high-LET generally producing more reactive species. These direct and indirect induced damage by ionizing radiation is responsible for cell death.

1.2.2 Mechanisms of radioresistance and development of radiosensitizers

Radioresistance

Radioresistance arises from a combination of cellular repair capacity, redox regulation, metabolic adaptation and microenvironmental factors (Fig. 1.3).[37,38] The therapeutic effect of radiotherapy depends largely on radiation-induced biomolecular damage and oxidative stress, yet tumor cells activate multiple mechanisms to resist these effects. After irradiation, DNA repair pathways are rapidly engaged, and checkpoint signaling is activated to maintain genome stability through homologous recombination or non-homologous end joining. In many tumors, however, defects in DNA repair also allow damaged DNA to bypass checkpoint control, enabling replication of mutated genomes and promoting long-term radioresistance.[39] Among different forms of radiation damage, double-strand breaks (DSBs) are the most severe and the hardest to repair. Low-LET radiation can also induce DSBs, but these breaks are usually isolated and therefore more easily controlled, which limits the cytotoxicity of low-LET radiation compared with high-LET modalities that generate clustered and complex DSBs.[32]

Tumor cells also strengthen their antioxidant systems by upregulating enzymes such as superoxide dismutase, catalase and glutathione peroxidase to neutralize excess ROS.[40] Metabolic reprogramming helps to maintain redox balance, as tumor cells may reduce mitochondrial respiration or shift toward glycolytic metabolism to limit ROS generation. This metabolic shift also provides biosynthetic precursors and energy that support rapid proliferation and tumor growth.[41,42] Repeated irradiation can further promote radioresistance by inducing cellular plasticity and generating cancer stem cell-like populations with stronger survival abilities. The tumor microenvironment also plays an important role. Hypoxic regions weaken the oxygen enhancement effect and make tumor cells less sensitive to radiation.[43]

These mechanisms together limit the efficiency of low-LET radiation, making the use of radiosensitizers important for improving cellular sensitivity.

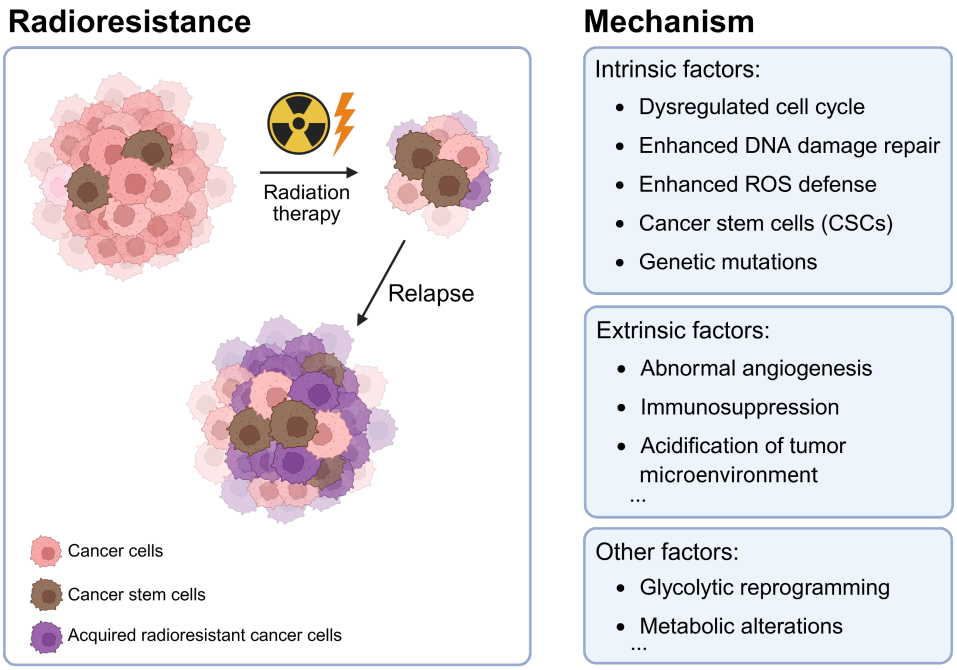

Figure 1.3. An Overview of mechanisms involved in tumor radioresistance. Adapted from Reference 38.

Radiosensitizer

Radiosensitizers are agents designed to enhance the sensitivity of tumor cells to ionizing radiation. Currently, clinically investigated radiosensitizers are largely repurposed chemotherapeutic agents or drugs originally developed for non-radiation-related indications (Table 1.2). These compounds increase radiation response by impairing DNA repair, modulating tumor oxygenation, or disrupting antioxidant defenses (Fig. 1.3). Despite these mechanistic advantages, their clinical translation has been limited by substantial systemic toxicity, poor tumor selectivity, and narrow therapeutic windows.[44] In addition, many patients have contraindications or limited treatment tolerance, making them unsuitable for enhanced therapy with radiosensitizers having high systemic toxicity.

Table 1.2. *Ongoing Clinical Trials of Radiosensitizers, Reproduced from Reference 44.*

Identifier	Drug	Conditions	Phase	Initiation
NCT02757651	Hydrogen peroxide	Breast cancer	I/II	January 2017
NCT01850563	Hyperbaric oxygen	Brain metastases	Proof of principle	May 2013
NCT01880359	Nimorazole	HNSCC (human papillomavirus negative)	III	July 2014
NCT00301379	5-FU	Cholangiocarcinoma	III	August 2005
NCT02189109	NVX-108 (perfluorocarbon dodecafluoropentane)	Glioblastoma multiforme	I	May 2014
NCT02229656	Olaparib	Head and neck cancer	I	February 2014
NCT02363829	Nelfinavir	Uterine cervix cancer	I	February 2015
NCT01781403	Temozolomide	Rectal cancer	I	May 2013
NCT02724618	Curcumin	Prostate cancer	II	March 2016
NCT01068327	Nelfinavir mesylate	Stage III pancreatic cancer	I	November 2007
NCT01684904	Paclitaxel	Esophageal cancer	II	July 2012
NCT03066154	Docetaxel	Prostatic neoplasms	I	September 2016
NCT02871843	RRx-001	Glioblastoma	I	February 2017
NCT03101995	Gemcitabine	Cervical cancer	II	July 2017

Materials that are used to boost the damage from ionizing radiation have also been developed, including high atomic number (Z) nanoparticles such as hafnium oxide[45], gadolinium[46], and gold[47]. Their higher cross section compared with water allows them to absorb more energy from radiation and deposit higher dose to cells. However, translating nanoparticles into clinical practice remains challenging because of concerns about potential long-term toxicity.

Because of these limitations, there is an increasing interest in radiosensitizers that do not lead to short- or long-term toxicity. Photosensitizers (PSs), originally developed for photodynamic therapy (PDT), have gained attention because they can generate additional ROS not only initiated by light but also when exposed to ionizing radiation, making them promising candidates for enhancing radiation response. Their safety profile further supports their application in cancer treatment. PSs are already clinically approved for PDT and have been used in patients for many years. They show minimal systemic toxicity at the concentrations relevant for radiation treatment and have a certain degree of tumor selectivity, especially compared with many conventional radiosensitizers that have lower tumor uptake and often cause substantial adverse side effects. Their radiosensitizing effects have already been observed in patients with recurrent tumors, and ongoing clinical studies continue to support their potential integration into radiotherapy.

1.3 Photosensitizer as radiosensitizer

The use of photosensitizers as radiosensitizers can be traced back to around 1955, when hematoporphyrin was combined with radiotherapy to treat patients with recurrent tumors and showed encouraging results. Since then, research in this field has gradually developed, but the working mechanism of photosensitizer excitation by ionizing radiation remains unclear. Considering the fact that reported patient outcomes tend to vary, treatment optimizations is essential and that would require a deeper understanding of the mechanism behind the activation of photosensitizers by ionizing radiation. This leads to the central question of this thesis: how photosensitizers generate ROS during ionizing radiation, and how this process can be used to improve different modalities of radiotherapy. Before addressing this question, this section will first introduce the basic photochemical properties of photosensitizers and then summarize the current state of their combination with radiotherapy and the hypotheses regarding their radiosensitizing mechanisms.

1.3.1 Basic principles of photosensitizers

Photosensitizers are molecules that can absorb light and convert this energy into chemical reactions. Tetrapyrrole structures represent the largest group of PSs used in anti-cancer applications because they generally show high singlet oxygen quantum yields compared with many other types of molecules. Tetrapyrrole backbones also occur naturally in several important biomolecules such as heme, chlorophyll and bacteriochlorophyll.[48] Several families of tetrapyrrole-based macrocycles have been developed for research and therapeutic use, including porphyrins, chlorins, bacteriochlorins and phthalocyanines (Fig. 1.4). The central tetrapyrrolic ring is fundamentally important in PS molecules because it forms an extended π conjugated system, in which the π electrons are delocalized over the whole macrocycle. This extensive delocalization enables strong absorption of visible or near-infrared light (400-800 nm), which is crucial for PDT. In addition, the conjugated system contains well-defined electronic energy levels. This means that the delocalized electrons can only transition from the ground state to specific higher-energy states, and each transition requires a photon whose energy precisely matches the energy gap. Photons with much higher or lower energy are therefore not absorbed efficiently.

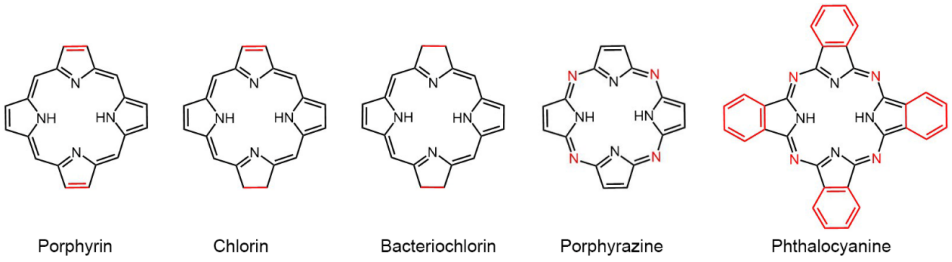

Figure 1.4. Molecular structure of tetrapyrrole-based photosensitizers.

The PS molecules are stable in the dark and remain in the ground singlet state, in which the two electrons in a single frontier orbital have opposite spins. After absorbing photon of certain energy, one electron is promoted to a higher-energy orbital, forming a singlet excited state ($^1PS^*$). This state is very unstable and short-lived (nanoseconds), and it usually returns to the ground state by fluorescence emission. However, the singlet excited state can also undergo intersystem crossing to form a triplet excited state ($^3PS^*$). The $^3PS^*$ contains two electrons with parallel spins, and it has a much longer lifetime (microseconds) because the return of these parallel-spin electrons to the singlet ground state is a spin-forbidden process under quantum selection rules. As a result, the $^3PS^*$ has enough time to transfer its energy to surrounding molecular oxygen (O_2), producing singlet oxygen ($^1O_2$).[49] This process, known as the Type II pathway, is the dominant mechanism responsible for cell damage in PDT. The $^3PS^*$ can also gain or lose an electron to form a radical cation or radical anion. The best-studied pathway (Type I) is the reaction of the radical anion with O_2 to generate $\cdot O_2^-$.[50,51] Though $\cdot O_2^-$ has relatively low reactivity in biological systems, it can undergo dismutation or one-electron reduction to form H_2O_2, which can then undergo further one-electron reduction to produce $\cdot OH$ (Fig. 1.5). These ROS and $^1O_2$ can damage cellular structures, including lipids, proteins, and DNA, ultimately leading to cell death.[52,53]

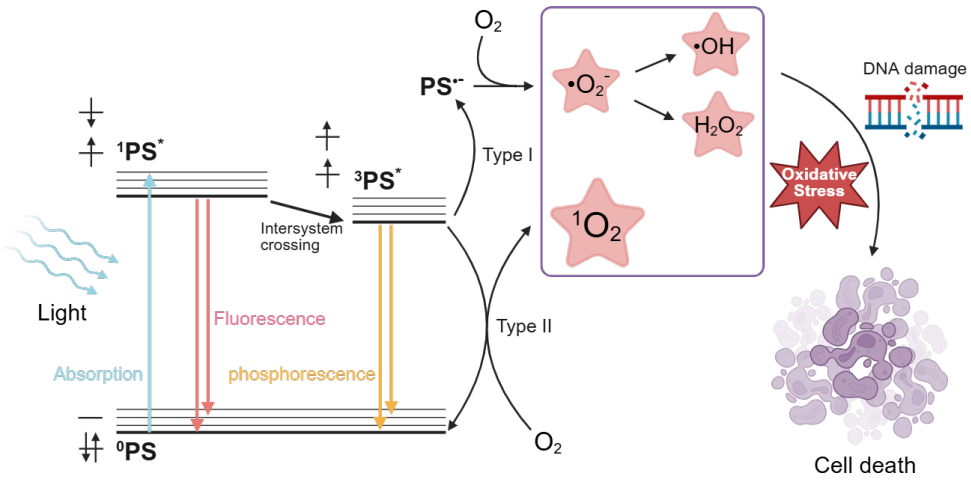

Figure 1.5. Mechanistic illustration of the photochemical behavior of photosensitizers and their associated cell-killing effects. Adapted from Reference 49.

1.3.2 Current research on PS as radiosensitizers

Clinical research

Clinical research on photosensitizers as radiosensitizers has progressed slowly, and only a small number of clinical studies have been conducted so far, although interest in this approach has been growing in recent years. Most of these clinical attempts have been performed in combination with external photon beam radiation therapy, using several porphyrin-based agents as the sensitizing compounds. Among them, hematoporphyrin, porfimer sodium (Photofrin II) and 5-aminolevulinic acid (5-ALA) have received the most clinical attention. The first clinical study of hematoporphyrin was reported by Schwartz et al. in 1955, in which 38 patients with resistant or inoperable tumors received hematoporphyrin together with X-rays at dose rates between approximately 0.1 and 2.9 Gy/min or with ^{60}Co γ-rays.[54] Tumor reduction was observed in 13 of 38 patients, with squamous-cell carcinoma and rhabdomyosarcoma showing marked responses, while melanoma showed no improvement. Between 2002 and 2006, Schaffer and colleagues reported case observations in 17 patients with advanced cancer disease who received external beam radiotherapy, including one patient with oropharyngeal carcinoma treated with brachytherapy.[55,56] Partial or complete remissions occurred in several tumor types, including pelvic sarcoma, cervical cancer, astrocytoma and bladder cancer, although the approach was not effective in recurrent glioblastoma or in oropharyngeal carcinoma.

More recently, renewed attention has been directed to 5-ALA, a precursor of mitochondrial

protoporphyrin IX with selective accumulation in brain tumors. A phase I clinical trial was initiated at the Fox Chase Cancer Center in 2020 that enrolled 130 patients with various tumor types in order to determine tolerated doses of 5-ALA in combination with radiotherapy.[57] In addition, a phase I and II clinical study led by Stummer at the University Hospital Münster is currently investigating 34 patients with recurrent glioblastoma. This trial evaluates repeated and dose escalated administration of 5-ALA together with conventional radiotherapy, with the primary aim of assessing tolerability and identifying an optimal administration schedule for future clinical studies.[58]

Clinical studies of photosensitizers as radiosensitizers have shown encouraging tumor responses in some cases, yet failures have also been reported. Because the number of treated patients remains small and randomized trials are lacking, the overall evidence is still inconclusive. The variable outcomes among tumor types suggest possible tumor-specific behavior, which may relate to the uptake or distribution of photosensitizers in patients. Moreover, failure also often reflects the limitations of radiotherapy itself, including tumor hypoxia, antioxidant responses and the scavenging of radicals generated during irradiation. These observations indicate that important clinical questions still remain regarding how this treatment combination can be effectively implemented.

Preclinical research

Beyond clinical studies, this combined treatment has received extensive attention in preclinical research. A range of porphyrins (free-base or metal-based) and texaphyrins have been investigated and shown positive results in both *in vitro* and *in vivo* across different tumor types. A detailed summary can be found in the review by Leo et. al.,[59] and here we focus on the main research aspects investigated in these preclinical studies.

Preclinical research has generally approached this combined treatment from a practical perspective. First, different photosensitizers have been tested across various tumor types including glioblastoma, breast, colorectal, cervical, lung, and prostate cancers.[60-65] Most studies confirmed the radiosensitizing role of PSs, though the strength of the observed effects varied with tumor type, which again may reflect the differences in intrinsic radioresistance. For example, glioblastoma U87 showed improved radiosensitivity when treated with 5-ALA combined with fractionated radiation in mouse models.[63,66] However, in glioblastoma stem cells (a highly radioresistant population) or giant cell glioblastoma, 5-ALA shows no radiosensitizing effect.[58] Second, concentration-dependence of PSs has been investigated, as a threshold concentration is typically required for radiosensitization.[67] Third, given that hypoxia

is a common tumor characteristic, the oxygen-dependence of radiosensitization has been examined. In vitro studies showed that Photofrin II produces radiosensitizing effects at 21% oxygen but not at 5%, and verteporfin similarly loses its effect under hypoxic conditions.[68,69] In contrast, 5-ALA-induced PpIX can maintain radiosensitizing effects in hypoxia.[70] However, whether the presence of oxygen truly enhances the intrinsic radiosensitizing capability of PSs remains uncertain. The difficulty comes from the fact that hypoxia itself increases tumor radioresistance, which makes it hard to distinguish whether the reduced effect is caused by a loss of PS function or simply by the reduced radiation effectiveness in hypoxic environment. The fact that 5-ALA localizes mainly in the mitochondria, which is an important site of radiation-induced damage, also plays an important role.

Both kilovoltage X-rays in the range of 50 to 220 kV and megavoltage photons can trigger radiosensitization. Studies using lower energy typically employed fractionated irradiation, whereas MeV beams often produced radiosensitizing effects with a single dose. Some explanations attribute this difference to Cerenkov light, since its emission falls within the absorption range of many photosensitizers which is between 400 and 800 nm.[71-73] However, comparative studies have not shown a clear difference between kV and MV irradiation in terms of the overall radiosensitizing effect, which makes the contribution of Cerenkov light uncertain.[74] At present, internal radiation has received much less attention compared with external beam studies. Brachytherapy has been examined as one of the internal radiation approaches. Photofrin II was tested with ^{192}Ir in adenocarcinoma tumors, and the treatment was delivered at a low dose rate of about 1 Gy/h. Under these conditions, no radiosensitizing effect was observed.[75] Radionuclides have also been explored. For example, the combination of ^{64}Cu with 5-ALA significantly decreased breast cancer cell viability and produced tumor remission in mouse models.[65] Although these observations were attributed to Cerenkov light, the actual amount of light emitted by ^{64}Cu (~0.56 Cerenkov photons/decay) is negligible compared with the deposited radiation energy, which raises questions on the role of Cerenkov radiation.[76]

Although these studies cover a wide range of topics and provide many useful observations, the research directions are highly scattered and the results are not always consistent. This makes it difficult to draw clear conclusions from preclinical work alone and raises the need to examine the mechanism of photosensitizer activation by ionizing radiation.

Mechanistic insights

Currently, there are generally three hypotheses regarding the ROS formation by PSs when exposed to ionizing radiation. The first involves Cerenkov light produced when the radiation energy exceeds the threshold required for its generation. Cerenkov light is considered to function as an internal light source that can excite PSs to the triplet state, leading to the production of ROS. The second hypothesis suggests that PSs can be directly excited by secondary electrons generated during the interaction of radiation with matter.[77] The third proposes an indirect pathway in which ionizing radiation produces ionized PS species that promote electron transfer to surrounding substrates and generate ROS. This process does not rely on the traditional photochemical pathway through which photosensitizers are usually excited.[59] While these hypotheses outline possible routes for ROS formation, there is no direct evidence for any of them and much remains to be understood.

Although many questions regarding the radiosensitizing effect of photosensitizers still need to be answered, the main starting point of this thesis is:

- To better understand the mechanism behind ionizing radiation induced activation of photosensitizers.
- To determine which radiation modalities are best suited for the activation of photosensitizers in biologically relevant environment such as 2D or 3D cell cultures.

1.4 Outline of the thesis

The aim of this thesis is to investigate how photosensitizers respond when ionizing radiation interacts with these molecules in aqueous solutions, and how these mechanistic insights can help to further develop the combination with radiation therapy. We primarily used X-rays and gamma rays to study the interaction mechanisms between photosensitizers and ionizing radiation. Based on our hypothesis, we then applied iodine-125, yttrium-90 and lutetium-177 as radiation sources in combination with photosensitizers to treat cancer cells, assessing whether the proposed mechanism also operates in biological environment.

In **Chapter 2**, we examine how radiation conditions influence singlet oxygen formation by Chlorin e6 (Ce6) in aqueous solutions and aimed at interpreting the underlying mechanism. We compared singlet oxygen production when exposed to photon beams with different energies, including energies not leading to Cerenkov emission and energies capable of producing Cerenkov light. Singlet Oxygen Sensor Green (SOSG) and the imidazole/RNO method were used to detect singlet oxygen formation. In addition to energy differences, we also evaluated dose rate effects similar to those used in external beam radiation therapy and brachytherapy. To further support the interpretation of the activation mechanism, we performed scavenger experiments assessing the contribution of different reactive species to the overall singlet oxygen production process by Ce6.

In **Chapter 3**, we investigate whether photosensitizers are activated through direct electronic excitation. We used an iodine-125(^{125}I) system that provides Auger electrons and photon emissions to create different electron environments around Chlorin e6. Gold nanoparticles were introduced as a platform to position Ce6 at defined distances from ^{125}I. Cytotoxicity was used as the main approach to evaluate how these different electron environments influence the activation process and to determine the function of Ce6.

In **Chapter 4**, we apply an yttrium-90 foil to mimic the dose rate of brachytherapy and investigate how dose rate influences the radiosensitizing behavior of 5-ALA in glioblastoma U87 cells and in the prostate cancer cell line PIP-PC3. The evaluation mainly focuses on changes in cell proliferation after combined treatment.

In **Chapter 5**, we further examine the dose rate effect on the radiosensitizing behavior of 5-ALA in PIP-PC3 cells using the radionuclide lutetium-177. The activity-to-dose and dose rate were estimated through Monte Carlo simulations. To assess the response to this combined treatment, we performed 2D clonogenic assays and 3D spheroid experiments.

In **Chapter 6**, the conclusions are presented based on the understanding gained from the results and finish with an outlook for future research directions in this field.

References

1 Bray, F., Laversanne, M., Sung, H., Ferlay, J. *et al.* Global cancer statistics 2022: GLOBOCAN estimates of incidence and mortality worldwide for 36 cancers in 185 countries. *CA: A Cancer Journal for Clinicians* **74**, 229-263 (2024).

2 Maria, D. L. O., Cao, M., Cai, B., Cummings, M. & Zheng, D. Adaptive Radiotherapy: Next-Generation Radiotherapy. *Cancers* **16**, 1206 (2024).

3 Karaca, S. & Bölükbaş, M. K. Time Matters: A Review of Current Radiotherapy Practices and Efficiency Strategies. *Technology in Cancer Research & Treatment* **24**, 15330338251345376 (2025).

4 Boopathi, E., Den, R. B. & Thangavel, C. Innate Immune System in the Context of Radiation Therapy for Cancer. *Cancers* **15**, 3972 (2023).

5 Koka, K., Verma, A., Dwarakanath, B. S. & Papineni, R. V. L. Technological Advancements in External Beam Radiation Therapy (EBRT): An Indispensable Tool for Cancer Treatment. *Cancer Management and Research* **14**, 1421-1429 (2022).

6 Locke, J., Karimpour, S., Young, G., Lockett, M. A. & Perez, C. A. Radiotherapy for epithelial skin cancer. *International Journal of Radiation Oncology, Biology, Physics* **51**, 748-755 (2001).

7 Durante, M. & Flanz, J. Charged particle beams to cure cancer: Strengths and challenges. *Seminars in Oncology* **46**, 219-225 (2019).

8 Pickett, B. & Pouliot, J. The effect of the radial function on I-125 seeds used for permanent prostate implantation. *Medical Dosimetry* **29**, 204-209 (2004).

9 Jiang, P., Zou, L., Wei, L., Cheng, G. *et al.* Chinese Expert Consensus on Iodine^{125} Seed Implantation for Recurrent Cervical Cancer in 2021. *Frontiers in Oncology* **11**, 700710 (2021).

10 Palmisciano, P., Haider, A. S., Balasubramanian, K., Boockvar, J. A. *et al.* Cesium-131 brachytherapy for the treatment of brain metastases: Current status and future perspectives. *Journal of Clinical Neuroscience* **109**, 57-63 (2023).

11 Richard T. Hoppe, Theodore Locke Phillips & Roach, M. *Leibel and Phillips Textbook of Radiation Oncology: Chapter 14 - High Dose Rate Brachytherapy*. 14 (Elsevier Health Science, 2010).

12 Sangro, B., Carpanese, L., Cianni, R., Golfieri, R. *et al.* Survival after Yttrium-90 resin microsphere radioembolization of hepatocellular carcinoma across Barcelona clinic liver cancer stages: A European evaluation. *Hepatology* **54**, 868-878 (2011).

13 Salem, R., Thurston, K. G., Carr, B. I., Goin, J. E. & Geschwind, J.-F. H. Yttrium-90 Microspheres: Radiation Therapy for Unresectable Liver Cancer. *Journal of Vascular and Interventional Radiology* **13**, S223-S229 (2002).

14 Pasciak, A. S., Manupipatpong, S., Hui, F. K., Gainsburg, L. *et al.* Yttrium-90 radioembolization as a possible new treatment for brain cancer: proof of concept and safety analysis in a canine model. *EJNMMI Research* **10**, 96 (2020).

15 Szumowski, P., Abdelrazek, S., Iwanicka, D., Mojsak, M. *et al.* Dosimetry during adjuvant ^{131}I therapy in patients with differentiated thyroid cancer-clinical implications. *Scientific Reports* **11**, 13930 (2021).

16 Hofman, M. S., Violet, J., Hicks, R. J., Ferdinandus, J. *et al.* [^{177}Lu]-PSMA-617 radionuclide treatment in patients with metastatic castration-resistant prostate cancer (LuPSMA trial): a single-centre, single-arm, phase 2 study. *The Lancet Oncology* **19**, 825-833 (2018).

17 Strosberg, J., El-Haddad, G., Wolin, E., Hendifar, A. *et al.* Phase 3 Trial of ^{177}Lu-Dotatate for Midgut Neuroendocrine Tumors. *The New England journal of medicine* **376**, 125-135 (2017).

18 Xu, X. G., Bednarz, B. & Paganetti, H. A review of dosimetry studies on external-beam radiation treatment with respect to second cancer induction. *Physics in medicine and biology* **53**, R193–R241 (2008).

19 Ling, C. C., Gerweck, L. E., Zaider, M. & Yorke, E. Dose-rate effects in external beam radiotherapy redux. *Radiotherapy and Oncology* **95**, 261-268 (2010).

20 Hoskin, P. J., Rojas, A. M., Bownes, P. J., Lowe, G. J. *et al.* Randomised trial of external beam radiotherapy alone or combined with high-dose-rate brachytherapy boost for localised prostate cancer. *Radiotherapy and Oncology* **103**, 217-222 (2012).

21 Henry, A., Pieters, B. R., André Siebert, F. & Hoskin, P. GEC-ESTRO ACROP prostate brachytherapy guidelines. *Radiotherapy and Oncology* **167**, 244-251 (2022).

22 Violet, J., Jackson, P., Ferdinandus, J., Sandhu, S. *et al.* Dosimetry of ^{177}Lu-PSMA-617 in Metastatic Castration-Resistant Prostate Cancer: Correlations Between Pretherapeutic Imaging and Whole-Body Tumor Dosimetry with Treatment Outcomes. *Journal of Nuclear Medicine* **60**, 517-523 (2019).

23 Sartor, O., De Bono, J., Chi, K. N., Fizazi, K. *et al.* Lutetium-177–PSMA-617 for Metastatic Castration-Resistant Prostate Cancer. *New England Journal of Medicine* **385**, 1091-1103 (2021).

24 Jackson, P., Hofman, M., McIntosh, L., Buteau, J. P. & Kumar, A. R. Radiation Dosimetry in ^{177}Lu-PSMA-617 Therapy. *Seminars in Nuclear Medicine* **52**, 243-254 (2022).

25 Ells, Z., Grogan, T. R., Czernin, J., Dahlbom, M. & Calais, J. Dosimetry of [^{177}Lu]Lu-PSMA–Targeted Radiopharmaceutical Therapies in Patients with Prostate Cancer: A Comparative Systematic Review and Metaanalysis. *Journal of Nuclear Medicine* **65**, 1264-1271 (2024).

26 Mazeron, J., Scalliet, P., Van Limbergen, E. & Lartigau, E. Radiobiology of brachytherapy and the dose-rate effect. *The GEC-ESTRO handbook of brachytherapy. Brussels: ESTRO*, 95-121 (2002).

27 Tamborino, G., Nonnekens, J., De Saint-Hubert, M., Struelens, L. *et al.* Dosimetric Evaluation of the Effect of Receptor Heterogeneity on the Therapeutic Efficacy of Peptide Receptor Radionuclide Therapy: Correlation with DNA Damage Induction and *In Vivo* Survival. *Journal of Nuclear Medicine* **63**, 100-107 (2022).

28 Tandon, P., Prakash, D., Kheruka, S. C. & Bhat, N. N. *Radiation Safety Guide for Nuclear Medicine Professionals*. (Springer Nature Singapore, 2022).

29 Eigen, G. in *Graduate Texts in Physics Interactions of Charged Particles and Photons with Matter and Fields* 43-140 (Springer Nature Switzerland, 2025).

30 Becker, D. & Sevilla, M. D. The Chemical Consequences of Radiation Damage to DNA. *Advances in Radiation Biology* **17**, 121-180 (1993).

31 Ravanat, J.-L. Endogenous natural and radiation-induced DNA lesions: differences and similarities and possible implications for human health and radiological protection. *Radioprotection* **53**, 241-248 (2018).

32 Lomax, M. E., Folkes, L. K. & O'Neill, P. Biological Consequences of Radiation-induced DNA Damage: Relevance to Radiotherapy. *Clinical Oncology* **25**, 578-585 (2013).

33 Jay-Gerin, J.-P. Fundamentals of Water Radiolysis. *Encyclopedia* **5**, 38 (2025).

34 Azzam, E. I., Jay-Gerin, J.-P. & Pain, D. Ionizing radiation-induced metabolic oxidative stress and prolonged cell injury. *Cancer Letters* **327**, 48-60 (2012).

35 Mikkelsen, R. & Wardman, P. Biological chemistry of reactive oxygen and nitrogen and radiation-induced signal transduction mechanisms *Oncogene* **22**, 5734-5754 (2003).

36 Berlett, B. S. & Stadtman, E. R. Protein Oxidation in Aging, Disease, and Oxidative Stress. *Journal of*

Biological Chemistry **272**, 20313-20316 (1997).

37 Busato, F., Khouzai, B. E. & Mognato, M. Biological Mechanisms to Reduce Radioresistance and Increase the Efficacy of Radiotherapy: State of the Art. *International Journal of Molecular Sciences* **23**, 10211 (2022).

38 Rycaj, K. & Tang, D. G. Cancer stem cells and radioresistance. *International Journal of Radiation Biology* **90**, 615-621 (2014).

39 Huang, R.-X. & Zhou, P.-K. DNA damage response signaling pathways and targets for radiotherapy sensitization in cancer. *Signal Transduction and Targeted Therapy* **5**, 265-276 (2020).

40 Nguyen, L., Dobiasch, S., Schneider, G., Schmid, R. M. *et al.* Impact of DNA repair and reactive oxygen species levels on radioresistance in pancreatic cancer. *Radiotherapy and Oncology* **159**, 265-276 (2021).

41 Akhunzianov, A. A., Rozhina, E. V., Filina, Y. V., Rizvanov, A. A. & Miftakhova, R. R. Resistance to Radiotherapy in Cancer. *Diseases* **13**, 22 (2025).

42 Tang, L., Wei, F., Wu, Y., He, Y. *et al.* Role of metabolism in cancer cell radioresistance and radiosensitization methods. *Journal of Experimental & Clinical Cancer Research* **37** (2018).

43 Shiridokht, F., Kehtari, P., Eskandani, M., Farajollahi, A. & Vandghanooni, S. Advancing cancer radiotherapy: Harnessing radiosensitizers and nanotechnology for enhanced tumor control. *International Journal of Pharmaceutics: X* **10**, 100419 (2025).

44 Wang, H., Mu, X., He, H. & Zhang, X.-D. Cancer Radiosensitizers. *Trends in Pharmacological Sciences* **39**, 24-48 (2018).

45 Bonvalot, S., Rutkowski, P. L., Thariat, J., Carrère, S. *et al.* NBTXR3, a first-in-class radioenhancer hafnium oxide nanoparticle, plus radiotherapy versus radiotherapy alone in patients with locally advanced soft-tissue sarcoma (Act.In.Sarc): a multicentre, phase 2–3, randomised, controlled trial. *The Lancet Oncology* **20**, 1148-1159 (2019).

46 Kotb, S., Detappe, A., Lux, F., Appaix, F. *et al.* Gadolinium-Based Nanoparticles and Radiation Therapy for Multiple Brain Melanoma Metastases: Proof of Concept before Phase I Trial. *Theranostics* **6**, 418-427 (2016).

47 Penninckx, S., Heuskin, A.-C., Michiels, C. & Lucas, S. Gold Nanoparticles as a Potent Radiosensitizer: A Transdisciplinary Approach from Physics to Patient. *Cancers* **12**, 2021 (2020).

48 Abrahamse, H. & Hamblin, M. R. New photosensitizers for photodynamic therapy. *Biochemical Journal* **473**, 347-364 (2016).

49 Maldonado-Carmona, N., Ouk, T.-S. & Leroy-Lhez, S. Latest trends on photodynamic disinfection of Gram-negative bacteria: photosensitizer's structure and delivery systems. *Photochemical & Photobiological Sciences* **21**, 113-145 (2022).

50 Ma, J. & Jiang, L. Photogeneration of singlet oxygen ($^1O_2$) and free radicals ($Sen^{\cdot-}$, $O_2^{\cdot-}$) by *tetra*-brominated hypocrellin B derivative. *Free Radical Research* **35**, 767-777 (2001).

51 Baptista, M. S., Cadet, J., Di Mascio, P., Ghogare, A. A. *et al.* Type I and Type II Photosensitized Oxidation Reactions: Guidelines and Mechanistic Pathways. *Photochemistry and Photobiology* **93**, 912-919 (2017).

52 Plaetzer, K., Krammer, B., Berlanda, J., Berr, F. & Kiesslich, T. Photophysics and photochemistry of photodynamic therapy: fundamental aspects. *Lasers in Medical Science* **24**, 259-268 (2009).

53 Przygoda, M., Bartusik-Aebisher, D., Dynarowicz, K., Cieślar, G. *et al.* Cellular Mechanisms of Singlet Oxygen in Photodynamic Therapy. *International Journal of Molecular Sciences* **24**, 16890 (2023).

54 Schwartz, S., Absolon, K. & Vermund, H. Hospital Report Porphyrins, X-Rays and Tumors. *Univ. Minnesota Med. Bull.* **27**, 1-37 (1955).

55 Schaffer, M., Schaffer, P. M., Vogesser, M., Ertl-Wagner, B. *et al.* Application of Photofrin II as a specific radiosensitising agent in patients with bladder cancer—a report of two cases. *Photochemical & Photobiological Sciences* **1**, 686-689 (2002).

56 Schaffer, M., Ertl-Wagner, B., Schaffer, P. M., Kulka, U. *et al.* Feasibility of Photofrin II as a Radiosensitizing Agent in Solid Tumors – Preliminary Results. *Oncologie* **29**, 514-519 (2006).

57 ClinicalTrials.gov Identifier: NCT04381806.

58 ClinicalTrials.gov Identifier: NCT05590689.

59 Leo, S., Gutierrez, N. M. C., Bulin, A.-L., Coll, J.-L. *et al.* The physicochemical and biochemical mechanisms of porphyrinoid-mediated radiodynamic therapy. *European Journal of Medicinal Chemistry* **296**, 117861 (2025).

60 Maesaka, F., Nakai, Y., Yoshida, T., Tomizawa, M. *et al.* 5-Aminolevulinic Acid: A Novel Approach to Improving Radioresistance in Prostate Cancer. *Cancers* **17**, 1286 (2025).

61 Yang, D. M., Cvetkovic, D., Chen, L. & Ma, C. C. Therapeutic effects of in-vivo radiodynamic therapy (RDT) for lung cancer treatment: a combination of 15MV photons and 5-aminolevulinic acid (5-ALA). *Biomedical Physics and Engineering Express* **8**, 6 (2022).

62 Yamada, K., Murayama, Y., Kamada, Y., Arita, T. *et al.* Radiosensitizing effect of 5-aminolevulinic acid in colorectal cancer in vitro and in vivo. *Oncology Letters* **16**, 5132-5138 (2019).

63 Takahashi, J., Nagasawa, S., Doi, M., Takahashi, M. *et al.* In Vivo Study of the Efficacy and Safety of 5-Aminolevulinic Radiodynamic Therapy for Glioblastoma Fractionated Radiotherapy. *International Journal of Molecular Sciences* **22**, 9762 (2021).

64 Takahashi, J., Misawa, M. & Iwahashi, H. Transcriptome Analysis of Porphyrin-Accumulated and X-Ray-Irradiated Cell Cultures under Limited Proliferation and Non-Lethal Conditions. *Microarrays* **4**, 25-40 (2015).

65 Jo, C., Ahn, H., Kim, J. H., Lee, Y. J. *et al.* Cancer therapy by antibody-targeted Cerenkov light and metabolism-selective photosensitization. *Journal of Controlled Release* **352**, 25-34 (2022).

66 Dupin, C., Sutter, J., Amintas, S., Derieppe, M.-A. *et al.* An Orthotopic Model of Glioblastoma Is Resistant to Radiodynamic Therapy with 5-AminoLevulinic Acid. *Cancers* **14**, 4244 (2022).

67 Schaffer, M., Schaffer, P. M., Corti, L., Gardiman, M. *et al.* Photofrin as a specific radiosensitizing agent for tumors: studies in comparison to other porphyrins, in an experimental in vivo model. *Journal of Photochemistry and Photobiology B: Biology* **66**, 157-164 (2002).

68 Schaffer, P., Kulka, U., Ertl-Wagner, B., Hell, R. *et al.* The influence of oxygen on the radiosensitizing activity of Photofrin II and hypericin. *Journal of Porphyrins and Phthalocyanines* **11**, 736-741 (2012).

69 Clement, S., Guller, A., Mahbub, S. B., Goldys, E. M. *et al.* Oxygen-Carrying Polymer Nanoconstructs for Radiodynamic Therapy of Deep Hypoxic Malignant Tumors. *Biomedicines* **9**, 322 (2021).

70 Owari, T., Tanaka, N., Nakai, Y., Miyake, M. *et al.* 5-Aminolevulinic acid overcomes hypoxia-induced radiation resistance by enhancing mitochondrial reactive oxygen species production in prostate cancer cells. *British Journal of Cancer* **127**, 350-363 (2022).

71 Kamkaew, A., Cheng, L., Goel, S., Valdovinos, H. F. *et al.* Cerenkov Radiation Induced Photodynamic Therapy Using Chlorin e6-Loaded Hollow Mesoporous Silica Nanoparticles. *ACS Applied Materials & Interfaces* **8**, 26630-26637 (2016).

72 Li, C., Guo, Y., Sheng, S., C. Lun, M. *et al.* Photodynamic Therapy Excited by Cerenkov Radiation from Cesium-137 Irradiator: In Vitro Studies. *Clinical Oncology and Research*, 1-5 (2020).

73 Spinelli, A. E. & Boschi, F. Photodynamic Therapy Using Cerenkov and Radioluminescence Light. *Frontiers in Physics* **9**, 637120 (2021).

74 Takahashi, J., Murakami, M., Mori, T. & Iwahashi, H. Verification of radiodynamic therapy by medical linear accelerator using a mouse melanoma tumor model. *Scientific Reports* **8**, 2728 (2018).

75 Moradi, A., Hashemi, B. & Hassan, Z. in *IFMBE Proceedings* 141-143 (Springer Berlin Heidelberg, 2009).

76 RK, G., GS, M. & SR, C. Computed Cerenkov luminescence yields for radionuclides used in biology and medicine. *Physics in medicine and biology* **60**, 4263-4280 (2015).

77 Tu, Z., Sang, Z., Xu, Y., Liang, W. *et al.* Porphyrin-Engineered ^{125}I-Nanoseeds as a Prototype for Immunogenic Brachytherapy. *Journal of the American Chemical Society* **147**, 13229–13242 (2025).

Chapter 2

Low-Dose-Rate Ionizing Radiation Increases Singlet Oxygen Production by Photosensitizers

Abstract

Photosensitizers have significant potential as radiosensitizers in cancer treatment, yet the mechanism of ionizing radiation-induced singlet oxygen ($^1O_2$) generation remains unclear. Here, we systematically investigated $^1O_2$ production by the photosensitizer Chlorin e6 (Ce6) using SOSG probe and imidazole/RNO detection methods, evaluating effects of photon energy (X-rays up to 310 kV and ^{60}Co gamma rays at 1.17 and 1.33 MeV), dose, and dose rate. Ce6 produced more $^1O_2$ with increasing photon energy. At 5 Gy, the lowest dose rate (0.005 Gy/min) yielded significantly more $^1O_2$ than higher dose rates (7-0.05 Gy/min). Scavenging experiments identified superoxide anions ($\cdot O_2^-$) as a key intermediate. We propose that, unlike classical triplet-state photosensitization, ionizing radiation induces Ce6 radical cations ($Ce6^{\bullet+}$), which react with radiation-induced $\cdot O_2^-$ to generate $^1O_2$. These findings suggest potential for photosensitizer–radiation combinations in low dose rate therapies, though further biological validation and consideration of tumor redox status are required.

Keywords: photosensitizer, Chlorin e6, radiotherapy, singlet oxygen formation, dose rate, superoxide anions

The Content of this chapter is adapted from:

Xu, B., Liu, J., Eelkema, R. & Denkova, A. G. Low-dose-rate ionizing radiation increases singlet oxygen production by photosensitizers. *Cell Reports Physical Science* **6**, 102976 (2025)

2.1 Introduction

Despite the proven effectiveness of radiation therapy (RT) in cancer treatment,[1-5] tumour recurrence remains a significant clinical challenge.[6,7] Radiosensitizers are commonly used to enhance radiation effects in recurrent tumours.[8,9] Although these agents initially achieve tumour growth delay, their systemic toxicity ultimately limits improvements in overall survival.[10] Photosensitizers (PSs), which are traditionally used in photodynamic therapy (PDT) to generate cytotoxic singlet oxygen ($^1O_2$) and other reactive oxygen species (ROS) upon light activation,[11] have emerged as promising alternatives, offering remarkable potential to enhance radiation effects with minimal toxicity. Early PSs, such as Hematoporphyrin and Photofrin, achieved clinical success in inducing tumour remission when combined with RT, having as only side effect prolonged photosensitivity persisting for months after treatment.[12-17] Recently, 5-aminolevulinic acid (5-ALA) has gained a lot of attention as a precursor that converts intracellularly into protoporphyrin IX (PpIX), the latter selectively accumulating in tumour tissues due to altered heme biosynthesis,[18] thereby reducing systemic phototoxicity and enhancing radiotherapy outcomes. Preclinical studies have established the feasibility of 5-ALA as a radiosensitizer, prompting its clinical translation with ongoing clinical trials focused on evaluating the maximum tolerated dose of 5-ALA.[19-23] However, the fundamental interaction mechanism between ionizing radiation and photosensitizers that is responsible for these results has received limited attention, preventing optimization of the therapeutic outcomes.

Photosensitizers are typically activated by light photons, which excites them to a triplet state and leads to the generation of $^1O_2$ and ROS.[24] However, there is some evidence suggesting that this classical mechanism may not apply under ionizing radiation. For instance, Takahashi's research[25] suggests that under X-ray irradiation, PpIX may generate ROS through a mechanism involving the transfer of radical energies from primary radicals such as hydroxyl radicals (·OH), hydrogen radicals (·H), and hydrated electrons (e_{aq}^-), as well as secondary electrons, to PpIX. Similarly, Schaffer et al.[13] observed comparable biological effects of Photofrin at radiation doses of 5 Gy and 15 Gy, further suggesting that the observed results may not be caused by direct interaction of photosensitizers with radiation, such as photon excitation. Some cell studies have been performed to understand the observed cytotoxicity when using 5-ALA, which suggest that the effects are mediated by enhanced intracellular ROS production, especially superoxide anions ($\cdot O_2^-$) from mitochondrial dysfunction.[26,27] This mechanism is particularly relevant to 5-ALA due to PpIX accumulation in mitochondria. However, direct evidence linking the dysfunction of mitochondria during irradiation in the presence of PSs is

still lacking. In addition, most existing studies have focused on factors such as photon energy or radiation type (photons vs. particles), while the potential influence of dose rate has often been overlooked. Moreover, the diversity of experimental conditions, including cell types, has led to conflicting or non-comparable results. For instance, photons having both keV and MeV energies appear to be able to activate PS,[19,20,22] while some studies attribute the effect to Cerenkov radiation that only occurs at high photon energies,[28,29] as its emission spectrum overlaps with PS absorption wavelengths[30].

In this study, we have systematically investigated the activation of photosensitizers by X-rays and gamma rays, addressing key factors that may influence their behaviour. Specifically, this study considers the energy of photons (below and above the threshold of Cerenkov light production), the effect of dose rate, and the role of free radicals in pure water. Given that $^1O_2$ is recognized as one of the most cytotoxic species,[31] we primarily focus on its formation during ionizing radiation. The photosensitizer Chlorin e6 was chosen due to its better water solubility compared to most porphyrins and previous findings indicating its activation under ionizing radiation.[32]

2.2 Materials and Methods

Materials

Chlorin e6 (Ce6) was purchased from Santa Cruz Biotechnology (#SC-263067, purity > 96%). Singlet Oxygen Sensor Green (SOSG) and p-nitroso-N,N-dimethylaniline (RNO) were purchased from Thermo Fisher Scientific. L-Histidine and Superoxide dismutase (SOD), Aminophenyl Fluorescein Solution (APF) were purchased from Merck Sigma. Ethanol was purchased from Sigma Aldrich. Milli-Q (MQ) water used in these experiments was prepared with in-house Milli-Q system from Merck Millipore.

Radiation Source

The X-rays were generated by the X-ray source Philips MCN 321 with variable-energy X-ray tube. A ^{60}Co source (GC220, Nordion) was used to generate gamma-ray radiation. The dose rates of ^{60}Co were calculated using Fricke dosimetry corrected for the 2,778-day half-life of Cobalt-60.

X-ray and gamma-ray irradiation

For the X-ray irradiation experiments, the samples were positioned on a horizontal platform,

located at a specified distance from the X-ray tube. To achieve various dose rates necessary for the experiment, adjustments were made to the ratio of voltage and current (Table 2.1). The gamma ray irradiation was performed at a dose rate of 9.1 Gy/min and 6.2 Gy/min by placing samples into the sample chamber of the ^{60}Co source.

Table 2.1. *The settings used for delivering 5 Gy by X-ray irradiation*

Energy	310 kV, 12 mA	240 kV, 15 mA	240 kV, 1 mA	240 kV, 1 mA	240 kV, 0.7 mA	240 kV, 1 mA
Dose rate (Gy/min)	7	3	0.195	0.05	0.034	0.005
Distance (cm)	11	21	21	46	46	150
Irradiation time	40 s	1 min 42 s	25 min 38 s	100 min	147 min	16.5 h

Reactive oxygen species (ROS) measurement

Singlet oxygen ($^1O_2$) formation was confirmed by two established methods. The first method employed the SOSG probe, which exhibits high selectivity for singlet oxygen detection. The second method, developed by Kraljic and El Mohsni[33], involves a combination of imidazole group and RNO (referred as the Imd/RNO method).

Measurement of $^1O_2$ by SOSG probe. A 0.5 mM Ce6 stock solution was prepared by suspending Ce6 powder in MQ water and ultrasonicating for 20 min. The stock solution was then diluted to 10 μM with MQ water. Subsequently, 0.25 mL 10 μM Ce6 was mixed with an equal volume of 10 μM SOSG solution, resulting in a final concentration of 5 μM of Ce6 and SOSG. Both the mixtures and control samples (containing SOSG and water only) were then exposed to either X-rays or gamma-rays. After irradiation, the fluorescence of SOSG was measured at an excitation wavelength of 504 nm and an emission wavelength of 524 nm using a Cary Eclipse Fluorescence Spectrophotometer (Agilent Technologies).

The normalized relative increase in FL intensity was calculated as follows:

$$Relative\ increase\ FL\ intensity = \frac{FL\ (\ Ce6 + SOSG\ at\ each\ dose)}{FL\ (\ SOSG\ alone\ at\ each\ dose)} \quad \text{(Equation 2.1)}$$

$$Normalized\ relative\ FL\ intensity = \frac{Relative\ FL\ (\ Ce6 + SOSG\ at\ each\ dose)}{Relative\ FL\ (\ Ce6 + SOSG\ at\ 0\ Gy)} \quad \text{(Equation 2.2)}$$

First, the increased FL intensity of the Ce6 groups relative to the control groups was calculated by dividing the FL intensity of the Ce6 groups by the FL intensity of the control groups at the same specific dose. Then, the relative FL intensity obtained from the first step was normalized

by comparing it to the FL intensity at 0 Gy.

Confirmation of $^1O_2$ by Imd/RNO method. This method involves two main steps: initially, $^1O_2$ reacts rapidly with imidazole group, leading to its oxidation and the formation of a peroxide intermediate. In our experiment, we used L-histidine, which contains an imidazole group, as the reacting molecule. In the subsequent step, this peroxide intermediate reacts with RNO, causing the bleaching of RNO, which can be measured spectrophotometrically at 440 nm. For the assay, solutions of 0.2 mM Ce6, 25 mM L-histidine and 125 μM RNO were prepared separately in phosphate buffer (PB) (25 mM, pH = 7.4). These solutions (Ce6, L-histidine and RNO) were then mixed in a 96 well-plate to achieve a total volume of 200 μL, containing 40 μM Ce6, 10 mM L-histidine and 50 μM RNO (with or without 0.01% ethanol). The entire plate was then irradiated by X-rays at various dose rates in a dim environment. The absorption of RNO at 440 nm was measured by a microplate scanning spectrophotometer (PowerWave XS™, Bio-Tek) before and after the irradiation. For sunlight exposure experiments, the sample preparation was the same as that used in the X-ray irradiation experiments, except that stock solutions of Rose Bengal (0.1 mM in PB) and Ce6 (0.1 mM in PB) was further diluted to a final concentration of 10 μM.

Assessment of superoxide anions ($\cdot O_2^-$) contribution to $^1O_2$ formation using SOD. To investigate the potential role of superoxide anions in the system, the experiments described above were repeated with the addition of superoxide dismutase (SOD). The procedures for both SOSG and Imd/RNO measurements remained identical, except that SOD (1 μg/mL) was added to the samples before irradiation.

Confirmation of ·OH by APF probe. A 0.5 mM Ce6 stock solution was prepared by suspending Ce6 powder in MQ water and ultrasonicating for 20 min. The stock solution was then diluted to 10 μM with MQ water. Subsequently, 0.5 mL 10 μM Ce6 was mixed with an equal volume of 5 μM APF solution, resulting in a final concentration of 5 μM of Ce6 and 2.5 μM APF. Both the mixtures and control samples (containing APF and water only) were then exposed to X-rays. After irradiation, the fluorescence of APF was measured at an excitation wavelength of 490 nm and an emission wavelength of 515 nm using a Cary Eclipse Fluorescence Spectrophotometer (Agilent Technologies).

Statistical analysis

Data with error bar were presented as mean ± SD. Statistical analyses were performed using either one-way or two-way ANOVA as appropriate. GraphPad Prism software (version 8.00)

was used for statistical analysis and data visualization. $P < 0.05$ was considered statistically significant.

2.3 Results

Higher photon energy enhances singlet oxygen production at comparable dose rates

This section aims to investigate the role of radiation energy in activating Ce6, taking also into account possible Cerenkov light generation. To address this, two external radiation sources, X-rays and gamma-rays, were employed to deliver photons of different energies. The energy of the X-rays used was 310 kV, which will not produce Cerenkov light, while the energy of the gamma-rays delivered by a ^{60}Co source are well above the limit of Cerenkov light generation (i.e. 1.17 and 1.33 MeV). The activation of Ce6 was evaluated by measuring the formation of singlet oxygen ($^1O_2$) according to changes in fluorescence intensity (FL intensity) of the SOSG probe. Samples containing Milli Q water (MQ) with the same concentration of SOSG were used as a control group to account for any potential interaction of SOSG itself with ionizing radiation.

Figure 2.1 shows the FL intensity of SOSG in samples with or without Ce6 exposed to gamma or X-ray radiation. After exposure to gamma rays at a dose rate of 6.2 Gy/min (Fig. 2.1(a)), a significant increase in FL intensity was observed beyond 5 Gy in the Ce6 group compared to the control group, with a more pronounced enhancement at 10 and 20 Gy. To ensure comparable conditions with gamma-ray exposure, the dose rate of X-rays was set to 7 Gy/min (Fig. 2.1(b)), using a voltage of 310 kV and a current of 12 mA. A modest increase in FL intensity was noted at 20 Gy in the Ce6 group compared to controls.

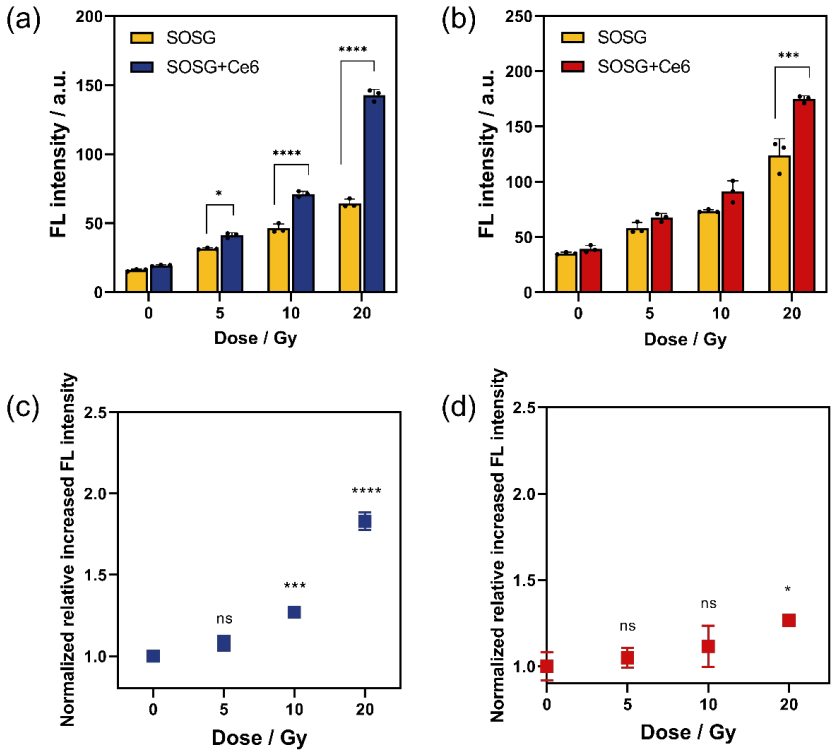

Figure 2.1. Higher-energy gamma-ray irradiation enhances SOSG fluorescence in the presence of Ce6 compared with X-ray irradiation. The direct fluorescence intensity values of SOSG in samples after exposure to: (a) a ^{60}Co source emitting gamma energy of 1.17 and 1.33 MeV at a dose rate of 6.2 Gy/min. (b) X-rays with a dose rate of 7 Gy/min (310 kV, 12 mA). (c) and (d) represent the normalized relative increase of fluorescence intensity of SOSG in Ce6-containing samples compared to the control groups, corresponding to (a) and (b) respectively, as calculated using Equation 2.1 and 2.2 (*see Methods*). All data are represented as mean ± SD and analyzed by two-way ANOVA (a and b) or one-way ANOVA (c and d); *$p < 0.05$, ***$p < 0.0005$, ****$p < 0.0001$; $n = 3$. [Ce6] = 5 μM; [SOSG] = 5 μM.

We noticed that the SOSG fluorescence also increased with radiation dose in the absence of Ce6 (Fig. S2.1). This radiation-induced response was further confirmed by the fluorescence spectra (Fig. S2.2(a)) and has been previously reported by Liu et al.[32], who showed that the fluorescence signal was influenced by ·OH produced during ionizing radiation. Consistently, the UV spectral analysis revealed decreased absorption at 257 nm (Fig. S2.2(b)), suggesting ·OH-mediated modification of SOSG's anthracene moiety,[34] which could disrupt its fluorescence quenching mechanism.

To properly assess the ability of Ce6 to generate $^1O_2$ compared to SOSG solutions alone, additional calculations were performed. First, the relative increase in the Ce6 group at each

dose compared to the control group was calculated using Equation 2.1 (see *Methods*). These values were then normalized to the relative FL intensity at 0 Gy according to Equation 2.2 (see *Methods*) to further isolate the effect of Ce6 from the baseline fluorescence differences at 0 Gy.

Figure 2.1(c) and Figure 2.1(d) present the data processed from Figure 2.1(a) and Figure 2.1(b) based on the described corrections. After normalization, an increase that was initially observed for a dose below 5 Gy under gamma-ray radiation (Fig. 2.1(a)) was no longer evident (Fig. 2.1(c)). The normalized relative FL intensities for 5 Gy, 10 Gy, and 20 Gy were 1.080 ± 0.046, 1.270 ± 0.036, and 1.829 ± 0.054, respectively. No significant increase was observed at 5 Gy in the Ce6 group, while significant differences in FL intensity were observed at 10 Gy ($p < 0.0005$) and 20 Gy ($p < 0.0001$) compared to non-irradiated samples. For the samples irradiated with X-rays at a dose rate of 7 Gy/min, the normalized FL intensity values were 1.049 ± 0.055, 1.116 ± 0.119, and 1.266 ± 0.023 for 5 Gy, 10 Gy, and 20 Gy, respectively. A significant enhancement was observed at 20 Gy ($p < 0.05$) (Fig. 2.1(d)).

The lowest dose rate (0.005 Gy/min) leads to the highest singlet oxygen production

The findings from the previous section demonstrate that Cerenkov light was not essential for activating Ce6, as $^1O_2$ was also detected when using X-rays with energy below the Cerenkov threshold. Building on these results, this section investigates the effect of dose rate on $^1O_2$ production, a factor that differs significantly between external and internal radiation.[35] Given the unpredictable dose rates inherent to radionuclide therapy, the lowest dose rate used here was 0.005 Gy/min, comparable to that used in low-dose-rate brachytherapy.[36] X-rays with an energy of 240 kV were used to avoid Cerenkov light formation, and the voltage-to-current ratio of the X-ray source was adjusted to achieve the desired dose rates, as detailed in Table 1.

Figure 2.2 shows the measurement of $^1O_2$ using the SOSG probe and the Imd/RNO method. In Figure 2.2(a), the FL intensity of the SOSG in samples following 5 Gy of X-ray irradiation at various dose rates are depicted. After normalization (Fig. 2.2(b)), the greatest enhancement in FL intensity in the presence of Ce6 was observed at 0.005 Gy/min, with a normalized relative increase of 2.505 ± 0.026 compared to non-irradiated samples. The corresponding values for dose rates of 7 Gy/min, 3 Gy/min, 0.2 Gy/min, and 0.05 Gy/min were 1.361 ± 0.108, 1.416 ± 0.131, 1.413 ± 0.115, and 1.580 ± 0.024, respectively. Statistical analysis showed that the normalized relative FL intensity at 0.005 Gy/min was significantly higher than those at higher dose rates ($p < 0.0001$). In contrast, the normalized relative FL intensities at dose rates of 7 Gy/min, 3 Gy/min, 0.2 Gy/min, and 0.05 Gy/min did not differ significantly from each other; however, a slight increase was observed compared to non-irradiated groups. The different

results at 5 Gy observed in our study between Figure 2.1(b) and Figure 2.2(b) at 7 Gy/min radiation may be due to variations in SOSG batches, as differences in solubility and sensitivity to $^1O_2$ could lead to the discrepancies in measured intensities.

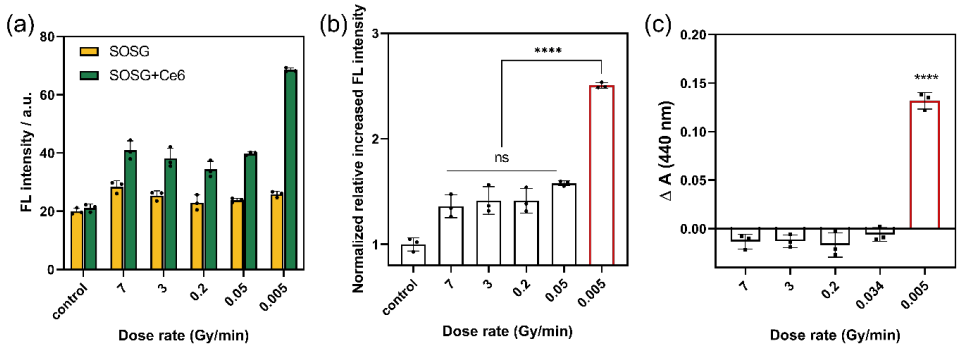

Figure 2.2. Low dose rate irradiation enhances SOSG fluorescence and RNO bleaching in the presence of Ce6. (a) Fluorescence intensity of SOSG in samples with or without Ce6. [Ce6] = 5 μM; [SOSG] = 5 μM. (b) Normalized relative increase in fluorescence intensity based on data derived from (A). (c) Absorption difference of RNO in the presence of Ce6 before and after X-ray irradiation. Samples contained 40 μM Ce6, 50 μM RNO and 10 mM L-histidine; ΔA denotes the difference between the absorption of RNO before and after irradiation; pH was set to 7.4 using phosphate buffer (PB). All data are represented as mean ± SD and analyzed by one-way ANOVA (b and c); ****$p < 0.0001$; $n = 3$.

To confirm the results obtained using SOSG, we used a second method for detecting $^1O_2$, known as the Imd/RNO method. This method showed effective detection of $^1O_2$ generation (Fig. S2.3(a)), which was completely inhibited by the $^1O_2$ quencher NaN_3 (Fig. S2.3(b)). In our experiments, the absorption of RNO was measured before and after the irradiation. The change in absorption ($\Delta A = A_{\text{before radiation}} - A_{\text{after radiation}}$) was used to evaluate the ability of Ce6 to generate $^1O_2$. When applying this method under ionizing radiation, it should be noted that RNO also quenches ·OH generated during water radiolysis,[37] which can lead to the decrease of RNO absorption and interfere with the detection of $^1O_2$. To minimize this effect, ethanol was added as a strong ·OH scavenger to protect RNO.[38] At a radiation dose of 70 Gy, a clear decrease in RNO absorption was observed in the RNO solution, but this effect was eliminated in the presence of 0.01% ethanol, confirming its protective role (Fig. S2.4(a)). In all subsequent X-ray irradiation experiments, 0.01% ethanol was present unless otherwise specified.

Figure 2.2(c) shows the absorption change of RNO in the presence of Ce6 before and after X-ray exposure. At a dose of 5 Gy delivered at a dose rate of 0.005 Gy/min, RNO absorption decreased significantly by 0.126 ± 0.013 ($p<0.0001$ compared to other groups). In contrast, no significant decrease in RNO absorption was observed when samples were irradiated at higher

dose rates (7, 3, 0.2 and 0.034 Gy/min). A similar decrease at 0.005 Gy/min was also observed with Ce6 in the absence of ethanol, whereas the control groups (Ce6+RNO, L-histidine+RNO, and RNO), with or without ethanol, showed only minor changes (Fig. S2.4(b)). For higher dose rates, the control groups (Ce6+RNO, L-histidine+RNO and RNO) exhibited negligible changes in RNO absorption (Fig. S2.4(c)).

Superoxide anions are involved in singlet oxygen formation

Research has suggested that free radicals from water radiolysis may play a role in the activation process of photosensitizers.[13,25] Our experimental results showed that when using the Imd/RNO method, the addition of ethanol had no effect on the formation of $^1O_2$ by Ce6 (Fig. S2.4(b)), indicating that ·OH were not involved in the formation process. To further explore the mechanism under ionizing radiation, we evaluated the role of free radicals, particularly superoxide anions ($\cdot O_2^-$), which has been shown to be influenced by dose rate due to possible radical-radical recombination.[39] This was achieved by introducing a $\cdot O_2^-$ scavenger, superoxide dismutase (SOD), during radiation exposure.

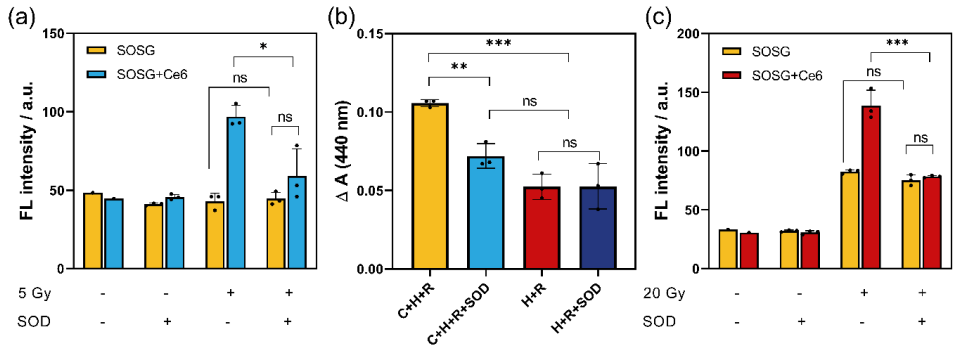

Figure 2.3. Addition of SOD eliminates the increase in SOSG fluorescence and RNO bleaching in the presence of Ce6. (a, b) Samples were exposed to 5 Gy of X-rays (240 kV, 1 mA; dose rate = 0.005 Gy/min). (a) Fluorescence change of SOSG. [Ce6] = 5 µM; [SOSG] = 5 µM; [SOD] = 1 µg/mL. (b) Change in RNO absorption. C+H+R samples contained 40 µM Ce6, 10 mM L-histidine and 50 µM RNO; C+H+R+SOD samples contained 40 µM Ce6, 10 mM L-histidine, 50 µM RNO and 1 µg/mL of SOD; H+R samples contained 10 mM L-histidine and 50 µM RNO; H+R+SOD samples contained 10 mM L-histidine, 50 µM RNO and 1 µg/mL of SOD; ΔA denotes the difference between the absorption of RNO before and after irradiation; pH was set to 7.4 using PB. (c) Fluorescence of SOSG after exposure to 20 Gy of gamma-ray radiation (1.17 and 1.33 MeV) at a dose rate of 6.2 Gy/min. [Ce6] = 5 µM; [SOSG] = 5 µM; [SOD] = 1 µg/mL. All data are represented as mean ± SD and analyzed by one-way ANOVA; *p < 0.05, **p < 0.01, ***p ≤ 0.0005; n = 3.

As shown in Figure 2.3(a), the addition of 1 µg/mL SOD did not affect the intrinsic fluorescence of SOSG without X-ray exposure, nor did it alter SOSG behavior after light exposure (Fig. S2.5(a)). In the absence of SOD, exposure to 5 Gy of X-rays at 0.005 Gy/min

resulted in an increase in FL intensity of SOSG in the Ce6 group compared to the control group, consistent with earlier findings. However, this increase was eliminated with the addition of SOD, as indicated by the lack of significant difference between the Ce6 group and the control group with SOD after irradiation. Similarly, the addition of SOD did not affect the decrease of RNO absorption in presence of Ce6 under sunlight exposure (Fig. S2.5(b)). In Figure 2.3(b), a significant decrease of RNO absorption was observed in the Ce6 group without SOD when compared to the control group without Ce6 after exposed to 5 Gy at a dose rate of 0.005 Gy/min. However, this decrease in RNO absorption in the presence of Ce6 was eliminated as well by the addition SOD, showing a significant difference when compared to the Ce6 group without SOD. Furthermore, in the presence of SOD, no significant difference was observed between the Ce6 group and the control group.

The effect of SOD on the FL intensity of SOSG in the presence of Ce6 was also studied under gamma-ray exposure. Figure 2.3(c) shows that after 20 Gy of gamma-ray radiation, the FL intensity of SOSG in the presence of Ce6 was significantly higher than that of the control group. However, after adding SOD, this increase disappeared and no difference of the FL intensity of SOSG was observed between the Ce6 group and control group. Notably, SOSG itself still had higher FL intensity after 20 Gy irradiation compared to 0 Gy regardless of the addition of SOD.

The UV absorption of SOSG molecules both before and after irradiation in the presence of SOD was measured to check whether SOD would structurally influence the SOSG molecule (Fig. S2.5(c)). The UV spectrum shows that the addition of SOD did not affect the molecular structure of SOSG, even after radiation, as no noticeable decrease in SOSG absorption was observed.

2.4 Discussion

In this study, we systematically investigated the $^1O_2$ generation by Ce6 under ionizing radiation, focusing on key factors such as radiation energy (below or above the threshold of generating Cerenkov light in water), dose rate, and the effects of free radicals. We primarily evaluated $^1O_2$ formation using the SOSG probe during irradiation by measuring the increase in FL intensity at an emission wavelength of 528 nm. Additionally, we used the Imd/RNO method as a complementary approach to validate the obtained results.

X-rays with energy up to 310 kV and gamma rays with energy of 1.17 and 1.33 MeV can both activate Ce6 to produce $^1O_2$, with increasing doses leading to more $^1O_2$ production (Fig. 2.1). Gamma rays appeared to be more efficient than X-rays in activating Ce6 when compared at similar dose rates, achieving higher $^1O_2$ production at a lower dose. This enhanced response was specific to Ce6, as the SOSG controls showed comparable behavior under both X-ray and gamma ray irradiation (Fig. S2.1(a)). While gamma rays generated more $^1O_2$, several observations suggest that this enhanced production is not driven by Cerenkov radiation. First, at the energy levels used in this study, gamma rays produce minimal Cerenkov radiation.[40] Second, X-ray irradiation successfully generated $^1O_2$ (Fig. 2.1(b) and Fig. S2.6), despite the absence of Cerenkov light (Fig. S2.7). These observations suggest that the difference in $^1O_2$ production between gamma rays and X-rays is likely driven by their energy and related interaction mechanism.

The relationship between dose rate and $^1O_2$ production exhibits a distinct pattern, where dose rates ranging from 0.05 Gy/min to 7 Gy/min showed minimal impact, a significant increase was observed at the much lower dose rate, i.e. 0.005 Gy/min (Fig. 2.2(a) and Fig. 2.2(b)). To address the potential interference from SOSG, this observation was further validated using the Imd/RNO method, which further confirmed that the lowest dose rate (0.005 Gy/min) led to a substantial increase in $^1O_2$ production (Fig. 2.2(c)). Furthermore, the decrease in RNO absorption was consistent for samples with and without ethanol, confirming that the reduction in RNO can be attributed to the formation of $^1O_2$ and not of ·OH (Fig. S2.4(b)). To the best of our knowledge, this study is the first to demonstrate that radiation dose rate affects the production of $^1O_2$ by photosensitizers, as demonstrated here by Ce6.

There are no reports investigating similar effects in other types of photosensitizers. In principle, photosensitizes such as Ce6 is activated by absorbing an incident photon with energy of approximately 1.14 eV to ultimately form a triplet state,[41] which can subsequently transfer

energy to $^3O_2$ and form $^1O_2$. However, it is very unlikely for ionizing radiation to follow this activation pathway, as energy of ionizing radiation far exceeds 1.14 eV. Instead, this activation may occur in subsequent steps, where the energy deposited by ionizing radiation into the surrounding medium (e.g., water) triggers subsequent indirect processes that ultimately lead to the production of $^1O_2$ by Ce6.

The energy deposition of ionizing radiation in water is categorized into 3 main stages: the physical stage (~10^{-15} s), the physicochemical stage (10^{-15} to ~ 10^{-12} s) and the chemical stage (10^{-12} to ~ 10^{-6} s). During the initial physical stage, the primary ionizations produce secondary electrons through excitation and ionization of surrounding molecules. These secondary electrons undergo cascading energy loss, eventually generating low energy electrons that can no longer induce molecular excitation or ionization.[42] One could expect that these low energy electrons having energy above 1.14 eV could transfer energy to Ce6 molecules, resulting in the triplet state of Ce6 and in turn producing $^1O_2$, which might explain the dose-dependent manner of the increased FL intensity of SOSG with Ce6 (Fig. 2.1), as the production of secondary electrons is dose-dependent.

The energy deposition of low energy electrons predominantly depends on the initial radiation energy.[42,43] If these electrons were solely responsible for Ce6 activation, $^1O_2$ production should remain consistent at a given dose regardless of the dose rate. However, our observations at 5 Gy across different dose rates showed dose rate-related variations in $^1O_2$ production, despite nearly identical X-ray energy spectra (Fig. S2.7), suggesting the involvement of processes beyond the physical stage. While the excited H_2O^* molecules (with energy ~ 1.3 eV above the first ionization potential[43]) could potentially transfer energy to Ce6, their short lifetime (~ 0.8 ps[44]) and low yield[43] make their contribution negligible.

Dissolved molecular oxygen plays a crucial role as a precursor to $^1O_2$. During exposure to ionizing radiation, a continuous consumption of O_2 occurs through the following reactions.[45]

$$e^-_{aq} + O_2 \rightleftarrows \cdot O_2^-$$

$$H^\cdot + O_2 \rightleftarrows HO_2^\cdot$$

At lower dose rates, two factors could potentially enhance the energy transfer process between Ce6 and oxygen: the slower O_2 consumption rate compared to high dose rates, which allows Ce6 molecules to be surrounded by more O_2, and the longer irradiation time, which enables more efficient O_2 replenishment. This could theoretically provide more opportunities for Ce6 to transfer energy to surrounding oxygen. However, given that the dissolved O_2 concentration

in water under normal atmospheric pressure (~250 μM) is sufficiently high, a 5 Gy dose would not significantly deplete it.[46] Therefore, O_2 availability is unlikely to be a limiting factor in Ce6 activation. Rather, free radicals and molecular products generated during irradiation appear to be more probable drivers of Ce6 activation and subsequent $^1O_2$ production.

Recent studies have shown that the yield of free radicals, such as ·OH and e_{aq}^-, varied with dose rate, possibly due to the complicated intra-track radical-radical recombination.[39,47] The Imd/RNO results (Fig. 2.2(c)) clearly indicated that ·OH was not involved in the generation of $^1O_2$ by Ce6, as the measurement done in the presence of ethanol, a known quencher of ·OH, a substantial amount of $^1O_2$ was still formed at a dose rate of 0.005 Gy/min.

The yield of e_{aq}^- decreases with increasing dose rate, likely because e_{aq}^- are involved in numerous radiolysis processes, and at higher dose rates, the denser distribution of radiolysis products increases the chance of radical-radical recombination.[47] Of particular interest is their interaction with O_2 molecules, which leads to the formation of $\cdot O_2^-$, a species that was found to generate $^1O_2$ through a redox reaction.[48] Interestingly, our experiments using SOD to quench $\cdot O_2^-$ eliminated the increased production of $^1O_2$ at low dose rate in both the SOSG and the Imd/RNO method (Fig. 2.3(a) and Fig. 2.3(b)). Additionally, the elimination of $^1O_2$ observed at 20 Gy gamma-ray radiation (Fig. 2.3(c)), further supports the important role of $\cdot O_2^-$ in the $^1O_2$ production by Ce6. While the exact mechanism remains unclear, thermodynamic considerations of the redox potential of $\cdot O_2^-$ and the triplet state of Ce6 (^{3}Ce6*) suggest that direct formation of $^1O_2$ via oxidation of $\cdot O_2^-$ by ^{3}Ce6* is unlikely.[48,49]

We can now propose a possible mechanistic pathway for the generation of $^1O_2$ by Ce6 under ionizing radiation conditions, which differs significantly from traditional photosensitization processes. While conventional photosensitization of Ce6 typically proceeds through excitation to its triplet state, our results suggest that high-energy radiation leads to the formation of Ce6 radical cations ($Ce6^{\bullet+}$). These radical cations can subsequently react with $\cdot O_2^-$ to produce $^1O_2$. The possibility of such a pathway is supported by previous studies reporting the existence of radical cations of photosensitizers when exposed to ionizing radiation.[50,51] In addition, this mechanism is similar to the one proposed by Kavarnos and Turro[52] when describing porphyrin photochemistry. These papers suggest that $^1O_2$ formation can occur either through energy transfer process (Equation 2.3) or stepwise electron exchange in polar solvents (Equation 2.4 and 2.5). However, in our radiation-induced system, the conventional photosensitization pathways (Equation 2.3 and 2.4) are unfavorable due to the huge energy gap between ionizing radiation and visible light.

$$^3PS^* + {}^3O_2 \rightarrow PS + {}^1O_2 \quad \text{(Equation 2.3)}$$

$$^3PS^* + {}^3O_2 \rightarrow PS^{\bullet+} + \cdot O_2^- \quad \text{(Equation 2.4)}$$

$$PS^{\bullet+} + \cdot O_2^- \rightarrow PS + {}^1O_2 \quad \text{(Equation 2.5)}$$

Instead, we propose that the electron exchange reaction between $Ce6^{\bullet+}$ and $\cdot O_2^-$ (Equation 2.5) dominates the $^1O_2$ generation process, as indicated in Scheme 2.1. According to the literature, porphyrin compounds typically undergo oxidation at potentials around +0.9 to +1.0 V vs NHE in aqueous media.[53] Given the structural similarities between Ce6 and these porphyrin compounds, the redox potential of $Ce6^{\bullet+}$ can be estimated to be in a similar range. At this potential, the oxidation of $\cdot O_2^-$ to $^1O_2$ (redox potential at least +0.34 V vs NHE[48]) would be thermodynamically favorable, supporting this proposed mechanism. Furthermore, the radiolysis of water provides a direct source of $\cdot O_2^-$ that can react with $Ce6^{\bullet+}$, thereby contributing to the generation of $^1O_2$.[54-57]

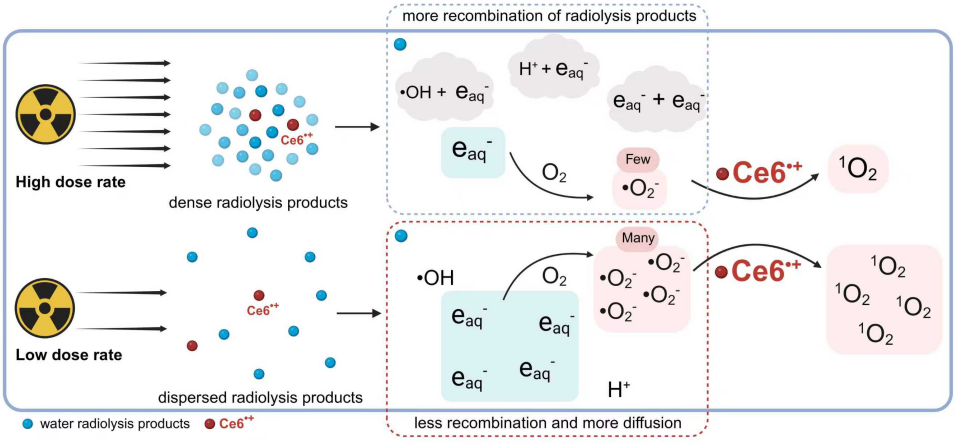

Scheme 2.1. Schematic illustration of the proposed mechanism for $^1O_2$ generation by Ce6 under high- and low-dose-rate ionizing radiation exposure.

The enhanced $^1O_2$ generation observed specifically at a very low dose rate suggests a kinetically driven process. At very low dose rates, the extended time between ionization events give e_{aq}^- more opportunity to react with O_2, favoring the formation of $\cdot O_2^-$ over recombination with other radicals. This increased availability of $\cdot O_2^-$ enhances the interaction with $Ce6^{\bullet+}$. At higher dose rates, higher dose was required to achieve the same level of $^1O_2$ production, likely because the increased density of radical formation promoted rapid radical-radical

recombination, reducing the efficiency of $\cdot O_2^-$ formation and its subsequent reaction with $Ce6^{\bullet+}$. The enhanced $^1O_2$ production observed under gamma-ray irradiation compared to X-rays at similar doses may arise from differences in photon energy and their associated linear energy transfer (LET) characteristics. Gamma-rays, with higher initial energy and lower LET, produce more spatially dispersed radicals during water radiolysis, potentially reducing inter-track radical interactions.[58] However, our comparison between only two photon energies cannot conclusively identify LET as the primary driver of enhanced $^1O_2$ generation. Future studies using particle beams with controlled energies could better identify the roles of energy and LET in photosensitizer activation.

From a practical perspective, when considering PSs as radiosensitizers, their biological effects under ionizing radiation arise from a complex interplay of reactive species, not only $^1O_2$ but also ·OH and even PS-derived radicals. Although our experiments confirmed that ·OH is not involved in $^1O_2$ generation by Ce6, we further examined ·OH formation under ionizing radiation in presence of Ce6 using the APF probe. As shown in Figure S8, Ce6 enhanced $^1O_2$ production, whereas no increase in ·OH was detected using the APF probe. The APF fluorescence signal with Ce6 were even slightly reduced compared using APF alone, which may be explained by the ability of Ce6 to scavenge ·OH as mentioned in some studies.[59] These results demonstrate the important role of $^1O_2$ when applying Ce6 as a radiosensitizer. Compared with ·OH or $\cdot O_2^-$, $^1O_2$ remains the most biologically impactful species, as it oxidizes unsaturated lipids, proteins and nucleic acids and has a relatively long diffusion range.[56,60,61] In addition, studies have found that PS-derived radical cations ($PS^{\bullet+}$) can directly oxidize DNA bases, especially attacking guanine residues and inducing strand lesions,[62] but these effects are local and further restricted by the subcellular distribution of most PSs to mitochondria, lysosomes, and the endoplasmic reticulum rather than the nucleus.[63,64] These findings indicate that while the overall biological effects of PS-mediated radiosensitization arise from the combined actions of multiple ROS and PS radicals, $^1O_2$ still remains the dominant and most biologically significant species. This work focuses on elucidating the generation of $^1O_2$ and its interplay with $\cdot O_2^-$, offering mechanistic insights that may guide future investigations of PS-driven ROS networks. While low dose rate modalities such as brachytherapy or radionuclide therapy might enhance $^1O_2$ production, careful consideration and further investigation are required due to the complexity of intracellular antioxidant defenses, the availability of $\cdot O_2^-$ and dose-rate-dependent alterations in cellular responses.

A primary limitation of this study lies in the reliance on indirect methods for detection of $^1O_2$.

While we employed both SOSG fluorescence and the Imd/RNO bleaching assay, these approaches are inherently less sensitive than direct detection methods and may fail to capture short-lived species. This limitation may partly explain why no detectable $^1O_2$ signal was observed at 5 Gy under higher dose rates irradiation in our experiments, even though photosensitizers at this dose and within this dose rate range are known to induce cytotoxic effects.[65] Second, although our scavenging experiments strongly suggest the involvement of $\cdot O_2^-$ in $^1O_2$ formation, direct observation of the reaction between $Ce6^{\bullet+}$ and $\cdot O_2^-$ was not achieved due to the technical challenges in detecting these short-lived species during irradiation. Finally, the preferential formation of $^1O_2$ through the $\cdot O_2^-$ pathway rather than traditional triplet state mechanisms requires further investigation. Specifically, computational simulations and experimental studies should quantify how efficiently superoxide is formed under different dose rates and radiation qualities.

2.5 Conclusion

In this study, we systematically investigated the interaction of Ce6 with ionizing radiation, first examining the effects of different photon energies and then exploring the impact of dose rates. Notably, enhanced $^1O_2$ generation was observed at very low dose rates (0.005 Gy/min). Through scavenging experiments, we identified $\cdot O_2^-$ as a possible key intermediate in $^1O_2$ formation. Our mechanistic investigation suggests that, unlike traditional photosensitization where triplet states dominate, Ce6 activation by ionizing radiation proceeds primarily through free radical reactions, with $Ce6^{\bullet+}$ interacting with radiation-induced $\cdot O_2^-$ to generate $^1O_2$. The enhanced efficiency at low dose rates and high energy radiation indicates that radical lifetime and spatial distribution play crucial roles in this process. The involvement of $\cdot O_2^-$ in this mechanism suggests that the therapeutic efficacy of combined photosensitizer-radiation treatment may be influenced by the oxidative stress status of cancer cells, especially those with elevated ROS levels and reduced SOD activity. Our data also suggest that low-dose-rate treatments like brachytherapy and radionuclide therapy may be more effective when combined with PSs, as they maintain continuous ROS generation in cancer cells and enhance the production of $^1O_2$ by Ce6. However, extensive biological studies would need to be performed to confirm whether in cellular environment the same effects would occur.

References

1 M. B. Barton, S. Jacob, J. Shafiq, K. Wong *et al.* Estimating the demand for radiotherapy from the evidence: a review of changes from 2003 to 2012. *Radiotherapy and oncology : journal of the European Society for Therapeutic Radiology and Oncology* **112**, 140-144 (2014).

2 Dash, A., Knapp, F. F. R., Pillai, M. R. A., Dash, A. *et al.* Targeted Radionuclide Therapy - An Overview. *Current Radiopharmaceuticals* **6**, 152-180 (2013).

3 Baskar, R., Lee, K. A., Yeo, R. & Yeoh, K. W. Cancer and Radiation Therapy: Current Advances and Future Directions. *International Journal of Medical Sciences* **9**, 193-199 (2012).

4 Chargari, C., Deutsch, E., Blanchard, P., Gouy, S. *et al.* Brachytherapy: An overview for clinicians. *CA: A Cancer Journal for Clinicians* **69**, 386-401 (2019).

5 Berg, K., Luksiene, Z., Moan, J. & L, M. Combined treatment of ionizing radiation and photosensitization by 5-aminolevulinic acid-induced protoporphyrin IX. *Radiation Research* **142**, 340-346 (1995).

6 Adeberg, S., König, L., Bostel, T., Harrabi, S. *et al.* Glioblastoma Recurrence Patterns After Radiation Therapy With Regard to the Subventricular Zone. *International Journal of Radiation Oncology, Biology, Physics* **90**, 886-893 (2014).

7 Bartelink, H., Horiot, J. C., Poortmans, P., Struikmans, H., Van den Bogaert, W., Barillot, I., Fourquet, A., Borger, J., Jager, J., Hoogenraad, W., et al. Recurrence rates after treatment of breast cancer with standard radiotherapy with or without additional radiation. *The New England journal of medicine* **345**, 1378-1387 (2001).

8 Wardman, P. Chemical Radiosensitizers for Use in Radiotherapy. *Clinical Oncology* **19**, 397-417 (2007).

9 Stupp, R., Mason, W. P., Van Den Bent, M. J., Weller, M. *et al.* Radiotherapy plus Concomitant and Adjuvant Temozolomide for Glioblastoma. *The New England journal of medicine* **352**, 987-996 (2005).

10 Pepper, N. B., Stummer, W. & Eich, H. T. The use of radiosensitizing agents in the therapy of glioblastoma multiforme—a comprehensive review. *Strahlentherapie und Onkologie* **198**, 507-526 (2022).

11 Allison, R. R., Downie, G. H., Cuenca, R., Hu, X. H. *et al.* Photosensitizers in clinical PDT. *Photodiagnosis and Photodynamic Therapy* **1**, 27-42 (2004).

12 Schwartz, S., Absolon, K. & Vermund, H. Hospital Report Porphyrins, X-Rays and Tumors. *Univ. Minnesota Med. Bull.* **27**, 1-37 (1955).

13 Schaffer, M., Schaffer, P. M., Corti, L., Gardiman, M. *et al.* Photofrin as a specific radiosensitizing agent for tumors: studies in comparison to other porphyrins, in an experimental in vivo model. *Journal of Photochemistry and Photobiology B: Biology* **66**, 157-164 (2002).

14 Schaffer, M., Schaffer, P. M., Vogesser, M., Ertl-Wagner, B. *et al.* Application of Photofrin II as a specific radiosensitising agent in patients with bladder cancer—a report of two cases. *Photochemical & Photobiological Sciences* **1**, 686-689 (2002).

15 Schaffer, M., Ertl-Wagner, B., Schaffer, P. M., Kulka, U. *et al.* Feasibility of Photofrin II as a Radiosensitizing Agent in Solid Tumors – Preliminary Results. *Oncologie* **29**, 514-519 (2006).

16 Schaffer, P., Batash, R., Ertl-Wagner, B., Hofstetter, A. *et al.* Treatment of cervix carcinoma FIGO IIIb with Photofrin II as a radiosensitizer: a case report. *Photochemical & Photobiological Sciences* **18**, 1275-1279 (2019).

17 Pignatelli, P., Umme, S., D'Antonio, D. L., Piattelli, A. & Curia, M. C. Reactive Oxygen Species Produced by 5-Aminolevulinic Acid Photodynamic Therapy in the Treatment of Cancer. *International Journal of Molecular Sciences* **24**, 8964 (2023).

18 Cozzens, J. W., Lokaitis, B. C., Delfino, K., Hoeft, A. *et al.* A Phase 2 Sensitivity and Selectivity Study of High-Dose 5-Aminolevulinic Acid in Adult Patients Undergoing Resection of a Newly Diagnosed or Recurrent Glioblastoma. *Operative Neurosurgery* **29**, 71-79 (2024).

19 Yang, D. M., Cvetkovic, D., Chen, L. & Ma, C. C. Therapeutic effects of in-vivo radiodynamic therapy (RDT) for lung cancer treatment: a combination of 15MV photons and 5-aminolevulinic acid (5-ALA). *Biomedical Physics and Engineering Express* **8**, 6 (2022).

20 Takahashi, J., Misawa, M., Murakami, M., Mori, T. *et al.* 5-Aminolevulinic acid enhances cancer radiotherapy in a mouse tumor model. *SpringerPlus* **2**, 602 (2013).

21 Panetta, J. V., Cvetkovic, D., Chen, X., Chen, L., & Ma, C. C. . Radiodynamic therapy using 15-MV radiation combined with 5-aminolevulinic acid and carbamide peroxide for prostate cancer in vivo. *Physics in Medicine and Biology* **65**, 165008 (2020).

22 Takahashi, J., Nagasawa, S., Doi, M., Takahashi, M. *et al.* In Vivo Study of the Efficacy and Safety of 5-Aminolevulinic Radiodynamic Therapy for Glioblastoma Fractionated Radiotherapy. *International Journal of Molecular Sciences* **22**, 9762 (2021).

23 Pepper, N. B., Eich, H. T., Müther, M., Oertel, M. *et al.* ALA-RDT in GBM: protocol of the phase I/II dose escalation trial of radiodynamic therapy with 5-Aminolevulinic acid in patients with recurrent glioblastoma. *Radiation Oncology* **19**, 11 (2024).

24 Larue, L., Ben Mihoub, A., Youssef, Z., Colombeau, L. *et al.* Using X-rays in photodynamic therapy: an overview. *Photochemical & Photobiological Sciences* **17**, 1612-1650 (2018).

25 Takahashi, J. & Misawa, M. Characterization of reactive oxygen species generated by protoporphyrin IX under X-ray irradiation. *Radiation Physics and Chemistry* **78**, 889-898 (2009).

26 Kitagawa, T., Yamamoto, J., Tanaka, T., Nakano, Y. *et al.* 5-Aminolevulinic acid strongly enhances delayed intracellular production of reactive oxygen species (ROS) generated by ionizing irradiation: Quantitative analyses and visualization of intracellular ROS production in glioma cells in vitro. *Oncology Reports* **33**, 583-590 (2015).

27 Ueta, K., Yamamoto, J., Tanaka, T., Nakano, Y. *et al.* 5-Aminolevulinic acid enhances mitochondrial stress upon ionizing irradiation exposure and increases delayed production of reactive oxygen species and cell death in glioma cells. *International Journal of Molecular Medicine* **39**, 387-398 (2017).

28 Axelsson, J., Davis, S. C., Gladstone, D. J. & Pogue, B. W. Cerenkov emission induced by external beam radiation stimulates molecular fluorescence. *Medical Physics* **38**, 4127-4132 (2011).

29 Yang, D. M., Cvetkovic, D., Jr, A. E., Chen, L. & Ma, C. M. C. Tumor Regression with 5-Aminolevulinic Acid (5-ALA)-Mediated Radiodynamic Therapy (RDT) Using Different Megavoltage Energies. *International Journal of Radiation Oncology, Biology, Physics* **117**, e270 (2023).

30 Spinelli, A. E. & Boschi, F. Photodynamic Therapy Using Cerenkov and Radioluminescence Light. *Frontiers in Physics* **9**, 637120 (2021).

31 Miyamoto, S., Martinez, G. R., MedeirosPaolo, M. H. G. & Mascio, D. Singlet molecular oxygen generated from lipid hydroperoxides by the russell mechanism: studies using ^{18}O-labeled linoleic acid hydroperoxide and monomol light emission measurements. *Journal of the American Chemical Society* **125**, 6172-6179 (2003).

32 Liu, H., Carter, P. J. H., Laan, A. C., Eelkema, R. & Denkova, A. G. Singlet Oxygen Sensor Green is not a Suitable Probe for $^1O_2$ in the Presence of Ionizing Radiation. *Scientific Report* **9**, 8393 (2019).

33 Kraljić, I. & Mohsni, S. E. A New Method for the detection of singlet oxygen in aqueous solutions. *Photochemistry and Photobiology* **28**, 577-581 (1978).

34 Kim, S., Fujitsuka, M. & Majima, T. Photochemistry of Singlet Oxygen Sensor Green. *The Journal of Physical Chemistry B* **117**, 13985-13992 (2013).

35 Beddok, A., Lahaye, C., Calugaru, V., De Marzi, L., Fouillade, C., Salvador, S., Fontbonne, J. M., Favaudon, V., & Thariat, J. . A Comprehensive Analysis of the Relationship Between Dose Rate and Biological Effects in Preclinical and Clinical Studies, From Brachytherapy to Flattening Filter Free Radiation Therapy and FLASH Irradiation. *International Journal of Radiation Oncology, Biology, Physics* **113**, 985-995 (2022).

36 Viswanathan, A. N., Erickson, B. A., Ibbott, G. S., Small, W., Jr, & Eifel, P. J. The American College of Radiology and the American Brachytherapy Society practice parameter for the performance of low-dose-rate brachytherapy. *Brachytherapy* **16**, 68-74 (2017).

37 Sharpatyi, V. A. & Kraljić, I. Determination of singlet oxygen in radiolysis of aerated aqueous solution. *Photochemistry and Photobiology* **28**, 587-590 (1978).

38 Kraljić, I. & Trumbore, C. p-Nitrosodimethylaniline as an OH radical scavenger in radiation chemistry. *Journal of the American Chemical Society* **87**, 2547-2550 (1965).

39 Jansen, J., Knoll, J., Beyreuther, E., Pawelke, J. *et al.* Does FLASH deplete oxygen? Experimental evaluation for photons, protons, and carbon ions. *Medical Physics* **48**, 3982-3990 (2021).

40 Zhang, Q., Xiao, G., Sun, Q., Zeng, J. *et al.* Investigation of the Mechanisms of Radio-Dynamic Therapy. *Mathews Journal of Cancer Science* **5**, 19 (2020).

41 Gattuso, H., Monari, A. & Marazzi, M. Photophysics of chlorin e6: from one- and two-photon absorption to fluorescence and phosphorescence. *RSC Advances* **7**, 10992-10999 (2017).

42 Pimblott, S. M. & LaVerne, J. A. Production of low-energy electrons by ionizing radiation. *Radiation Physics and Chemistry* **76**, 1244-1247 (2007).

43 Cobut, V., Frongillo, Y., Patau, J., Goulet, T. *et al.* Monte Carlo simulation of fast electron and proton tracks in liquid water-I. Physical and physicochemical aspects. *Radiation Physics and Chemistry* **51**, 229-244 (1998).

44 Wang, Z., Pang, Y., & Dlott, D. D. Hydrogen-Bond Disruption by Vibrational Excitations in Water. *The Journal of Physical Chemistry A* **111**, 3196-3208 (2007).

45 Boscolo, D., Scifoni, E., Durante, M., Krämer, M. & Fuss, M. C. May oxygen depletion explain the FLASH effect? A chemical track structure analysis. *Radiotherapy and Oncology* **162**, 68-75 (2021).

46 Karle, C., Liew, H., Tessonnier, T., Mein, S. *et al.* Oxygen consumption measurements at ultra‐high dose rate over a wide LET range. *Medical Physics* **52**, 1323-1334 (2024).

47 Kusumoto, T., Danvin, A., Mamiya, T., Arnone, A. *et al.* Dose Rate Effects on Hydrated Electrons, Hydrogen Peroxide, and a OH Radical Molecular Probe Under Clinical Energy Protons. *Radiation Research* **201**, 287-293.

48 Sawyer, D. T. & Valentine, J. S. How super is superoxide? *Accounts of Chemical Research* **14**, 393-400 (1981).

49 Baptista, M. S., Cadet, J., Greer, A. & Thomas, A. H. Photosensitization Reactions of Biomolecules: Definition, Targets and Mechanisms. *Photochemistry and Photobiology* **97**, 1456-1483 (2021).

50 Imamura, T., Takahashi, M., Tanaka, T., Jin, T. *et al.* Optical and ESR studies for the reaction of molybdenum tetraphenylporphyrns in gamma-ray irradiated 2-methyltetrahydrofuran. *Inorganic Chemistry* **23**, 3752-3755 (1984).

51 Konishi, S., Hoshino, M. & Imamura, M. Triplet ESR spectrum of the copper porphyrin cation radical. *Journal of the American Chemical Society* **104**, 2057-2059 (1982).

52 Kavarnos, G. J. & Turro, N. J. Photosensitization by reversible electron transfer: theories, experimental evidence, and examples. *Chemical Reviews* **86**, 401-449 (1986).

53 Manaia, M. N., & Chiorcea-Paquim, A. M. Solid state electrochemical behaviour of porphine in aqueous media. *Journal of Electroanalytical Chemistry* **929**, 117123 (2023).

54 Schaap, A. P., Zaklika, K. A., Kaskar, B. & Fung, L. W. M. Mechanisms of photooxygenation. 2. Formation of 1,2-dioxetanes via 9,10-dicyanoanthracene-sensitized electron-transfer processes. *Journal of the American Chemical Society* **102**, 389-391 (1980).

55 E. F. F. Silva, C. Serpa, J. M. Dabrowski, C. J. P. Monteiro *et al.* Mechanisms of Singlet-Oxygen and Superoxide-Ion Generation by Porphyrins and Bacteriochlorins and their Implications in Photodynamic Therapy. *Chemistry (Weinheim an Der Bergstrasse, Germany)* **16**, 9273-9286 (2010).

56 Przygoda, M., Bartusik-Aebisher, D., Dynarowicz, K., Cieślar, G. *et al.* Cellular Mechanisms of Singlet Oxygen in Photodynamic Therapy. *International Journal of Molecular Sciences* **24**, 16890 (2023).

57 Pandey, N. K., Xiong, W., Wang, L., Chen, W. *et al.* Aggregation-induced emission luminogens for highly effective microwave dynamic therapy. *Bioactive Materials* **7** (2021).

58 Pimblott, S. M. & LaVerne, J. A. Diffusion-Kinetic Theories for LET Effects on the Radiolysis of Water. *The Journal of Physical Chemistry* **98**, 6136-6143 (1994).

59 Yu, J. W., Yoon, S. S., & Yang, R. Iron Chlorin e6 Scavenges Hydroxyl Radical and Protects Human Endothelial Cells against Hydrogen Peroxide Toxicity. *Biological and Pharmaceutical Bulletin* **24**, 1053-1059 (2001).

60 Valenzeno, D. P. Photomodification of biological membranes with emphasis on singlet oxygen mechanisms. *Photochemistry and Photobiology* **46**, 147-160 (1987).

61 Esben Skovsen, John W. Snyder, John D. C. Lambert, a. & Ogilby, P. R. Lifetime and Diffusion of Singlet Oxygen in a Cell. *The Journal of Physical Chemistry B* **109**, 8570-8573 (2005).

62 Enescu, M., Steenkeste, K., Enescu, M., Tfibel, F. *et al.* Ultrafast Guanine Oxidation by Photoexcited Cationic Porphyrins Intercalated into DNA. *The Journal of Physical Chemistry B* (2004).

63 Moan, J., Berg, K., Kvam, E., Western, A., Malik, Z., Rück, A., & Schneckenburger, H. . Intracellular localization of photosensitizers. *Ciba Foundation Symposium* **146**, 95-111 (1989).

64 Oliveira, C. S., Turchiello, R., Kowaltowski, A. J., Indig, G. L. & Baptista, M. S. Major determinants of photoinduced cell death: Subcellular localization versus photosensitization efficiency. *Free Radical Biology and Medicine* **51**, 824-833 (2011).

65 Hosoi, Y., Kawamura, M., Ido, T., Takai, Y. *et al.* Sensitization of cells to ionizing radiation by chlorine6Na. *Radiation Oncology Investigations* **6**, 151-156 (1998).

Supporting information

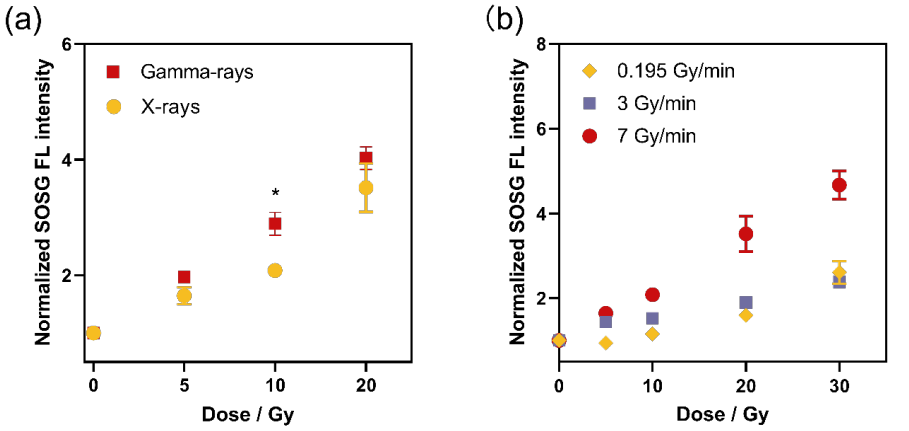

Figure S2.1. SOSG fluorescence increases with radiation dose and dose rate in the absence of Ce6. Data was obtained by normalizing SOSG FL intensity at each dose to the non-irradiated SOSG controls (0 Gy). (a) Comparison between 7 Gy/min X-ray radiation and 6.2 Gy/min gamma-ray radiation. [SOSG] = 5 µM. (b) Comparison between different X-ray dose rates. Values of FL intensity at all doses were normalized to the FL intensity at 0 Gy. [SOSG] = 5 µM. All data are represented as mean ± SD and analyzed by two-way ANOVA (a): *p = 0.0134; n = 3.

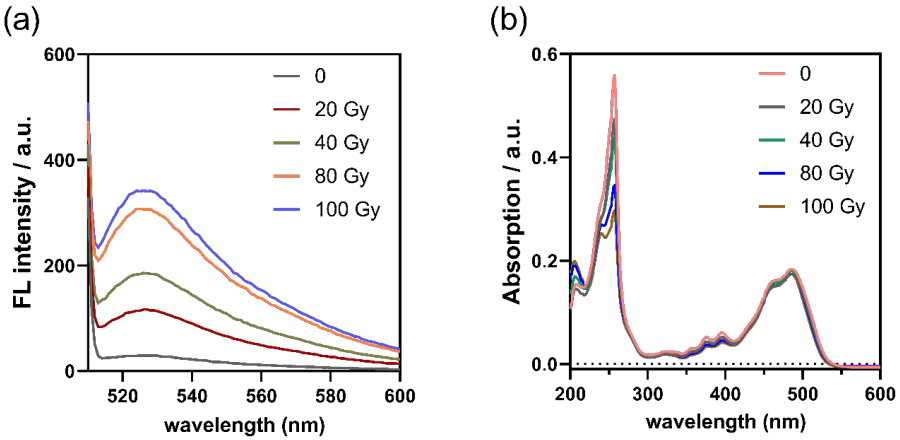

Figure S2.2. Gamma-ray irradiation increases SOSG fluorescence and reduced its absorption at 257 nm. (a) Fluorescence intensity of SOSG as a function of dose. (b) UV absorption of SOSG molecules after being exposed to various doses. [SOSG] = 5 µM.

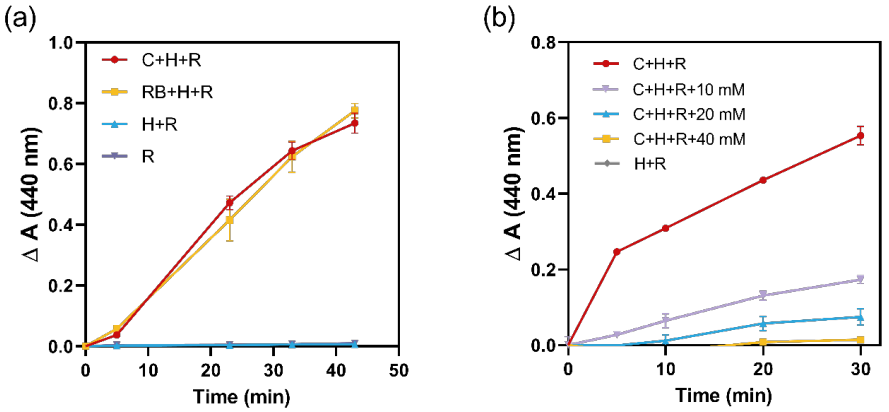

Figure S2.3. Sunlight-induced RNO bleaching by Ce6 is inhibited by NaN_3. (a) The bleaching of RNO by photosensitizer Ce6 (red line) and Rose Bengal (RB) as positive control (yellow line) under sunlight exposure for 5, 23, 33 and 43 min. (b) Reversal of RNO bleaching by Ce6 upon addition of NaN_3 at different concentrations under sunlight exposure for 5, 10, 20 and 30 min. Sample compositions: C+H+R: 10 µM Ce6 + 50 µM RNO + 10 mM L-histidine; RB+H+R: 10 µM Rose Bengal + 10 mM L-histidine + 50 µM RNO; H+R: 10 mM L-histidine + 50 µM RNO; R: 50 µM RNO; C+H+R+40 mM/20 mM/10 mM: 10 µM Ce6 + 10 mM L-histidine + 50 µM RNO + 10/20/40 mM NaN_3; pH was set to 7.4 using PB buffer. n = 3.

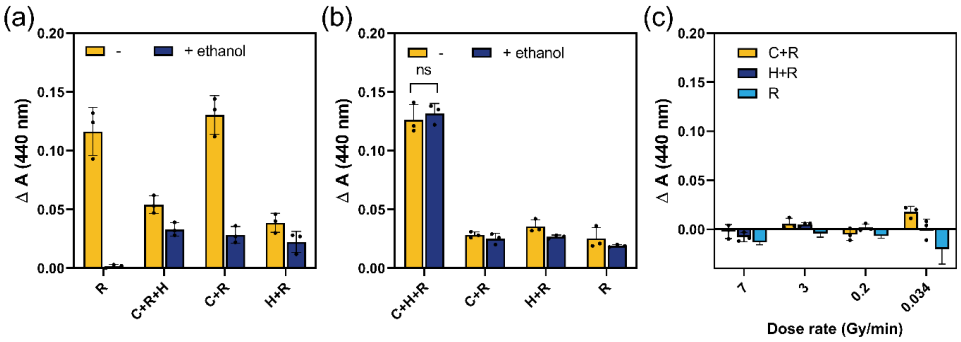

Figure S2.4. RNO bleaching with additional ethanol excludes hydroxyl radical involvement in singlet oxygen formation. (a)The addition of 0.01% ethanol eliminated the decrease in RNO absorption. Samples were irradiated by X-rays for 70 Gy at a dose rate of 7 Gy/min. (b) Decrease in RNO absorption after 5 Gy X-ray radiation at a dose rate of 0.005 Gy/min in presence and absence of 0.01% ethanol. (c) Decrease in RNO absorption after 5 Gy X-ray irradiation at dose rates of 7 Gy/min, 3 Gy/min, 0.2 Gy/min and 0.034 Gy/min with or without Ce6 in presence of 0.01% ethanol. R samples contained 50 µM RNO; C+H+R samples contained 40 µM Ce6, 10 mM L-histidine and 50 µM RNO; C+R samples contained 40 µM Ce6 and 50 µM RNO; H+R samples contained 10 mM L-histidine and 50 µM RNO. ΔA denotes the difference between the absorption of RNO before and after irradiation. pH was set to 7.4 using PB buffer. All data are represented as mean ± SD and analyzed by two-way ANOVA (B); n = 3.

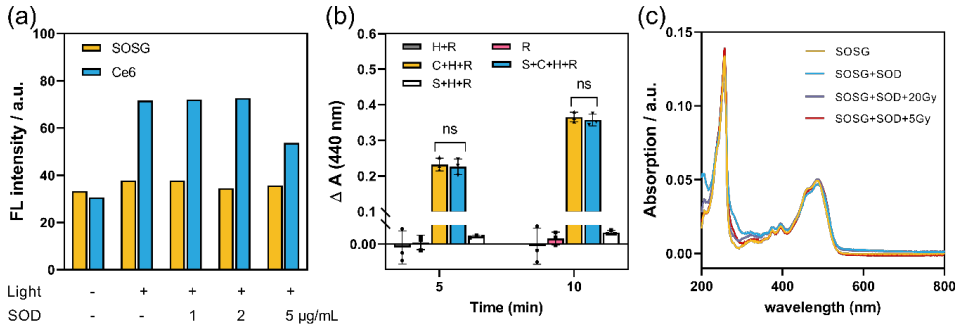

Figure S2.5. The addition of SOD does not affect the response of either SOSG or RNO. (a) Behavior of SOSG as a function of SOD concentration in presence or absence of Ce6 under sunlight exposure. [Ce6] = 5 μM; [SOSG] = 5 μM. (b) The effect of SOD on the bleaching of RNO in presence and absence of Ce6 under sunlight exposure. H+R samples contained 10 mM L-histidine and 50 μM RNO; R samples contained only 50 μM RNO; C+H+R samples contained 10 μM Ce6, 10 mM L-histidine and 50 μM RNO; S+C+H+R samples contained 1 μg/mL SOD, 10 μM Ce6, 10 mM L-histidine and 50 μM RNO; S+H+R samples contained 1 μg/mL SOD, 10 mM L-histidine and 50 μM RNO. ΔA denotes the difference between the absorption of RNO before and after irradiation. pH was set to 7.4 using PB buffer. (c) Absorption spectra of SOSG with or without SOD before and after X-ray (5 Gy, 240 kV, 1 mA, 0.005 Gy/min) or γ-ray irradiation (20 Gy, 6.2 Gy/min). [SOSG] = 5 μM; [SOD] = 1 μg/mL. All data are represented as mean ± SD and analyzed by two-way ANOVA (B); n = 3.

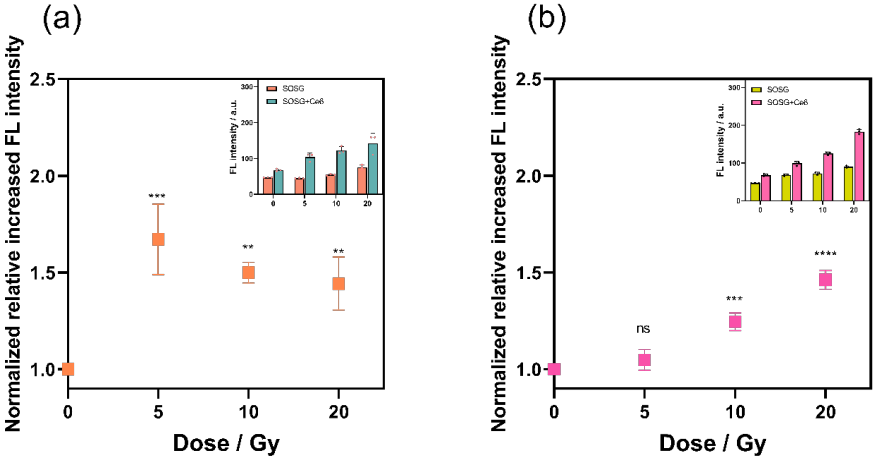

Figure S2.6. X-ray irradiation increases SOSG fluorescence in the presence of Ce6. (a) Samples were irradiated by the X-rays at a dose rate of 0.195 Gy/min. (b) Samples were irradiated by the X-rays at a dose rate of 3 Gy/min. [Ce6] = 5 μM; [SOSG] = 5 μM. All data are represented as mean ± SD and analyzed by one-way ANOVA: **p = 0.0024, ***p ≤ 0.005, ****p < 0.0001; n = 3.

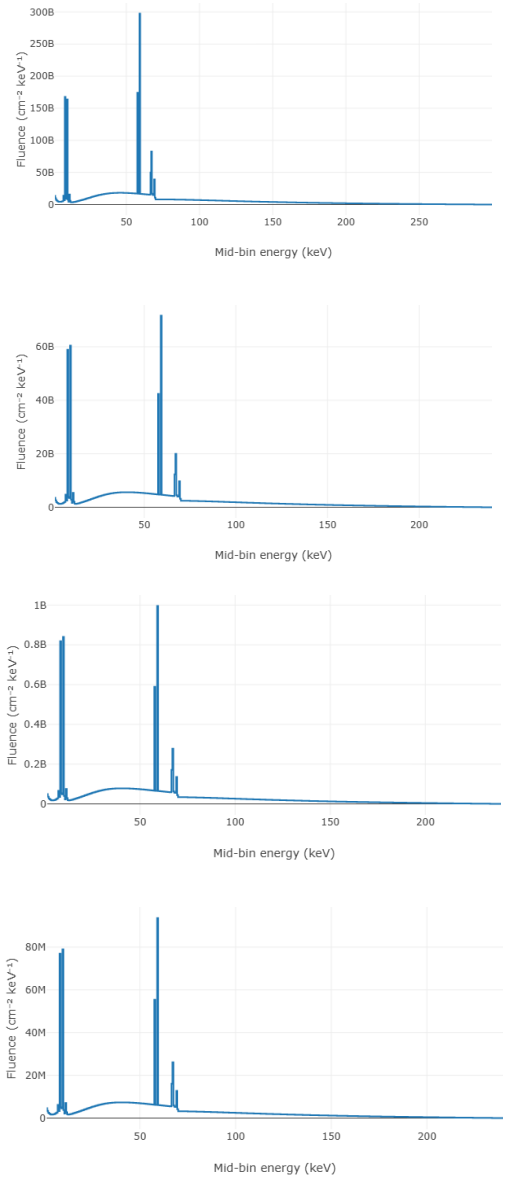

Figure S2.7. Simulation of the energy distribution of the X-ray beam using Spekpy. The order from top to bottom in the illustration corresponds to: 300 kVp, 12 mA at a distance of 11 cm; 240 kVp, 15 mA at a distance of 21 cm, 240 kVp, 1 mA at a distance of 46 cm and 240 kVp, 1 mA at a distance of 1.5 m, respectively.

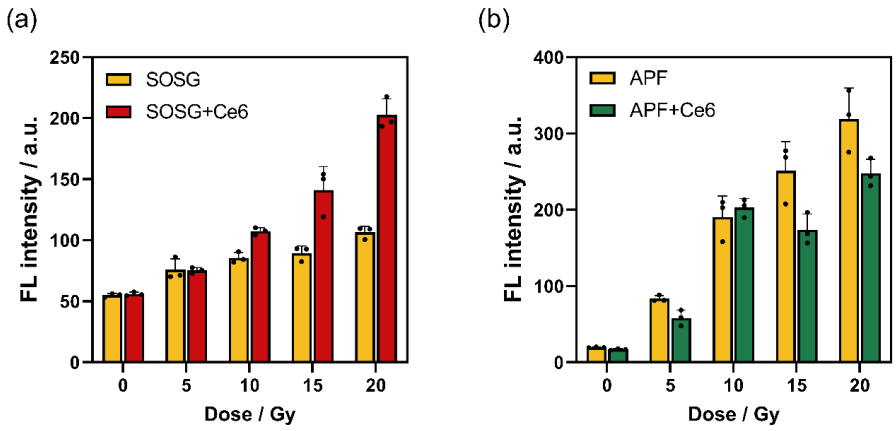

Figure S2.8. X-ray irradiation increases SOSG fluorescence in the presence of Ce6, whereas APF shows no increase. X-ray settings: 240 kV, 5 mA, 0.65 Gy/min. (a) Fluorescence intensity of SOSG, reflecting singlet oxygen formation. (b) Fluorescence intensity of APF, reflecting hydroxyl radical formation. [Ce6] = 5 µM; [SOSG] = 5 µM; [APF] = 2.5 µM; n = 3.

Chapter 3

Radiodynamic Therapy Using Iodine-125 and Chlorin e6: Impact of Gold Nanoparticles and Component Conjugation

Abstract

Radiodynamic therapy (RDT) uses ionizing radiation to activate photosensitizers (PSs) to enhance the generation of reactive oxygen species and provide new treatment modality for cancer. However, how radiation transfers energy to PSs remains unclear, with two proposed mechanisms: direct excitation by electrons generated by radiation or radiation-induced ionization followed by electron transfer between ionized PSs and water radiolysis products. To distinguish between these pathways, we exposed Chlorin e6 (Ce6) to either Auger electrons or low-energy X-rays and gamma rays by using iodine-125 (^{125}I) in different experimental setups. For photon irradiation, we simply mixed [^{125}I]NaI with Ce6 solutions. To expose Ce6 to Auger electrons, we used gold nanoparticles (AuNPs) as platforms to carry ^{125}I and conjugate Ce6 on their surface, placing Ce6 within the Auger electron emission region. When [^{125}I]NaI was added to Ce6 solutions, singlet oxygen formation and cell killing were observed. Simply mixing ^{125}I-radiolabeled AuNPs with Ce6 solutions also produced efficient cell killing, to a greater extent than observed for [^{125}I]NaI alone, likely because AuNPs deposited more energy in the surrounding medium. In contrast, conjugating Ce6 to ^{125}I-radiolabeled AuNPs showed no cell killing effect. These results suggest that direct electron excitation is not dominant. Instead, the ionization-induced pathway appears more likely, where ionized Ce6 reacts with diffusible radiolysis products. Surface-conjugated Ce6 may suffer from reduced availability to radicals derived by water radiolysis caused by catalytic scavenging of superoxide anions at the AuNP surface. In contrast, free Ce6 dispersed around radiolabeled AuNPs can more easily access radiolysis products generated in the surrounding medium. Further investigation is needed to verify this mechanism.

Keywords: radiodynamic therapy, energy deposition, iodine-125, chlorin e6, gold nanoparticles, electrons

3.1 Introduction

Radiodynamic therapy (RDT) is a promising approach that combines the principles of radiation therapy (RT)[1-3] and photodynamic therapy (PDT)[4,5]. In RDT, high-energy ionizing radiation activates photosensitizers (PSs) to generate cytotoxic reactive oxygen species (ROS), thereby introducing additional ROS-mediated damage that can further enhance the efficacy of radiotherapy.[6-8] This strategy also addresses a key limitation of conventional PDT, where visible light activation restricts treatment to superficial lesions because of limited tissue penetration.[7] Despite these promising features, the mechanism by which deposited radiation energy is converted into PS activation remains poorly understood, and the resulting efficiency is still much lower than that achieved by visible light.

The key question of how ionizing radiation activates photosensitizers has led to two discussed mechanistic possibilities. One hypothesis is the direct excitation pathway, in which electrons generated by radiation excite the photosensitizer in a manner similar to light-based activation. The second and more chemically grounded hypothesis is a radiation induced ionization mechanism, where ionizing radiation first ionizes the photosensitizer, enabling it to act as an electron transfer platform that drives the formation of radicals and ROS.[9] In this case, the photosensitizer does not require electron excitation but participates in radiation initiated chemical reactions. Systems designed to enhance local electron emissions, such as combination of high Z nanoparticles with radionuclides that emit high yields of Auger electrons, have been reported to increase singlet oxygen ($^1O_2$) production when photosensitizers are placed within the effective energy deposition range of Auger electrons, suggesting a possible direct excitation.[10] However, similar activation has also been observed under X-ray irradiation or with gallium-68 (beta plus emitter), where Auger electron yields are low or negligible. These studies suggest that radiation-induced ionization and radiolysis products, and in some cases, Cerenkov light emission, can be the explanation for the observed ROS formation.[11-15]

To examine these mechanistic possibilities, we designed systems that modulate the local electron density around the photosensitizer Chlorin e6 (Ce6). Iodine-125 (^{125}I) was selected as the radiation source because it emits both long-range low linear energy transfer (LET) photons (27.4-31.4 keV) and short-range high-LET Auger electrons (10 eV-10 keV)[16,17], allowing spatial separation of energy deposition at different length scales. To precisely control the placement of ^{125}I relative to Ce6, we employed gold nanoparticles (AuNPs) as carriers. AuNPs offer straightforward and fast radiolabeling of ^{125}I with excellent radiolabel retention[18,19], along

with tunable surface chemistry for Ce6 conjugation. Additionally, the high atomic number of AuNPs enhances local electron emission under irradiation.[20] With ^{125}I on the AuNP surface, Auger and low energy electrons deposit their energy within nanometers, whereas photoelectrons extend over micrometers.[21-23] This design allows us to compare Ce6 activation within and beyond regions of high electron density caused by radiation, thereby identifying the dominant activation mechanism.

In this study, we first examined $^1O_2$ generation and cytotoxicity when [^{125}I]NaI was simply mixed with Ce6 in aqueous solution to evaluate the activation behavior of Ce6 under ^{125}I irradiation. We then introduced AuNPs as carriers of ^{125}I and investigated their cytotoxic effects when combined with Ce6 on HeLa cells using three configurations as shown in Scheme 3.1. In the first system, ^{125}I radiolabeled ultrasmall PEG-coated AuNPs (1.7 nm) were directly mixed with Ce6 solutions and added to HeLa cells. In the second system, BSA-coated AuNPs (10 nm, BSA-Au) were synthesized, and Ce6 was conjugated to the BSA shell (Ce6-Au), positioning it within a few nanometers of the nanoparticle surface. After purification to remove unreacted Ce6, the resulting Ce6-Au nanoparticles were radiolabeled with ^{125}I and added to HeLa cells. As a comparison, ^{125}I radiolabeled BSA-Au was directly mixed with Ce6 solutions and added to HeLa cells.

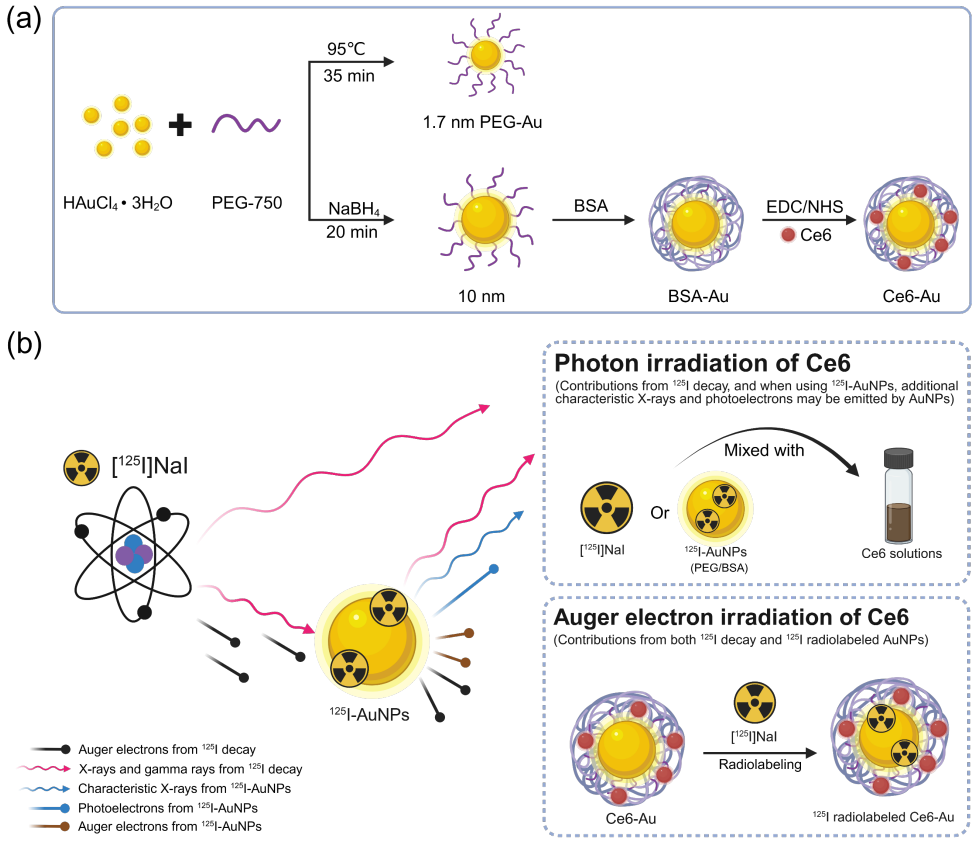

Scheme 3.1. (a) Three AuNP configurations used in this chapter: 1.7 nm PEG-Au, 10 nm BSA-Au, and 10 nm Ce6-Au. (b) A simplified illustration of ^{125}I experimental setups.

3.2 Materials and Method

Materials

Gold(III) chloride trihydrate ($HAuCl_4 \cdot 3H_2O$) and Singlet oxygen sensor green (SOSG) were purchased from Thermo Fisher Scientific. Sodium borohydride powder ($NaBH_4$), crystal violet (1% solution), N-Hydroxysuccinimide (NHS) and N-(3-Dimethylaminopropyl)-N′-ethylcarbodiimide hydrochloride (EDC) were obtained from Merck Sigma. Chlorin e6 (Ce6) was purchased from Bio-connect life sciences. PEG-SH (Mw=750 Da) was purchased from Rapp Polymere. Sodium Iodine-125 (17 mCi/mg, pH 12~14, [^{125}I]NaI) was ordered from Revvity. Cell Counting Kit-8 (CCK8) was purchased from Tebu-Bio. Dulbecco's Modified Eagle Medium (DMEM) and 100X penicillin-streptomycin solution were purchased from VWR chemicals. Fetal bovine serum (FBS) was ordered from Biowest.

Singlet oxygen formation of Ce6 in presence of [^{125}I]NaI

The generation of singlet oxygen was determined using the SOSG probe. In brief, 10 μM Ce6 solution was prepared in Milli-Q (MQ) water by sonication for 20 min. The SOSG probe (10 μM) was prepared by dissolving the powder in 33 μL methanol and diluting with MQ water. Equal volumes (500 μL) of 10 μM Ce6 solution and 10 μM SOSG solution were mixed, together with different activities of [^{125}I]NaI (0.2, 0.8, or 1.6 MBq). Control groups consisted of 500 μL of 10 μM SOSG solution mixed with 500 μL MQ water and the same activity of [^{125}I]NaI. For Samples without [^{125}I]NaI, an equivalent volume of 0.1 M NaOH was added to maintain the same pH. The fluorescence intensity of SOSG was monitored using a Cary Eclipse Fluorescence Spectrophotometer (Agilent Technologies) at an excitation wavelength of 504 nm and an emission wavelength of 524 nm.

Synthesis of AuNPs

Synthesis of 1.7 nm PEG coated AuNPs. 1.7 nm PEG-AuNPs were synthesized following a previously reported thermal reduction approach. Briefly, 25 mL of 2.4 mM PEG_{750}-SH aqueous solution was mixed with 75 μL of 1 M $HAuCl_4$ in a 2-neck round flask covered with aluminum foil under vigorous stirring for 30 min at room temperature. Afterwards, the flask was placed in an oil bath at 95 °C and stirred vigorously for 35 minutes. The resulting PEG-AuNPs were collected and filtered through a 220 nm syringe filter to remove the large aggregates. Unreacted reagents and small ligands were removed using centrifuge filters (Amicon®, MWCO 10,000) at 4000 rpm, and the nanoparticles were washed three times with MilliQ water (MQ water). The final solution was concentrated to 2 mL and stored at 4 °C.

Synthesis of 10 nm PEG coated AuNPs. 10 nm PEG-AuNPs were synthesized via the $NaBH_4$ reduction method. In brief, 2 mL of 2.4 mM PEG_{750}-SH aqueous solution was mixed with 3 mL Milli-Q water and stirred for 10 min. Subsequently, 150 µL of 0.1 M $HAuCl_4$ was injected via syringe, and the mixture was stirred vigorously for 15 min at room temperature until the color changed from yellow to pale yellow. 0.5 mL of 0.05 M $NaBH_4$ was rapidly injected and the solution immediately changed to a wine-red colloid. After 5 min of stirring, additional 0.5 mL of 0.05 M $NaBH_4$ was added dropwise, gradually changing the solution to saffron-red. The mixture was stirred for 20 min to allow complete reaction. Subsequently, the PEG-AuNPs solution was filtered through a 0.22 µm syringe filter to remove large aggregates, then purified twice using a spin filter (30,000 MWCO) at 3500 rpm to eliminate excess PEG_{750}-SH and $NaBH_4$. The final volume was adjusted to 4 mL, and the PEG-AuNPs was stored at 4 °C.

Synthesis of BSA coated AuNPs. Bovine serum albumin (BSA) was used to modify the surface of 10 nm AuNPs. Briefly, 0.5 mL of 2 mg/mL BSA aqueous solution was mixed with 4 mL of 10 nm PEG-AuNP solution and stirred vigorously overnight at room temperature. The resulting mixture was then collected and further purified twice by a spin filter (30,000 MWCO), followed by passage through a PD-10 column with 50 mM HEPES buffer (pH 7.4) as the exchange buffer. After purification, the BSA-Au solution was stored at 4 ℃ for further use.

Synthesis of Ce6 conjugated AuNPs. Chlorin e6 (Ce6) was conjugated to the amine groups of BSA on the surface of AuNPs via EDC/NHS coupling reaction. Briefly, 2.5 mg of Ce6 was dissolved in 500 µL DMSO and mixed with 2 mL of 40.7 mg/mL NHS solution (10 mM, pH 6.2 MES buffer) for 20 minutes at room temperature. Afterwards, 3 mL of 16 mg/mL EDC solutions (10 mM, pH 6.2 MES buffer) was added dropwise to the Ce6/NHS mixture under gentle stirring. The reaction was mixed every 5 minutes over a period of 30 minutes. The activated Ce6 solution was then added to 4 mL of BSA-AuNP solutions and stirred overnight at room temperature. The resulting mixture was then collected and further purified twice by a spin filter (30,000 MWCO), followed by passage through a PD-10 column with MQ water as the exchange buffer. After purification, the Ce6-Au solution was stored at 4 ℃ for further use.

Characterization

The morphology and dimensions of AuNPs were characterized via a 120 kV JEM-1400 Plus transmission electron microscope (TEM, JEOL). Hydrodynamic diameter and zeta-potential measurements were performed on a Zeta sizer (nano-ZS, Malvern). The absorption spectrum was measured by a UV-VIS-NIR spectrophotometer (UV-6300PC, VWR). The concentration of PEG-Au, BSA-Au and Ce6-Au were measured using ICP-MS spectrum (NexION®, Perkin

Elmer) by dissolving samples in aqua regia and 1% HCl.

Radiolabeling of ^{125}I on PEG-Au, BSA-Au and Ce6-Au

The radiolabeling of ^{125}I onto the AuNPs was achieved via chemisorption according to our previously published paper[18]. Typically, the desired activity of [^{125}I]NaI solution needed for experiments was first taken out from the stock solution stored in 0.1 M NaOH (pH 12–14) and then neutralized by adding an equivalent volume of 0.1 M HCl. The neutralized ^{125}I solution was subsequently mixed with each type of AuNP solution. For 1.7 nm PEG-Au, a molar ratio of [$^{125}I^-$] to [AuNPs] of 1:10 was used, while for 10 nm BSA-Au and Ce6-Au, a molar ratio of 14:1 was applied. The mixtures were incubated on a thermoshaker at 37 °C and shaken at 800 rpm for 30 minutes to facilitate chemisorption.

The radiolabeling efficiency was confirmed by instant thin-layer chromatography iTLC using 0.9% saline (0.9 % NaCl) as the mobile phase and imaged on a Typhoon Trio phosphor imager (GE Healthcare). Radiolabeled AuNPs remained at its origin, whereas free ^{125}I migrated to the top of the iTLC strip. The radiolabeling efficiency was analyzed using both ImageQuant TL software (GE Healthcare) and an automatic gamma counter (Wallac Wizadrd2 2480, Perkin Elmer).

Radiochemical stability

Radiolabeled AuNPs (PEG-Au, BSA-Au, and Ce6-Au) were incubated in either PBS (10 mM, pH 7.4) or PBS containing 10 % FBS at 37 °C for 3 h, 24 h and 48 h. The desorption of ^{125}I from AuNPs was evaluated by iTLC at each time point and analyzed using a Wallac gamma counter.

Cell Culture

HeLa cells were kindly provided by Erasmus MC and cultured in DMEM (VWR chemicals), supplemented with 10% fetal bovine serum (Biowest) and 1X penicillin-streptomycin solution (VWR chemicals) in a cell incubator (Heracell®, Heraeus) at a humidified atmosphere containing 5% CO_2 at 37 ºC.

Cellular uptake of Ce6 and Ce6-Au in HeLa cells

A stock solution of 2.5 mg/mL Chlorin e6 was prepared in PBS (pH 7.4), protected from light and stored at -20 ºC. Cells were seeded at a density of 4×10^4 cells per well in 8-well chambered coverslips (Ibidi) overnight. Two experimental groups were established to compare cellular uptake of free Ce6 and Ce6-Au. Both treatments were prepared to deliver equivalent Ce6 concentrations of 10 µg/mL in the final solution. Stock solutions of 10 µg/mL Ce6 were freshly

prepared by diluting the stock solution in DMEM supplied with 2.5% FBS, while Ce6-Au were added based on their Ce6 content to achieve the same final Ce6 concentration. 200 µL of each solution was incubated with HeLa cells for 1 h, 3 h and 24 h at 37 ºC. Following incubation, the culture medium containing Ce6 or Ce6-Au was removed and cells were washed three times with PBS. Cells were then fixed with 4% paraformaldehyde in PBS (Thermo Fisher Scientific) for 15 minutes at room temperature in the dark. Cell nuclei were stained with Hoechst 33342, and Ce6 fluorescence was visualized using confocal microscopy (LSM 980, ZEISS) with an excitation wavelength of 405 nm and emission detection at 663 nm.

Cellular uptake of ^{125}I radiolabeled AuNPs

HeLa cells were seeded at a density of 5×10^5 cells per well in 12-well plates and incubated overnight prior to treatment. Cells were then treated with 50 kBq of either ^{125}I-BSA-Au or ^{125}I-Ce6-Au and incubated for 1 h, 3 h and 24 h at 37 ºC. Following incubation, cells were washed three times with PBS (1 mL per wash) and the washing fractions were collected. The remaining adherent cells were lysed with 1 mL of 0.1 M NaOH, and the lysates were collected, followed by two additional PBS washes. All collected samples were counted using an automated gamma counter (Wallac Wizard^2 2480, Perkin Elmer).

In vitro cell viability assay

HeLa cells were seeded at a density of 4,000 cells per well in 96-well plates and incubated overnight. For Ce6 + [^{125}I]NaI treatment, HeLa cells were pre-incubated with 10 µg/mL Ce6 for 4 h, then exposed to various activities of [^{125}I]NaI in fresh complete DMEM for 48 h. To assess the cytotoxicity of Ce6 in DMEM supplemented with 2.5% FBS, cells were treated with various concentrations of Ce6 (0.5–40 µg/mL) for 72 h and cell viability was determined by CCK-8 assay. The effect of Ce6 in the presence of 1.7 nm PEG-Au and 10 nm BSA-AuNPs was examined by adding a mixture of AuNPs with 10 µg/mL Ce6, while for Ce6-Au, various concentrations were tested. For combined treatments, cells were incubated for 48 h with ^{125}I-radiolabeled AuNPs at a constant radioactivity of 0.8 MBq and Au concentration of 40 µg/mL in 2.5% FBS DMEM. Cells treated with ^{125}I-radiolabeled 1.7 nm PEG-Au received either nanoparticles alone or nanoparticles together with 10 µg/mL Ce6 to evaluate the synergistic cytotoxicity of radiation and photosensitizer. For 10 nm AuNPs, cells were treated with ^{125}I-labeled BSA-Au at a constant radioactivity of 0.8 MBq and 10 µg/mL free Ce6 solution, or with ^{125}I-labeled Ce6-Au carrying 10 µg/mL Ce6 bound to BSA on the nanoparticle surface in 2.5% FBS DMEM.

Clonogenic assay

HeLa cells were seeded at a density of 3×10^4 cells per well in 48-well plates and incubated overnight. Cells were then pre-treated with 500 µL of 10 µg/mL Ce6 solution for 4 h, then exposed to various activities of [^{125}I]NaI in fresh complete DMEM for 48 h. Control groups were treated with either 10 µg/mL Ce6 solution alone or 1.6 MBq [^{125}I]NaI alone. Subsequently, cells were trypsinized, counted, and reseeded in 6-well plates at a density of 200 cells per well for all groups. Colonies were allowed to grow for 8 days, then washed twice with PBS, fixed with 4% paraformaldehyde, and stained with 1% crystal violet before being counted manually.

Statistical analysis

Data with error bar were presented as mean ± SD. Statistical analyses were performed using either one-way or two-way ANOVA as appropriate. GraphPad Prism software (version 8.00) was used for statistical analysis and data visualization. $P < 0.05$ was considered statistically significant.

3.3 Results and discussion

Radionuclides such as ^{68}Ga,^{89}Zr and ^{64}Cu, which can generate Cerenkov light, have been employed as internal light source to excite PSs to their triplet state, thereby generating cytotoxic ROS and $^1O_2$.[11,24,25] However, therapeutic efficacy has also been reported in the absence of Cerenkov light, for example with radionuclides such as ^{125}I, where $^1O_2$ generated by PS has been attributed to direct excitation by Auger electrons generated under irradiation.[10,13] In contrast, findings in Chapter 2 suggest that photosensitizer may undergo radiation-induced ionization followed by electron transfer reactions with water radiolysis products (i.e. superoxide anions ($\cdot O_2^-$)) rather than direct excitation by electrons. Despite these observations, mechanistic insights into how PSs respond to ionizing radiation are still limited, and further investigation is needed. Here, we employ ^{125}I and AuNPs to modulate the local radiation environment around Ce6 and investigate the dominant activation pathway.

To verify whether Ce6 can be activated by radiation in the absence of Cerenkov light emission, we first examined the $^1O_2$ formation in the presence of free ^{125}I. The SOSG probe was used to assess $^1O_2$ formation. Ce6 solutions were incubated with varying activities of [^{125}I]NaI for 24 h, while SOSG in Milli-Q water with the same activities of [^{125}I]NaI were set as control. For 0.2 MBq of ^{125}I, no significant increase in SOSG fluorescence was observed, whereas at 0.8 MBq and 1.6 MBq, a pronounced increase was detected ($p = 0.0055$ and $p = 0.0017$,

respectively). The SOSG fluorescence at 0 h was also measured to ensure that the addition of ^{125}I did not affect the SOSG fluorescence (Fig. S3.1). Since ^{125}I emits Auger electrons and photons with a maximum energy of 35 keV, which is below the threshold for generating Cerenkov light in water, any observed $^1O_2$ production cannot be attributed to Cerenkov light activation of Ce6. These results demonstrate that in the presence of ^{125}I, Ce6 produces $^1O_2$ through a mechanism that is independent of Cerenkov light. A slight decrease in SOSG fluorescence was observed after adding [^{125}I]NaI compared to samples without [^{125}I]NaI. This decrease was most likely not due to radiation effects of ^{125}I but rather to differences in pH. Since SOSG exhibits stronger fluorescence under more alkaline conditions[26] and [^{125}I]NaI was stored in 0.1 M NaOH (pH ~ 12-14), adding [^{125}I]NaI inevitably raised the pH of the solution. To match the pH among all samples, the same volume of 0.1 M NaOH was added to the controls without [^{125}I]NaI. However, the NaOH solution we prepared was slightly more basic than that in the commercial [^{125}I]NaI, resulting in higher fluorescence in the samples without [^{125}I]NaI.

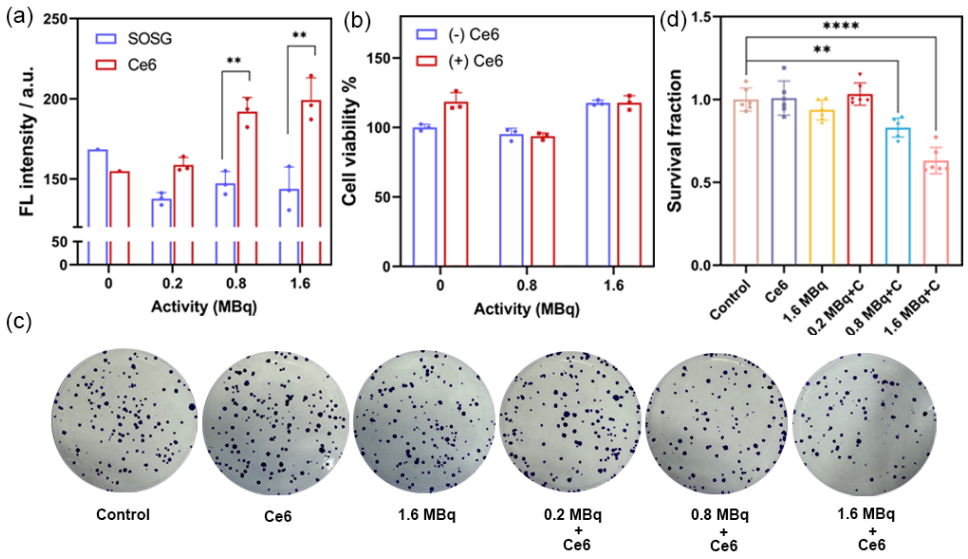

Figure 3.1. (a) Fluorescence intensity changes of SOSG in presence of Ce6 mixed with varying activities of [^{125}I]NaI after 24 h incubation; [Ce6] = 5 µM; n = 3. (b) Cytotoxicity to HeLa cells treated with Ce6 and [^{125}I]NaI after 48 h incubation; [Ce6] = 10 µg/mL; n = 3. (c) Representative images of Clonogenic formation of HeLa cells treated with Ce6 and 0.2, 0.8 or 1.6 MBq [^{125}I]NaI; [Ce6] = 10 µg/mL. (d) Survival fraction of HeLa cells treated with Ce6 and varying activities of [^{125}I]NaI; [Ce6] = 10 µg/mL; n = 6. All data are represented as mean ± SD and analyzed by two-way ANOVA (a) or one-way ANOVA (d); **$p < 0.01$, ****$p < 0.0001$.

After confirming the $^1O_2$ formation by Ce6 under ^{125}I irradiation, we next evaluated the cytotoxic effect of the combined treatment with Ce6 and [^{125}I]NaI in HeLa cells. As reported previously, albumin in fetal bovine serum (FBS) can bind Ce6 and reduce its cellular uptake (Fig. S3.2).[27] Therefore, culture medium without FBS was used to maximize uptake. After 4 h incubation, excess Ce6 was washed away and cells were incubated with various activities of [^{125}I]NaI for 48 h. Cell viability assessed by the CCK-8 assay showed that Ce6 treated cells had slightly higher viability than untreated controls (Fig. 3.1(b)), possibly due to a temporary increase in metabolic activity.[28] When HeLa cells were incubated with Ce6 together with 0.8 MBq or 1.6 MBq [^{125}I]NaI, no cytotoxicity was observed (Fig. 3.1(b)). Because short-term viability assays may not accurately reflect cytotoxicity, we performed clonogenic assays to evaluate long-term survival (representative colonies in Figure 3.1(c)). Ce6 alone or 1.6 MBq [^{125}I]NaI had no effect on colony formation (Fig. 3.1(d)). In contrast, the combination of Ce6 with 0.8 MBq [^{125}I]NaI reduced the survival fraction to 0.83 ($p = 0.0054$), and further to 0.63 ($p < 0.0001$) at 1.6 MBq. The clonogenic assay results demonstrated a clear ^{125}I dose-dependent radiosensitizing effect, consistent with the singlet oxygen generation shown in Figure 3.1(a).

The spatial separation between ^{125}I and Ce6 in our experiments provide some mechanistic insights. Although ^{125}I is traditionally considered an Auger electron emitter, its decay produces a broad spectrum of low-energy radiation, including Auger electrons, conversion electrons, characteristic X-rays, and γ-rays. The emitted electrons cover a wide energy range from approximately 50 eV to 35 keV.[29] The majority of Auger electrons possess energies below 5 keV and deposit that energy within a few to several hundred nanometers in biological tissue. The most energetic electrons, including some Auger and conversion electrons in the 20-35 keV range, can extend their penetration to approximately 0.5-1 μm[30,31]. Because HeLa cells lack expression of the sodium-iodide symporter (NIS), the cellular uptake of free ^{125}I is minimal[32,33], meaning that most ^{125}I decays occur extracellularly or near the cell membrane. In our experiments, HeLa cells grew as a monolayer, with dimensions of approximately 20-50 μm and a thickness of ~ 1-3 μm[34-36], the emitted electrons are largely confined to their point of origin, depositing energy locally near the decay site rather than traversing the entire cell. However, the cascade of secondary reactions initiated by these electrons, including water radiolysis and subsequent formation of radicals such as $\cdot O_2^-$ and $\cdot OH$[37], cannot be excluded from contributing to local physicochemical changes that may influence Ce6 activation.

In addition to electrons, ^{125}I decay also emits low-energy photons, primarily characteristic X-rays and γ-rays in the range of 27-35 keV. These photons have significantly greater penetration

depths in biological media compared to electrons and may therefore contribute to long-range energy deposition within cells.[38] Considering this, it is plausible that the observed enhancement in Ce6-mediated cytotoxicity arises not solely from localized Auger or conversion electron, but also from the energy deposited by low-energy photons emitted by ^{125}I, which can further generate secondary electrons or ROS to promote additional $^1O_2$ generation.

To further investigate this mechanism, high-Z elements were introduced as radiosensitizers. Due to their high atomic number and electron density, these elements efficiently absorb low-energy photons and emit large numbers of secondary electrons, thereby enhancing local dose deposition.[39,40] Among them, gold has been extensively studied and is well recognized for its strong radiosensitizing capability.[20] Consequently, AuNPs were selected as secondary electron generators. Under ^{125}I irradiation, AuNPs generate three types of emissions with distinct ranges: Auger and delta electrons (~few micrometers), photoelectrons (~several micrometers), and characteristic X-rays (longer range).[14] To examine the spatial dependence of Ce6 activation by these emissions, we compared two different systems: ^{125}I radiolabeled AuNPs with free Ce6 (variable distance) versus ^{125}I radiolabeled AuNPs conjugated with Ce6 (fixed distance).

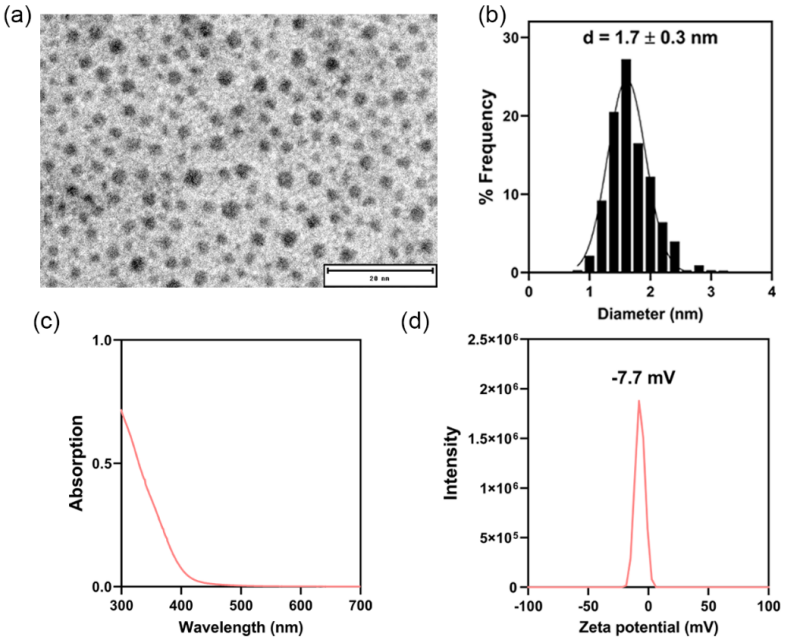

Figure 3.2. Characterization of 1.7 nm PEG-Au. (a) TEM image of the synthesized 1.7 nm PEG-Au. Scale bar = 20 nm. (b) Size distribution of PEG-Au calculated from TEM images. (c) UV-vis spectrum. (e) Zeta potential. All data are represented as mean ± SD.

Due to the low-energy radiation emitted by ^{125}I, smaller AuNPs are beneficial for generating more secondary electrons, as their reduced dimensions facilitate the escape of electrons into the surrounding medium.[41,42] To obtain ultrasmall AuNPs, PEG coated AuNPs (PEG-Au) were synthesized via thermal reduction of $HAuCl_4$ in the presence of PEG_{750}-SH according to previously published methods.[43] TEM images confirmed that the ultra-small AuNPs had a diameter of 1.7 ± 0.3 nm (Fig. 3.2(a) and Fig. 3.2(b)). UV-Vis absorption spectroscopy showed no distinct peak at 500 nm, confirming the small size of the AuNPs (Fig. 3.2(c)). The nanoparticles exhibited a zeta potential of -7.7 mV (Fig. 3.2(e)).

To enable the attachment of Ce6 onto the nanoparticle surface, larger AuNPs with an average diameter of 10.2 ± 1.8 nm were synthesized via reduction of $HAuCl_4$ with sodium borohydride ($NaBH_4$) in the presence of PEG_{750}-SH (Fig. 3.3(a) and Fig. 3.3(b)), following the procedure described in previous publications.[15] The resulting red-wine-colored solution indicated successful nanoparticle formation. These AuNPs were subsequently coated with BSA (BSA-Au), providing surface amino groups for conjugation with the carboxyl groups of Ce6 through an EDC/NHS coupling reaction[23]. After Ce6 loading, the solution colour changed to pink-brown. The UV-Vis absorption spectra displayed a distinct absorption peak at 525 nm for BSA-Au samples, which is a typical absorption peak for 10 nm AuNPs[44]. After loading Ce6 onto the BSA-coated AuNPs (Ce6-Au), the peak at 525 nm remained, while additional characteristic absorption bands appeared at 440 nm and 660 nm, corresponding to the Soret and Q bands of Ce6, respectively (Fig. 3.3(c)). These observations confirm the successful conjugation of Ce6 to BSA on the surface of AuNPs[13]. The zeta potential measurements further supported this result (Fig. 3.3(d)), showing a shift from -9.97 ± 0.82 mV for 10 nm PEG-Au to -10.73 ± 0.41 mV for BSA-Au and -27.11 ± 1.01 mV for Ce6-Au[13]. The concentration of conjugated Ce6 was calculated according to the Ce6 calibration curve (Fig. S3.4). Representative TEM images of BSA-Au and Ce6-Au are shown in Figure S3.3.

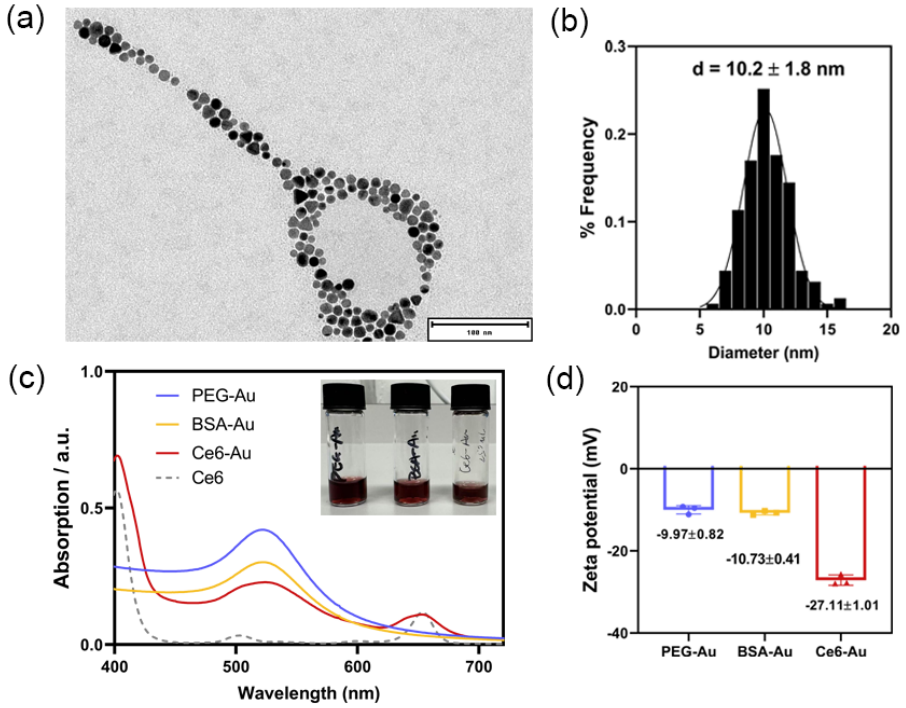

Figure 3.3. Characterization of 10 nm AuNPs with different surface modifications. (a) TEM images of synthesized 10 nm PEG-Au. Scale bar = 100 nm. (b) Size distribution of PEG-Au calculated from TEM images. (c) UV-vis spectrum of synthesized PEG-Au, BSA-Au, Ce6-Au and free Ce6 solutions. Photographs of PEG-Au, BSA-Au, and Ce6-Au are shown from left to right. (d) Zeta potential of PEG-Au, BSA-Au, Ce6-Au. All data are represented as mean ± SD.

After successfully synthesizing 1.7 nm PEG-Au and 10 nm BSA-Au and Ce6-Au, both types of nanoparticles were radiolabeled with ^{125}I via chemisorption using a method similar to that previously reported for 1.7 nm PEG-Au[19]. The procedures for radiolabelling and the radiochemical stability of ^{125}I labelled 1.7 nm PEG-Au have been described in detail in our earlier publication, where the labeling yield exceeded 92.5%, and the compound remained stable in PBS containing 10% FBS for up to 72 h, achieving a radiolabeling efficiency of 85%.[18] Therefore, these results are not repeated here. For the newly synthesized larger nanoparticles, the radiolabeling efficiency was determined to be 99% for both BSA-Au and Ce6-Au (Fig. 3.4(a)). The radiochemical stability results indicated that BSA-Au remained highly stable in both PBS and PBS containing 10% FBS, with 97% and 94% of ^{125}I retained after 48 h, respectively. However, Ce6-Au NPs showed good stability in PBS, with 96% of ^{125}I remaining bound, but lower stability in PBS containing 10% FBS, where 84% of ^{125}I remained on the

nanoparticle surface after 48 h (Fig. 3.4(b)).

The cellular uptake of ^{125}I radiolabeled BSA-Au and Ce6-Au was evaluated in HeLa cells. A total of 50 kBq of ^{125}I-BSA-Au or ^{125}I-Ce6-Au was incubated with the cells for 3, 24, and 48 h at 37 °C. The uptake exhibited a clear time-dependent trend, with increasing internalization observed at longer incubation times (Fig. 3.4(c)). When comparing the uptake of BSA-Au and Ce6-Au, no significant difference was observed.

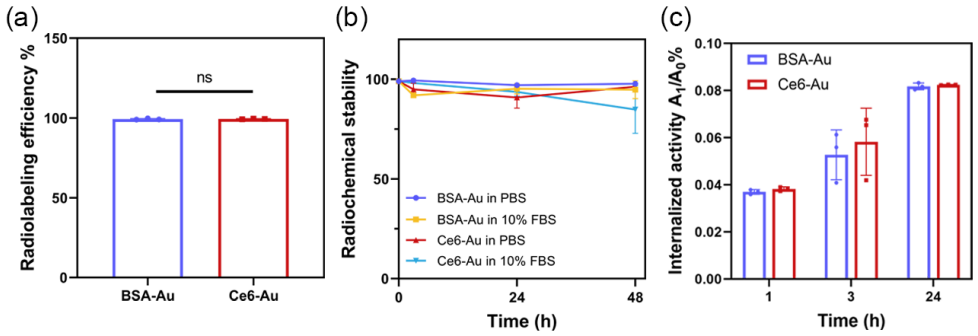

Figure 3.4. (a) Radiolabeling efficiency of ^{125}I-BSA-Au and ^{125}I-Ce6-Au. (b) Radiochemical stability of ^{125}I-BSA-AuNPs and ^{125}I-Ce6-AuNPs in 10 mM PBS buffer (pH 7.4) or in 10 mM PBS (pH 7.4) containing 10% FBS. (c) Internalization of ^{125}I-BSA-AuNPs and ^{125}I-Ce6-AuNPs in HeLa cells after 1 h, 3 h and 24 h incubation. The molar ratio of ^{125}I to BSA-Au or Ce6-Au was ~ 14: 1, and 50 kBq ^{125}I, 2.5 µg/mL Au was used in these experiments. All data are represented as mean ± SD and analyzed by t-test (a) or two-way ANOVA (c); ns indicates no significance.

Subcellular distribution of Ce6-Au (40 µg/mL Au and 10 µg/mL Ce6) was further visualized using confocal microscopy after incubation with HeLa cells for 3, 24, and 48 h (Fig. 3.5). Confocal imaging revealed that Ce6-Au nanoparticles were predominantly localized in the cytoplasm, with no detectable fluorescence in the cell nuclei. The fluorescence signal increased over time, in line with the increasing internalized ^{125}I activity (Fig. 3.4(c)). Notably, the uptake of Ce6-Au was markedly higher than that of free Ce6 at comparable concentrations (10 µg/mL) after 24 h of incubation[45].

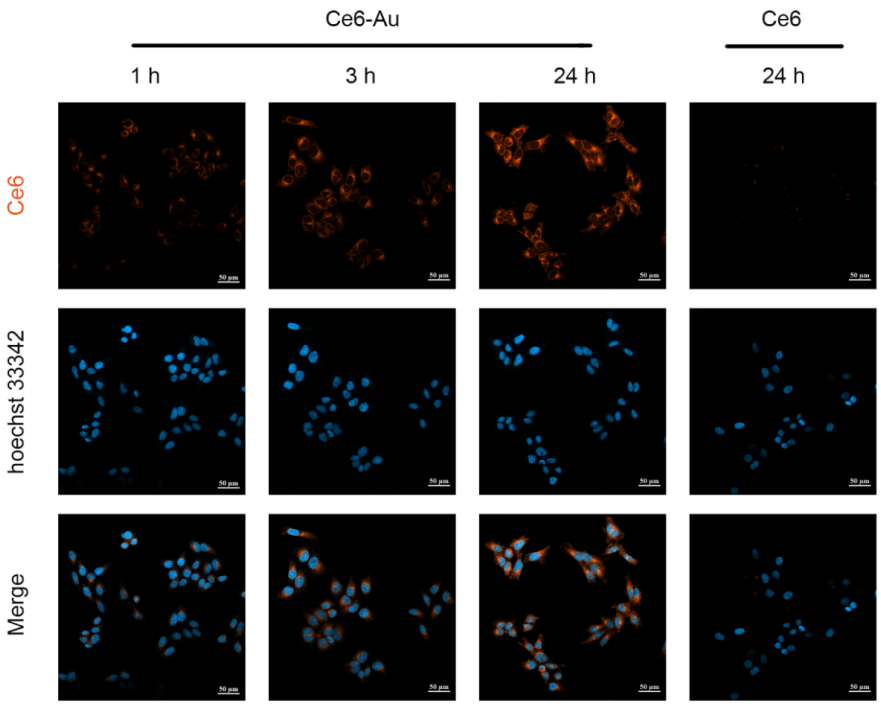

Figure 3.5. Confocal images of the cellular uptake of Ce6-AuNPs and free Ce6 after 1, 3, and 24 h incubation and free Ce6 after 24 h incubation in HeLa cells in 10% FBS DMEM. All images were acquired under the same measurement settings. Concentration of Ce6 loaded on Ce6-Au: ~10 μg/mL; concentration of free Ce6: ~10 μg/mL. Scale bar = 50 μm.

Following the characterization and uptake studies, the biological effects of the radiolabeled nanoparticles were examined. We first investigated the cytotoxicity of ultrasmall 1.7 nm ^{125}I-PEG-Au in combination with free Ce6 to assess whether the presence of PEG-Au enhances the response of Ce6 under low-energy radiation. Prior to radiolabelling, the cytotoxicity of ultrasmall PEG-Au (30, 40, 50 μg/mL) in the presence of 10 μg/mL Ce6 in 2.5% FBS DMEM was examined (Ce6 alone under this reduced-serum condition showed no cytotoxicity up to 72 h, as shown in Figure S3.4). As shown in Figure 3.6(a), PEG-Au and Ce6 together did not reduce cell viability. We then evaluated whether ^{125}I-PEG-Au would have additional toxicity on HeLa cells in the presence of Ce6. To be brief, in cell experiments, 0.8 MBq of ^{125}I was absorbed on 40 μg/mL PEG-Au and incubated with HeLa cells in the presence of 10 μg/mL Ce6 for 48 h in 2.5% FBS DMEM. For comparison, the same amount of 0.8 MBq of ^{125}I-PEG-Au without Ce6 was also tested. As shown in Figure 3.6(b), treatment with Ce6 alone or 0.8 MBq of ^{125}I alone did not result in a significant difference in cell viability compared with the

control group, although a slight increase was observed for their combined treatment. In contrast, cells treated with 0.8 MBq of ^{125}I-PEG-Au showed reduced viability to 65% ($p < 0.0001$ compared to control groups). This result is consistent with our previous findings that PEG-Au facilitates the delivery of ^{125}I to the cell nucleus, where Auger electrons emitted from both ^{125}I and PEG-Au directly damage the DNA. Notably, when cells were treated with 0.8 MBq of ^{125}I-PEG-Au together with Ce6, viability further decreased to only 35% ($p < 0.0001$ compared to control groups, $p = 0.0002$ compared to ^{125}I-PEG-Au groups). This indicates a synergistic effect between ^{125}I-PEG-Au and Ce6.

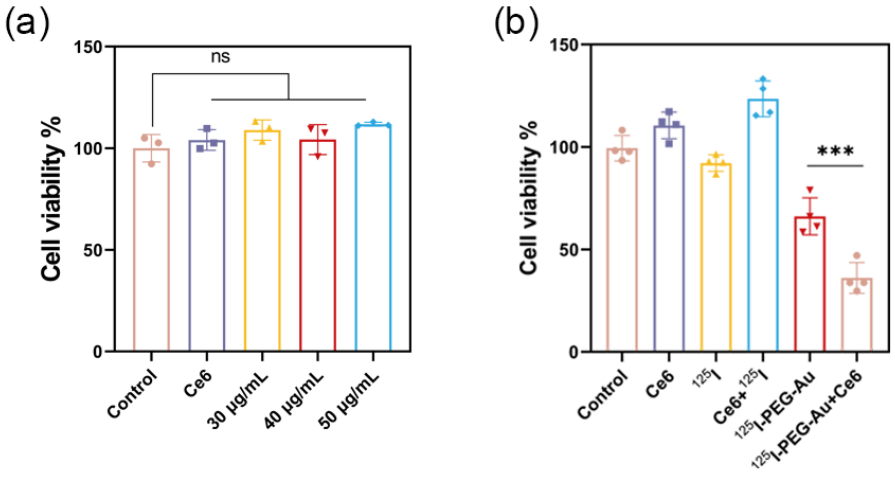

Figure 3.6. Cytotoxicity of Ce6 combined with 1.7 nm PEG-Au on HeLa cells after 48 h incubation (a) Cytotoxicity of Ce6 (10 μg/mL) mixed with varying concentrations of 1.7 nm PEG-Au (40 μg/mL), n = 3. (b) Cytotoxicity comparison of ^{125}I-radiolabeled PEG-Au (40 μg/mL) with or without Ce6 (10 μg/mL), including control groups of Ce6 (10 μg/mL) alone, [^{125}I]NaI (0.8 MBq) alone, and Ce6 (10 μg/mL) + [^{125}I]NaI (0.8 MBq), n = 4. The molar ratio of ^{125}I to PEG-Au was ~ 10: 1. All data are represented as mean ± SD and analyzed by one-way ANOVA; ns indicates no significance, ***$p < 0.001$.

After observing a synergistic cytotoxic effect from the combination of ultrasmall ^{125}I-PEG-Au and free Ce6, we next examined whether a similar enhancement could be achieved with the ^{125}I radiolabeled Ce6-Au in 2.5% FBS DMEM. As shown in Figure 3.7(a), treatment with 0.8 MBq ^{125}I-Ce6-Au, where Ce6 was conjugated to the BSA shell on ^{125}I radiolabeled nanoparticle surface (40 μg/mL Au and 10 μg/mL Ce6) maintained a high viability of 94%. In contrast, co-incubation of 0.8 MBq ^{125}I-BSA-Au (40 μg/mL) with freely distributed Ce6 (10 μg/mL) in 2.5% FBS DMEM resulted in a marked decrease in cell viability reaching 52% ($p = 0.0008$ compared to control groups). In addition, ^{125}I-BSA-Au alone did not induce significant cytotoxicity,

indicating that the effects arise from the combination with freely distributed Ce6 rather than the radiolabeled nanoparticles. For comparison, neither the mixture of Ce6, ^{125}I, and BSA-Au (Fig. 3.7(b)) nor that of Ce6-Au or Ce6-Au + ^{125}I exhibited significant cytotoxicity (Fig. S3.5 and Fig. S3.6).

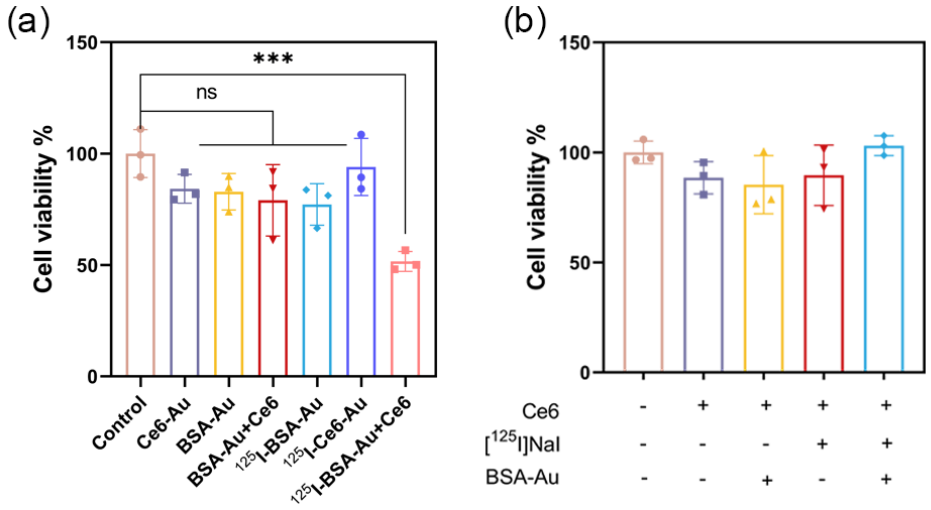

Figure 3.7. Cytotoxicity of different combinations of ^{125}I, AuNPs and Ce6 in HeLa cells. (a) Cytotoxicity of radiolabeled systems, including ^{125}I-Ce6-Au (Ce6 conjugated to nanoparticle surface) and ^{125}I-BSA-Au + Ce6. In both conditions, the Ce6 concentration was ~10 µg/mL and the Au concentration was 40 µg/mL, n = 3. The molar ratio of ^{125}I to BSA-Au or Ce6-Au was ~ 14: 1. (b) Cytotoxicity when Ce6 (10 µg/mL), BSA-AuNPs (40 µg/mL) and 0.8 MBq [^{125}I]NaI were added separately to HeLa cells, n = 3. All data are represented as mean ± SD and analyzed by one-way ANOVA; ns indicates no significance, ***p < 0.001.

Taken together, our results indicate that ^{125}I in combination with Ce6 induces cell killing in a dose-dependent manner. Radiolabeling ^{125}I onto AuNPs further enhances this effect in the presence of Ce6, whereas confining Ce6 near the surface of AuNPs is not needed to observe reduced viability. These findings suggest that the enhancement may arise from secondary processes initiated by electrons or photons emitted from ^{125}I and ^{125}I-labeled AuNPs, rather than from the direct energy deposition or direct excitation of Ce6 molecules by electrons. This behavior is different from that reported by Tu et al.[10], who developed porphyrin-engineered ^{125}I-nanoseeds composed of a core-shell Au@Ag (~ 82 nm) structure coated with a ~24 nm porphyrin-based covalent organic framework (COF) shell. Their Monte Carlo simulations indicated that nearly all Auger electrons deposited their energy within the COF shell, suggesting that the observed $^1O_2$ enhancement mainly arose from direct excitation of porphyrin

molecules by Auger electrons that originated from both ^{125}I decay and secondary emissions of the AuNPs under irradiation. However, their model mainly accounted for the local energy deposition of these electrons and neglected the contribution of photoelectrons generated through photoelectric absorption of ^{125}I emitted low-energy photons by AuNPs. Although these photons themselves do not deposit energy within the COF shell, the photoelectrons produced by AuNPs have much longer penetration ranges and can deposit energy beyond a single COF shell, potentially influencing neighboring porphyrin shells.[14] Moreover, their study lacked a control group in which ^{125}I radiolabeled Au@Ag nanoseeds were physically mixed with porphyrins, which makes it difficult to distinguish whether the observed enhancement mainly originated from the contribution of Auger electrons or from photoelectron-induced processes, as the former would play only a minor role in such a mixed system.

In our experiments, smaller AuNPs (1.7 nm and 10 nm) were used, where the energy deposition behavior differs from that of larger particles. Smaller AuNPs release a greater fraction of Auger electrons into the surrounding medium[46], which should make the spatial proximity of Ce6 to the AuNPs surface more important if direct electron excitation was the dominant pathway. However, when Ce6 was freely dispersed and not bound to AuNPs surface, ^{125}I radiolabeled AuNPs produced a strong cytotoxic effect. In contrast, attaching Ce6 to the surface of ^{125}I radiolabeled 10 nm AuNPs, did not yield any synergistic response, even though the conjugated form showed higher cellular uptake than free Ce6 (Fig. 3.5). Sung et al.[47] simulated the dose distribution around AuNPs using the Auger electron spectrum of ^{125}I and found that the low-energy electrons emitted from AuNPs produce a dose enhancement confined within ~ 30 nm from the particle surface for 10 and 50 nm AuNPs, while this effect is minimal for 2 nm particles. According to these simulations, if direct excitation were dominant, conjugating Ce6 to 10 nm AuNPs should enhance the therapeutic effect under our normoxic conditions, where oxygen is not expected to be limiting. However, no synergistic response was observed. Therefore, direct electron excitation is unlikely to be the dominant pathway.

However, placing Ce6 in a region with high local electron density may also increase ionization of Ce6. This leads to the second hypothesis, in which ionized Ce6 participates in electron transfer reactions with water radiolysis products, with $\cdot O_2^-$ as a likely intermediate toward $^1O_2$ (Chapter 2). Importantly, increased ionization alone may not lead to a stronger effect, because this pathway also requires sufficient, diffusible radiolysis products. When Ce6 is positioned very close to the AuNPs surface, local $\cdot O_2^-$ quenching may happen. AuNPs have been reported to scavenge $\cdot O_2^-$ at their surface through superoxide dismutase-like activity, which could

potentially reduce the availability of $\cdot O_2^-$ needed for $^1O_2$ formation.[48-50] By contrast, if Ce6 molecules are more freely dispersed around ^{125}I radiolabeled AuNPs, radiolysis products generated in the surrounding medium may have a greater chance to react with ionized Ce6. This possibility is supported by reports showing that under ionizing radiation exposure, AuNPs can generate more ROS, primarily ·OH and $\cdot O_2^-$ in aqueous solutions[51]. Nevertheless $^1O_2$ formation was not directly measured in the AuNP containing system in this chapter and should be verified in future work, together with more detailed analysis of nanoscale energy deposition and subsequent radical formation pathways.

Our results also indicate that radiolabeling AuNPs with ^{125}I is necessary to achieve stronger cell killing with Ce6 than with ^{125}I alone. This may reflect changes in both radiation interaction behavior and intracellular transport efficiency.[52] Such labeling could enhance the local energy deposition within cells compared to free ^{125}I, whereas unlabeled AuNPs likely provide limited dose enhancement because of the low AuNPs concentrations compared to water, causing most radiation energy to be absorbed by water instead of the nanoparticles.

Another factor that has not been considered here is that high-LET Auger electrons emitted during ^{125}I decay may damage Ce6 and compromise its photosensitizing capability. This hypothesis could be tested by exposing ^{125}I radiolabeled Ce6-Au to light and measuring singlet oxygen generation to assess whether Ce6 retains its photosensitizing activity. In addition, scavenger experiments could be used to evaluate whether $^1O_2$ and $\cdot O_2^-$ play an important role in the observed therapeutic effects.

3.4 Conclusion

In this work, we examined the activation of Ce6 under ^{125}I irradiation and how the spatial arrangement between the energy deposition region and Ce6 influences its activation and biological effects. Ce6 produced $^1O_2$ and induced cytotoxicity under ^{125}I exposure in a dose-dependent manner. When ^{125}I was radiolabeled onto AuNPs, the combination with free Ce6 resulted in pronounced cell-killing effects. In contrast, confining Ce6 close to the AuNP surface within the range of Auger electrons emission did not produce a therapeutic effect. These results indicate that direct energy deposition or electron-driven excitation of Ce6 is unlikely to be the dominant pathway, whereas Ce6 ionization followed by reactions with water radiolysis products is more likely to be involved. Our findings suggest that complex nanoparticle-photosensitizer conjugation is not required to achieve therapeutic effects in this system. This

practical advantage may benefit future development and translation of radiodynamic therapy to the clinic. However, further studies are required to investigate the underlying activation mechanisms and optimize system design.

References

1 Baskar, R., Lee, K. A., Yeo, R. & Yeoh, K.-W. Cancer and Radiation Therapy: Current Advances and Future Directions. *International Journal of Medical Sciences* **9**, 193-199 (2012).

2 Zafar, A., Khatoon, S., Khan, M. J., Abu, J. *et al.* Advancements and limitations in traditional anti-cancer therapies: a comprehensive review of surgery, chemotherapy, radiation therapy, and hormonal therapy. *Discover Oncology* **16**, 607 (2025).

3 Abshire, D. & Lang, M. K. The Evolution of Radiation Therapy in Treating Cancer. *Seminars in Oncology Nursing* **34**, 151-157 (2018).

4 Dougherty, T. J., Gomer, C. J., Henderson, B. W., Jori, G. *et al.* Photodynamic Therapy. *JNCI: Journal of the National Cancer Institute* **90**, 889-905 (1998).

5 Agostinis, P., Berg, K., Cengel, K. A., Foster, T. H. *et al.* Photodynamic therapy of cancer: An update. *CA: A Cancer Journal for Clinicians* **61**, 250-281 (2011).

6 Chong, L. M., Tng, D. J. H., Tan, L. L. Y., Chua, M. L. K. & Zhang, Y. Recent advances in radiation therapy and photodynamic therapy. *Applied Physics Reviews* **8**, 041322 (2021).

7 Zhu, S., Lin, S., Han, R., Zhu, S. *et al.* Treating Deep-Seated Tumors with Radiodynamic Therapy: Progress and Perspectives. *Pharmaceutics* **16**, 1135 (2024).

8 He, L., Yu, X. & Li, W. Recent Progress and Trends in X-ray-Induced Photodynamic Therapy with Low Radiation Doses. *ACS Nano* **16**, 19691–19721 (2022).

9 Takahashi, J. & Misawa, M. Characterization of reactive oxygen species generated by protoporphyrin IX under X-ray irradiation. *Radiation Physics and Chemistry* **78**, 889-898 (2009).

10 Tu, Z., Sang, Z., Xu, Y., Liang, W. *et al.* Porphyrin-Engineered ^{125}I-Nanoseeds as a Prototype for Immunogenic Brachytherapy. *Journal of the American Chemical Society* **147**, 13229–13242 (2025).

11 Duan, D., Liu, H., Xu, Y., Han, Y. *et al.* Activating TiO_2 Nanoparticles: Gallium-68 Serves as a High-Yield Photon Emitter for Cerenkov-Induced Photodynamic Therapy. *ACS Applied Materials & Interfaces* **10**, 5278–5286 (2018).

12 Lioret, V., Bellaye, P.-S., Bernhard, Y., Moreau, M. *et al.* Cherenkov Radiation induced photodynamic therapy - repurposing older photosensitizers, and radionuclides. *Photodiagnosis and Photodynamic Therapy* **44**, 103816 (2023).

13 Li, J., Lv, Z., Guo, Y., Fang, J. *et al.* Hafnium (Hf)-Chelating Porphyrin-Decorated Gold Nanosensitizers for Enhanced Radio–Radiodynamic Therapy of Colon Carcinoma. *ACS Nano* **17**, 25147–25156 (2023).

14 Lechtman, E., Chattopadhyay, N., Cai, Z., Mashouf, S. *et al.* Implications on clinical scenario of gold nanoparticle radiosensitization in regards to photon energy, nanoparticle size, concentration and location. *Physics in Medicine and Biology* **56**, 4631-4647 (2011).

15 Liu, H., Xu, B., Chen, L., Li, X. *et al.* Preparation and Characterization of Chlorin e6-Conjugated Au Nanoparticles as the Radiosensitizer for Enhanced Radiotherapy. *ACS Omega* (2025).

16 Robertson, D. M., Fountain, K. S., Anderson, J. A. & Posthumus, G. W. Radioactive iodine-125 as a therapeutic radiation source for management of intraocular tumors. *Transactions of the American Ophthalmological Society* **79**, 294-306 (1981).

17 Buchegger, F., Perillo-Adamer, F., Dupertuis, Y. M. & Bischof Delaloye, A. Auger radiation targeted into DNA: a therapy perspective. *European journal of nuclear medicine and molecular imaging* **33**, 1352-1363 (2006).

18 Wang, R., Liu, H., Antal, B., Wolterbeek, H. T. & Denkova, A. G. Ultrasmall Gold Nanoparticles Radiolabeled with Iodine-125 as Potential New Radiopharmaceutical. *ACS Applied Bio Materials* **7**, 1240-1249 (2024).

19 Walsh, A. A. Chemisorption of iodine-125 to gold nanoparticles allows for real-time quantitation and potential use in nanomedicine. *Journal of Nanoparticle Research* **19**, 152 (2017).

20 Chen, Y., Yang, J., Fu, S. & Wu, J. Gold Nanoparticles as Radiosensitizers in Cancer Radiotherapy. *International Journal of Nanomedicine* **15**, 9407-9430 (2020).

21 Clement, S., Chen, W., Anwer, A. G. & Goldys, E. M. Verteprofin conjugated to gold nanoparticles for fluorescent cellular bioimaging and X-ray mediated photodynamic therapy. *Microchimica Acta* **184**, 1765-1771 (2017).

22 Tiwari, P. M., Vig, K., Dennis, V. A., Singh, S. R. *et al.* Functionalized Gold Nanoparticles and Their Biomedical Applications. *Nanomaterials* **1**, 31-63 (2011).

23 Vieira, L., Castilho, M. L., Ferreira, I., Ferreira-Strixino, J. *et al.* Synthesis and characterization of gold nanostructured Chorin e6 for Photodynamic Therapy. *Photodiagnosis and Photodynamic Therapy* **18**, 6-11 (2017).

24 Kamkaew, A., Cheng, L., Goel, S., Valdovinos, H. F. *et al.* Cerenkov Radiation Induced Photodynamic Therapy Using Chlorin e6-Loaded Hollow Mesoporous Silica Nanoparticles. *ACS Applied Materials & Interfaces* **8**, 26630-26637 (2016).

25 Jo, C., Ahn, H., Kim, J. H., Lee, Y. J. *et al.* Cancer therapy by antibody-targeted Cerenkov light and metabolism-selective photosensitization. *Journal of Controlled Release* **352**, 25-34 (2022).

26 Probes, M. *Singlet Oxygen Sensor Green Reagent*, 2004).

27 Mojzisova, H., Bonneau, S., Vever-Bizet, C. & Brault, D. Cellular uptake and subcellular distribution of chlorin e6 as functions of pH and interactions with membranes and lipoproteins. *Biochim Biophys Acta* **1768**, 2748-2756 (2007).

28 Calabrese, E. J. Hormesis and medicine. *British Journal of Clinical Pharmacology* **66**, 594-617 (2008).

29 Alotiby, M., Greguric, I., Kibédi, T., Tee, B. & Vos, M. Quantitative electron spectroscopy of ^{125}I over an extended energy range. *Journal of Electron Spectroscopy and Related Phenomena* **232**, 73-82 (2019).

30 Howell, R. W. Radiation spectra for Auger-electron emitting radionuclides: Report No. 2 of AAPM Nuclear Medicine Task Group No. 6. *Medical Physics* **19**, 1371-1383 (1992).

31 Ku, A., Facca, V. J., Cai, Z., Reilly, R. M. *et al.* Auger electrons for cancer therapy – a review. *EJNMMI Radiopharmacy and Chemistry* **4**, 27 (2019).

32 Hingorani, M., Spitzweg, C., Vassaux, G., Newbold, K. *et al.* The Biology of the Sodium Iodide Symporter and its Potential for Targeted Gene Delivery. *Current Cancer Drug Targets* **10**, 242-267 (2010).

33 Tang, J., Wang, X., Xu, Y., Shi, Y. *et al.* Sodium-iodine Symporter Gene Expression Controlled by the EGR-1 Promoter. *Technology in Cancer Research & Treatment* **14**, 61-69 (2015).

34 Yun, X., Tang, M., Yang, Z., Wilksch, J. J. *et al.* Interrogation of drug effects on HeLa cells by exploiting new AFM mechanical biomarkers. *RSC Advances* **7**, 43764-43771 (2017).

35 Uzhytchak, M., Smolková, B., Frtús, A., Stupakov, A. *et al.* Sensitivity of endogenous autofluorescence in HeLa cells to the application of external magnetic fields. *Scientific Reports* **13**, 10818 (2023).

36 Borle, A. B. Kinetic analyses of calcium movements in HeLa cell cultures. I. Calcium influx. *The Journal of general physiology* **53**, 43-56 (1969).

37 Adjei, D., Trinh, N. D. & Mostafavi, M. Application of Geant4-DNA for simulating water radiolysis induced by Auger electron-emitting radionuclides. *Journal of Radiation Research* **64**, 369-378 (2023).

38 Fuss, M. C., Muñoz, A., Oller, J. C., Blanco, F. *et al.* Energy deposition model for I-125 photon radiation in water. *The European Physical Journal D* **60**, 203-208 (2010).

39 Shen, H., Huang, H. & Jiang, Z. Nanoparticle-based radiosensitization strategies for improving radiation therapy. *Frontiers in Pharmacology* **14**, 1145551 (2023).

40 Kwatra, D., Venugopal, A. & Anant, S. Nanoparticles in radiation therapy: a summary of various approaches to enhance radiosensitization in cancer. *Translational Cancer Research* **2** (2013).

41 Mesbahi, A. A review on gold nanoparticles radiosensitization effect in radiation therapy of cancer. *Reports of Practical Oncology and Radiotherapy* **15**, 176-180 (2010).

42 Cho, S., Jones, B. & Krishnan, S. The dosimetric feasibility of gold nanoparticle-aided radiation therapy (GNRT) via brachytherapy using low-energy gamma-/X-ray sources. *Physics in Medicine and Biology* **54**, 4889-4905 (2009).

43 Liu, J., Yu, M., Ning, X., Zhou, C. *et al.* PEGylation and zwitterionization: Pros and cons in the renal clearance and tumor targeting of near-IR-emitting gold nanoparticles. *Angewandte Chemie - International Edition* **52**, 12572-12576 (2013).

44 Omping, J., Unabia, R., Reazo, R. L., Lapening, M. *et al.* Facile Synthesis of PEGylated Gold Nanoparticles for Enhanced Colorimetric Detection of Histamine. *ACS Omega* **9**, 14269–14278 (2024).

45 Huang, X., Huang, X., Tian, X.-J., Tian, X.-J. *et al.* The conjugates of gold nanorods and chlorin e6 for enhancing the fluorescence detection and photodynamic therapy of cancers. *Physical Chemistry Chemical Physics* **15**, 15727-15733 (2013).

46 Chow, J. C. L. *Chapter 2 - Photon and electron interactions with gold nanoparticles: A Monte Carlo study on gold nanoparticle-enhanced radiotherapy*. (William Andrew Publishing, 2016).

47 Wonmo Sung, Seongmoon Jung & Ye, S.-J. Evaluation of the microscopic dose enhancement for nanoparticle-enhanced Auger therapy. *Physics in medicine and biology* **61**, 7522-7535 (2016).

48 Cheng, N. N., Starkewolf, Z., Davidson, R. A., Sharmah, A. *et al.* Chemical Enhancement by Nanomaterials under X-ray Irradiation. **134**, 1950–1953 (2012).

49 Matsuoka, K., Nakatani, Y., Yoshimura, T. & Akasaki, T. Superoxide Scavenging Activity of Gold, Silver, and Platinum Nanoparticles Capped with Sugar-based Nonionic Surfactants. *Journal of Oleo Science* **68**, 847-854 (2019).

50 Shcherbakov, V., Denisov, S. A. & Mostafavi, M. A mechanistic study of gold nanoparticles catalysis of O_2 reduction by ascorbate and hydroethidine, investigating reactive oxygen species reactivity. *RSC Advances* **13**, 8557-8563 (2023).

51 Misawa, M. & Takahashi, J. Generation of reactive oxygen species induced by gold nanoparticles under X-ray and UV Irradiations. *Nanomedicine: Nanotechnology, Biology and Medicine* **7**, 604-614 (2011).

52 Bardane, A., Maalej, N., Chakir, E. M. & Ibrahmi, E. M. A. Gold nanoparticle effect on dose and DNA damage enhancement in the vicinity of gold nanoparticles. *Nuclear Analysis* **3**, 100126 (2024).

Supporting information

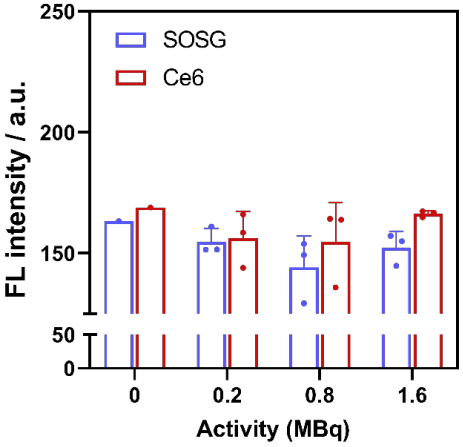

Figure S3.1. The fluorescence intensity of SOSG after addition of [^{125}I]NaI at 0 h. n = 3.

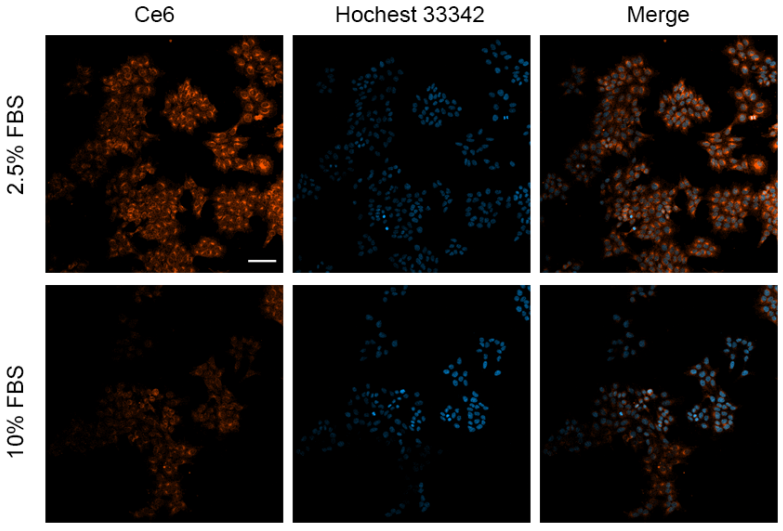

Figure S3.2. Cellular uptake of Ce6 in HeLa cells in DMEM containing 2.5 % FBS or 10 % FBS. Excitation: 405 nm, scale bar = 100 µm.

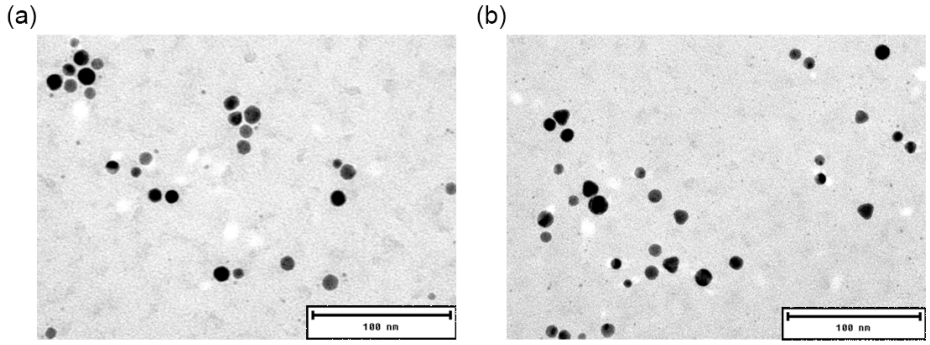

Figure S3.3. TEM images of (a) BSA-Au and (b) Ce6-Au. Scale bar = 100 nm.

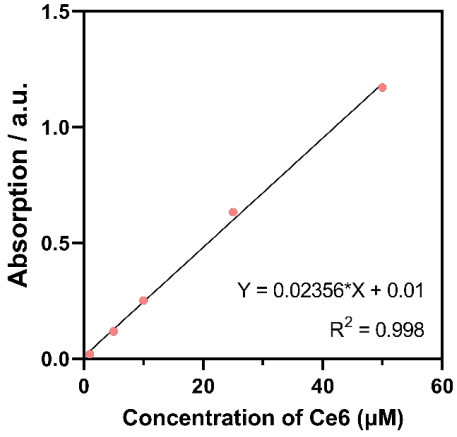

Figure S3.4. The absoprtion of Ce6 as function of concentration. The line is a linear fit of the data.

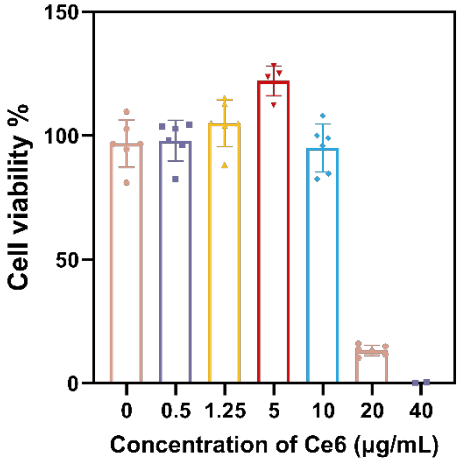

Figure S3.5. Cell viability test of various concentrations of Ce6 in HeLa cells in 2.5% FBS DMEM. n = 6.

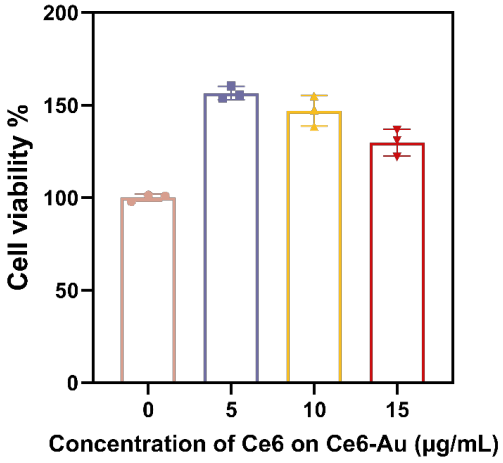

Figure S3.6. Cell viability test of Ce6-Au in HeLa cells as a function of Ce6 concentrations. Au concentration from left to right was 13, 26 and 52 μg/mL, respectively. n = 3.

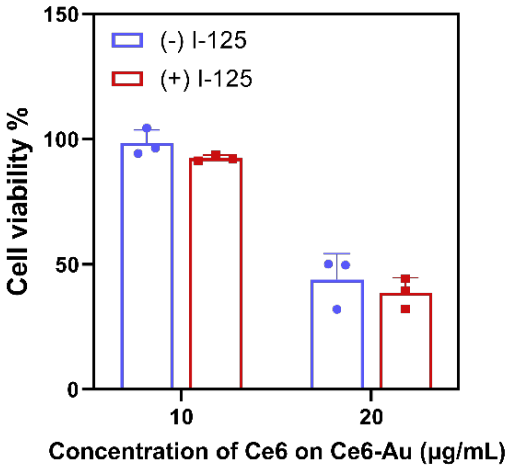

Figure S3.7. Cell viability test of Ce6-Au in the presence of 0.8 MBq [^{125}I]NaI. Au concentration from left to right was 40 and 80 µg/mL, respectively. n = 3.

Chapter 4

In Vitro Characterization of the Radiosensitizing Effects of 5-Aminolevulinic Acid as a Function of Dose Rate

Abstract

5-Aminolevulinic acid (5-ALA) has shown great promise as a radiosensitizer in conventional external beam radiotherapy (EBRT) by promoting the intracellular accumulation of protoporphyrin IX (PpIX), which enhances reactive oxygen species (ROS) generation in tumor cells. In contrast, its combination with brachytherapy has received limited attention. A key difference between EBRT and brachytherapy is the markedly lower dose rate used in the latter, which may alter the cellular oxidative environment and influence how PpIX contributes to radiosensitization. In this study, we examined how dose rate affects the radiosensitizing response of 5-ALA-induced PpIX in glioblastoma U87 and prostate cancer PIP-PC3 cells. X-ray irradiation at 1.5 Gy/min was used to mimic the dose rate of conventional EBRT, while yttrium-90 foil was employed as an external source to deliver continuous low-dose-rate irradiation (< 2 Gy/h). At 1.5 Gy/min, 5-ALA induced a clear radiosensitizing effect in both cell lines, resulting in reduced cell proliferation. As the dose rate decreased, this effect was still detectable at 2 Gy/h, but progressively weakened and ultimately disappeared under continuous ^{90}Y irradiation. These findings indicate that the radiosensitizing behavior of 5-ALA is dose-rate dependent which needs to be taken into account when evaluating the potential use of 5-ALA in radiotherapy modalities beyond EBRT.

Keywords: 5-aminolevulinic acid, dose rate, brachytherapy, yttrium-90

4.1 Introduction

The therapeutic effect of radiotherapy (RT) primarily relies on the ability of ionizing radiation to induce cancer cell death through either direct or indirect DNA damage, the latter being mediated by aqueous electrons (e_{aq}^-) and reactive oxygen species (ROS) generated in water.[1-4] Approximately 60% of the induced damage on vital cellular components is caused by ROS under low linear energy transfer (LET) irradiation, such as X-ray and gamma ray photons.[2,5] To enhance this effect without increasing harm to surrounding healthy tissue, radiosensitizers that amplify ROS production have been explored.[6] Among these, photosensitizers (PSs), particularly porphyrins[7], are considered promising candidates due to their low systemic toxicity and ability to generate toxic ROS upon exposure to ionizing radiation.[8] This radiosensitizing effect has been mainly demonstrated in conventional external beam radiation therapy (EBRT), which typically delivers dose rate of 1-2 Gy per minute.[9-13] Combinations with other radiotherapy types, such as low-dose-rate (LDR) brachytherapy and radionuclide therapy which typically have much lower dose rates of less than 2 Gy/h, have received little attention so far.[14]

5-Aminolevulinic acid (5-ALA), a natural precursor of protoporphyrin IX (PpIX) in the mitochondrial heme biosynthesis pathway, is one of the most recently studied PSs in clinical settings.[15] Because of the metabolic alterations associated with Warburg effect, tumors tend to accumulate higher levels of PpIX than normal tissues.[16] Given its safety profile and high selectivity for tumor tissue over healthy tissue, 5-ALA was approved by the U.S. Food and Drug Administration (FDA) for fluorescence-guided surgery (FGS) in patients with suspected high-grade gliomas (HGGs).[17] Beyond imaging applications, 5-ALA has also been investigated as a radiosensitizer in patients with recurrent glioblastoma undergoing EBRT.[18,19] In addition to EBRT, brachytherapy has attracted growing interest in treating glioblastoma.[20-22] However, the use of 5-ALA in brachytherapy has been limited. In a recent case report, 5-ALA-guided resection was combined with cesium-131 (^{131}Cs) brachytherapy in a pediatric patient with recurrent high-grade glioma.[23] Although the clinical outcomes were positive, the potential radiosensitizing contribution of 5-ALA to ^{131}Cs brachytherapy, particularly in response to the lower dose rate of ^{131}Cs compared to EBRT, was not assessed. Brachytherapy is also commonly used in the treatment of prostate cancer, where LDR isotopes such as iodine-125 and iridium-192 are frequently employed.[24] In this context, 5-ALA has also been tested in patients in combination with LDR brachytherapy using ^{125}I seeds, yet no significant tumor regression was observed.[25]

The radiosensitizing efficacy of PSs such as PpIX has been suggested to proceed via radical-radical reactions between PS-derived intermediates and water radiolysis products, resulting in the formation of ROS including superoxide ($\cdot O_2^-$), hydroxyl radicals ($\cdot OH$) and hydrogen peroxide (H_2O_2).[26] Results in Chapter 2 suggest that the activation of PSs has a dose-rate dependent manner, with the highest singlet oxygen ($^1O_2$) production by the photosensitizer Chlorin e6 observed at the lowest dose rate (0.005 Gy/min) when tested in pure water. However, the situation is more complex in biological systems, where a complete antioxidant defense network is present.[27] In such environments, dose rate not only influences radical kinetics, but also modulates tumor cell responses such as DNA repair capacity and antioxidant enzyme expression.[28,29] Enzymes may attenuate the oxidative damage induced by PSs exposed to lower dose rates since that typically requires longer irradiation times providing more time for the cell to adapt.

To evaluate the dose rate effect in biological systems, we investigated the combination of 5-ALA and ionizing radiation in two cancer cell lines, glioblastoma U87 and prostate cancer PIP-PC3, using two-dimensional *in vitro* models. To simulate different clinical dose rates, we applied 1.5 Gy/min X-rays to mimic EBRT conditions and used neutron-activated yttrium-90 foil as a continuous beta-minus radiation source delivering dose rates below 2 Gy/h.

4.2 Materials and Method

Cell culture

Glioblastoma cell lines U87 and prostate cell lines PIP-PC3 with stable PSMA expression were used in the experiments. U87 cells were purchased from ATCC. PIP-PC3 cells were kindly provided by Erasmus MC. U87 cells were cultured in DMEM (VWR chemicals), supplemented with 10% fetal bovine serum (Biowest) and 1X penicillin-streptomycin solution (VWR chemicals). PIP-PC3 cells were cultured in RPMI 1640 with L-glutamine (VWR chemicals), supplemented with 10% fetal bovine serum (Biowest) and 1X penicillin-streptomycin solution (VWR chemicals). All cells were incubated with a humidified atmosphere containing 5% CO_2 at 37 ºC.

Radiation source and dosimetry

Photon irradiation. High-energy photons were generated using an X-ray source (Philips MCN 321) equipped with a variable-energy X-ray tube. Irradiation was performed at 250 kV with a 1 mm Cu/Al filter, and the tube current was adjusted to deliver dose rates of 1.5 Gy/min.

Beta minus irradiation. Beta minus radiation was generated by an yttrium-90 ([^{90}Y]Y) foil. To produce radioactive ^{90}Y, an ^{89}Y foil (50 mm×50 mm, 0.127 mm thick,1.39 g, 99.9%, Thermo Fisher scientific) was enclosed in a double-layered polyethylene (PE) film and sealed on all four sides using a heat sealer to ensure complete encapsulation. The sealed package was then rolled and placed into a PE-rabbit capsule for irradiation. Neutron activation was performed for 45 minutes at the BP3 pneumatic irradiation facility (neutron fluxes: $\Phi_{th} = 4.57 \times 10^{16}$ m^{-2} s^{-1}; Φepi = 9.5×10^{14} m^{-2} s^{-1}; $\Phi_{fast} = 3.36 \times 10^{15}$ m^{-2} s^{-1}) of the Hoger Onderwijs Reactor (HOR), Reactor Institute Delft. Following irradiation, the foil was cooled for 4 days to allow the decay of ^{90m}Y and avoid unwanted gamma-rays. After unpacking, the activated [^{90}Y]Y foil was transferred to a closed Perspex container for further use (Scheme 4.1).

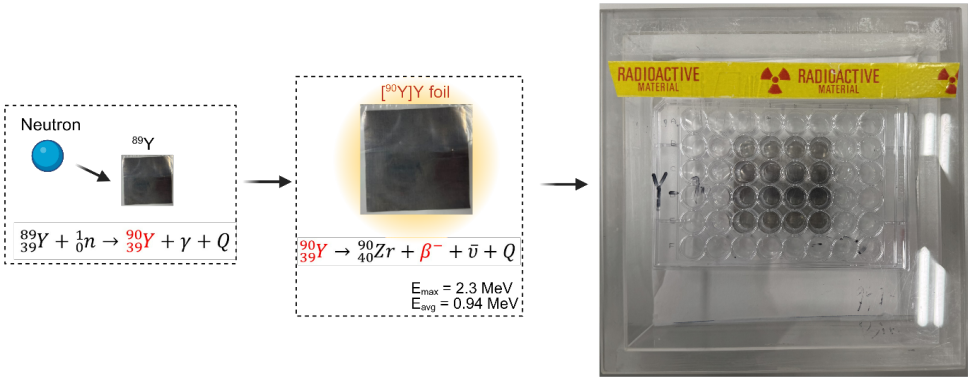

Scheme 4.1. Production of the [^{90}Y]Y foil by neutron activation and the corresponding setup used for the irradiation experiments.

Dose rate determination. Dose rates were determined based on measurements of GAFchromic™ EBT3 films. For X-ray measurements, a strip of EBT3 film was placed either in a 48-well plate or in a 1.5 mL Eppendorf vial containing 1 mL of Milli-Q water and irradiated under experimental conditions. For the beta minus irradiation the film was cut to fit the wells of a 48-well plate. The activated [^{90}Y]Y foil (5 × 5 cm) was placed under the plate, covering 3 × 3 wells. Accordingly, EBT3 films were placed in these 9 wells, which were fully covered by the foil. A thin tissue was inserted between the foil and the plate to prevent contamination, and the setup was irradiated for 1 hour. After exposure, the films were scanned using a flatbed scanner (EPSON V700), and the resulting images were analyzed with ImageJ. Pixel values were then converted to dose using a calibration curve.

In vitro accumulation of 5-ALA-induced PpIX

A stock solution of 100 mM 5-aminolevulinic acid hydrochloride (Thermo Fisher Scientific) was prepared in Milli-Q water, protected from light with aluminum foil and stored at -20 ºC. Cells were seeded at a density of 4×10^4 cells per well in 8-well chambered coverslips (Ibidi) overnight. Working solutions of 1 mM 5-ALA were freshly prepared by diluting the stock solution in complete culture medium.

To assess the accumulation of PpIX in response to different 5-ALA concentrations, cells were treated with 1 mM, 2.5 mM, 5 mM, or 10 mM 5-ALA for 24 hours. After incubation, 5-ALA was removed, and cells were washed twice with PBS. Cells were then fixed in 4% paraformaldehyde in PBS (Thermo Fisher Scientific) for 15 minutes at room temperature in the dark. Following fixation, cells were washed three times with PBS (5 minutes per wash) and stored at 4 °C, protected from light, until imaging.

To examine PpIX accumulation over time, 200 µL of 1 mM 5-ALA solution was added to each sample. Coverslips were wrapped in aluminum foil to protect from light during incubation. Cells were incubated with 5-ALA for 2, 4, or 18 hours. At each time point, the medium was removed and cells were washed twice with PBS. PpIX fluorescence was visualized using a confocal microscope (LSM 980, ZEISS) with an excitation wavelength of 405 nm and emission detected at 620 nm.

Cell proliferation assay

The cell counting kit-8 (CCK-8) assay. To evaluate the cytotoxicity of 5-ALA, U87 and PIP-PC3 cells were seeded at a density of 6,000 cells per well in 96-well plates. After cell attachment, different concentrations of 5-ALA (1 mM, 2.5 mM, 5 mM, and 10 mM) were added to the wells. The cells were incubated with 5-ALA for 24 hours. Following the incubation period, cell viability was assessed. To evaluate the radiosensitizing effect of 5-ALA, only X-ray irradiation was applied. Cells were seeded at a density of 5×10^5 per well in 6-well plates (Sarstedt) and incubated overnight. The following day, 2 mL of freshly prepared 1 mM 5-ALA solution was added into cells, with the control group receiving medium only. Plates were covered with aluminum foil to prevent light and incubated for 4 hours at 37°C in a humidified atmosphere containing 5% CO_2. After treatment, cells were washed twice with PBS, harvested using 0.25% trypsin-EDTA (Biowest). 5-ALA-treated cells were collected in black light-safe Eppendorf tubes to prevent light-activation. Cell suspensions were then adjusted to 1×10^5 cells/mL before X-ray irradiation. X-ray irradiation was performed at a dose rate of 1.5 Gy/min (250 kV, 15 mA, 1 mm Cu filter) with cells placed on a horizontal platform at 26 cm distance.

All irradiated cells received a total dose of 4 Gy. After irradiation, cells were immediately seeded in 96-well plates at 2000 cells per well (100 µL/well) in complete medium. Four experimental groups were set for each cell line: untreated control, 5-ALA treatment only, 5 Gy irradiation only, and 5-ALA combined with 5 Gy irradiation. Cell viability was assessed at 24, 48, 72 and 96 hours post-treatment using the CCK-8 assay according to the manufacturer's instructions.

5-Ethynyl-2'-deoxyuridine (EdU) proliferation assay. EdU staining was performed using ClickTech EdU Cell Proliferation Kit 555 (Baseclick) according to manufacturer's protocol. Briefly, following treatment with 5-ALA and X-ray irradiation, cells were seeded at a density of 1×10^4 cells per well in 8-well chambered coverslips (Ibidi) and incubated for 48 h. After incubation, 10 µM 5-EdU was added and incubated with cells for 1 h, followed by fixation and permeablization. Cells were then stained with 5-TAMRA-PEG3-Azid (λ_{abs} = 546 nm and λ_{em} = 579 nm) and Hoechst 33342. Fluorescence imaging was performed using a confocal microscope (LSM 980, ZEISS).

Clonogenic assay. X-ray irradiation: for the clonogenic assay, cells were seeded and treated with 5-ALA under the same conditions as described in the CCK-8 Assay. X-ray irradiation was performed using dose rates of 1.5 Gy/min. U87 cells were irradiated with doses of 2, 4, and 6 Gy, while PIP-PC3 cells received 1, 2, and 3 Gy. Following irradiation, cells were seeded in 6-well plates at appropriate densities in six replicates (U87: 600, 800, and 1600 cells/well for 2, 4, and 6 Gy, respectively; PIP-PC3: 200, 400, and 600 cells/well for 1, 2, and 3 Gy, respectively). Control groups included cells with or without 5-ALA and/or irradiation (U87: 600 cells/well; PIP-PC3: 200 cells/well). After 7 to 10 days (PIP-PC3) or 10 to 14 days (U87) of incubation, colonies were washed with PBS, fixed in 4% paraformaldehyde, and stained with 1% crystal violet solution. Colonies containing more than 50 cells were manually counted and survival fractions were normalized to the untreated control group.

Yttrium-90 irradiation: approximately 1×10^5 per well U87 or PIP-PC3 cells were seeded in a 48-well plate and incubated overnight. The following day, 500 µL of 1 mM 5-ALA was added into cells. After 4 hours of incubation, the 5-ALA-containing medium was discarded, cells were washed twice with PBS, and 500 µL of fresh culture medium was added. The plate with cells in wells was then placed on top of the foil to receive defined dosed (1 Gy or 3 Gy) using various dose rates. After irradiation, cells were trypsinized and reseeded into 6-well plates (U87: 600, 800 cells/well for 1 and 3 or 4 Gy, respectively; PIP-PC3: 200 and 600 cells/well for 1 and 3 Gy, 800 cells/well for 400 Gy, respectively). After 7 to 10 days (PIP-PC3) or 10 to 14 days

(U87) of incubation, colonies were washed with PBS, fixed in 4% paraformaldehyde, and stained with 1% crystal violet solution. Colonies containing more than 50 cells were manually counted and survival fractions were normalized to the untreated control group.

Statistical analysis

Data with error bar were presented as mean ± SD. Statistical analyses were performed using paired t-test, one-way or two-way ANOVA as appropriate. GraphPad Prism software (version 8.00) was used for statistical analysis and data visualization. $P < 0.05$ was considered statistically significant.

4.3 Results

Intracellular accumulation of PpIX

Although tumors tend to accumulate higher levels of PpIX than normal tissues, intracellular PpIX levels are still subject to cellular regulation and clearance mechanisms. To determine an optimal 5-ALA concentration for subsequent experiments, we evaluated both PpIX accumulation efficiency and cytotoxicity across a range of 5-ALA concentrations in U87 and PIP-PC3 cells. After 24 h incubation, PpIX fluorescence was detectable at [5-ALA] = 1 mM in both cell lines (Fig. S4.1). In U87 cells, increasing the concentration beyond 1 mM did not lead to a noticeable increase in fluorescence signal. In contrast, PIP-PC3 cells showed the highest fluorescence at 2.5 mM, while 5 and 10 mM exhibited reduced fluorescence (Fig. S4.1). However, cell viability assays revealed significant cytotoxicity at 2.5 mM in PIP-PC3 cells (Fig. S4.2). Therefore, to balance PpIX accumulation with cell viability and maintain consistent conditions between both cell lines, 1 mM 5-ALA was selected for all subsequent experiments. To further determine the optimal timing for irradiation, we next investigated the time-dependent accumulation of PpIX in U87 (Fig. 4.1(a)) and PIP-PC3 cells (Fig. 4.1(b)). In U87 cells (Fig. 4.1(c)), fluorescence was observed at 2 h and slightly increased at 4 h ($p < 0.05$), followed by a decrease at 18 h ($p < 0.01$ vs. 4 h). A similar trend was observed in PIP-PC3 cells, where fluorescence was also detectable at 2 h, followed by an increase at 4 h ($p < 0.05$). Unlike U87 cells, the fluorescence in PIP-PC3 cells remained stable at 18 h, showing no reduced fluorescence intensity compared to the 4 h time point (Fig. 4.1(d)). As the fluorescence intensity of PpIX reached its maximum at 4 h, all subsequent irradiations were conducted at 4 h following 5-ALA treatment.

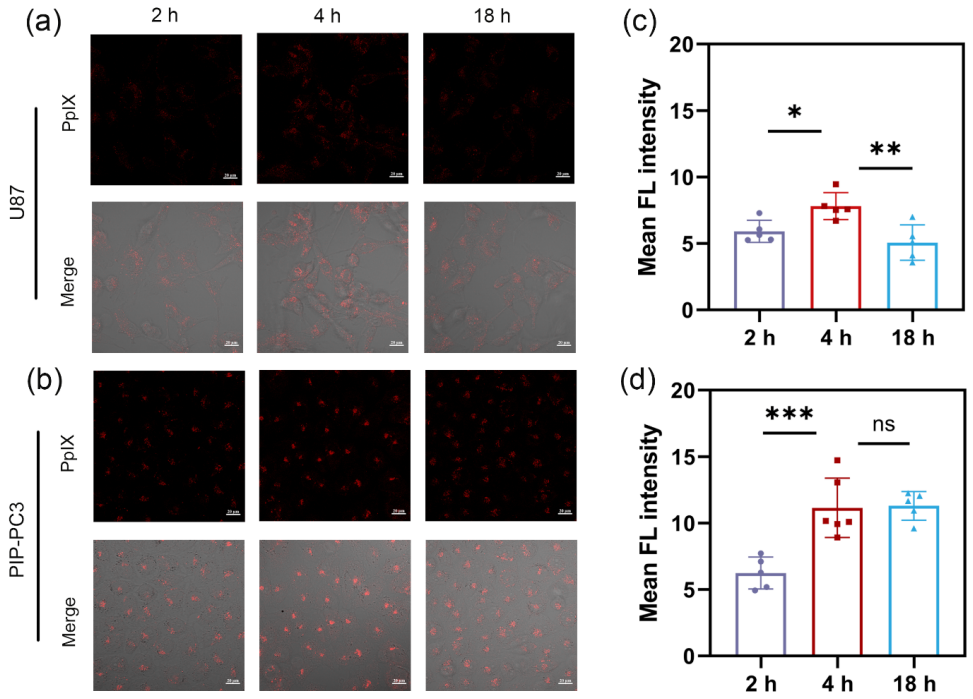

Figure 4.1. Accumulation of 5-ALA-induced PpIX in U87 and PIP-PC3 cells over time. (a) Fluorescence images and the corresponding merged brightfield–fluorescence images of U87 cells after 2 h, 4 h, and 18 h incubation with 1 mM 5-ALA. (b) Fluorescence images and the corresponding merged brightfield-fluorescence images of PIP-PC3 cells under the same conditions. Mean fluorescence intensity of PpIX in (c) U87 cells and (d) PIP-PC3 cells. Scale bar = 20 µm. All data are represented as mean ± SD and analyzed by one-way ANOVA; *p < 0.05, **p < 0.01, ***p < 0.001; n = 6.

Cell proliferation following combined 5-ALA and X-ray treatment

After determining the optimal time point for PpIX accumulation in U87 and PIP-PC3 cells, we next evaluated the biological effects of 5-ALA in combination with ionizing radiation. As 5-ALA has already been applied in combination with EBRT in both clinical and preclinical research, we examined its radiosensitizing effect under X-ray irradiation at a dose rate of 1.5 Gy/min, using CCK-8, clonogenic survival, and 5-EdU proliferation assays. We first assessed cell proliferation using the CCK-8 assay. As shown in Figure 4.2(a), the viability of U87 cells treated with 4 Gy decreased when compared to the control, showing even further reduction at 96 h. The addition of 5-ALA on the other hand did not lead to any further decrease compared to radiation alone. In PIP-PC3 cells, a slight reduction in viability was noted in the 4 Gy group at 48 hours, followed by a pronounced decrease at 72 and 96 hours compared to the control groups. The addition of 5-ALA did not cause any further reduction in viability relative to

radiation alone at any time point (Fig. 4.2(b)).

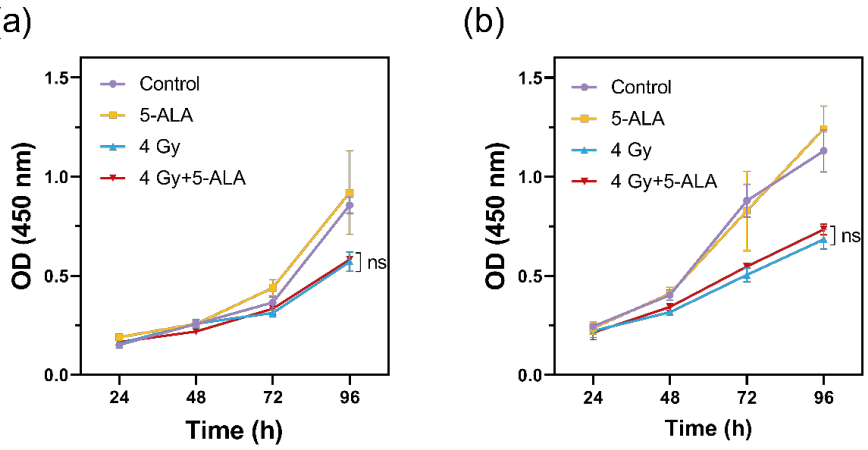

Figure 4.2. Cell viability of 1 mM 5-ALA pretreatment combined with 4 Gy X-ray irradiation after 24, 48, 72 and 96 h of incubation. (a) Cell viability of U87 cells. (b) Cell viability of PIP-PC3 cells. All data are represented as mean ± SD and analyzed by two-way ANOVA; ns indicates no significance; n=5.

Given that short-term viability does not always correlate with long-term cell survival, we performed clonogenic assays under the same treatment conditions to assess the sustained radiosensitizing effects of 5-ALA combined with X-ray irradiation. Representative images are shown in Figure 4.3(a) for U87 and Figure 4.3(b) for PIP-PC3. The corresponding survival fractions are presented in Figure 4.3(c) and 4.3(d), respectively, with detailed values summarized in Table 4.1. X-ray irradiation with dose rate of 1.5 Gy/min reduced colony formation in U87 cells in a dose-dependent manner. Pre-treatment with 5-ALA significantly inhibited cell growth at 2 Gy ($p = 0.032$), 4 Gy ($p = 0.0067$), and 6 Gy ($p = 0.024$) compared to irradiation alone (Fig. 4.3(c)). For PIP-PC3, a dose-dependent reduction in colony formation was also observed. The addition of 5-ALA further suppressed colony formation, with significant effects at 1 Gy ($p = 0.026$), 2 Gy ($p = 0.0002$) and 3 Gy ($p = 0.0091$). To quantitatively evaluate the extent of radiosensitization induced by 5-ALA, the sensitizer enhancement ratio (SER) was calculated based on the surviving fraction curves. The resulting SER values were 1.29 for U87 cells and 1.49 for PIP-PC3 cells (Table S4.1).

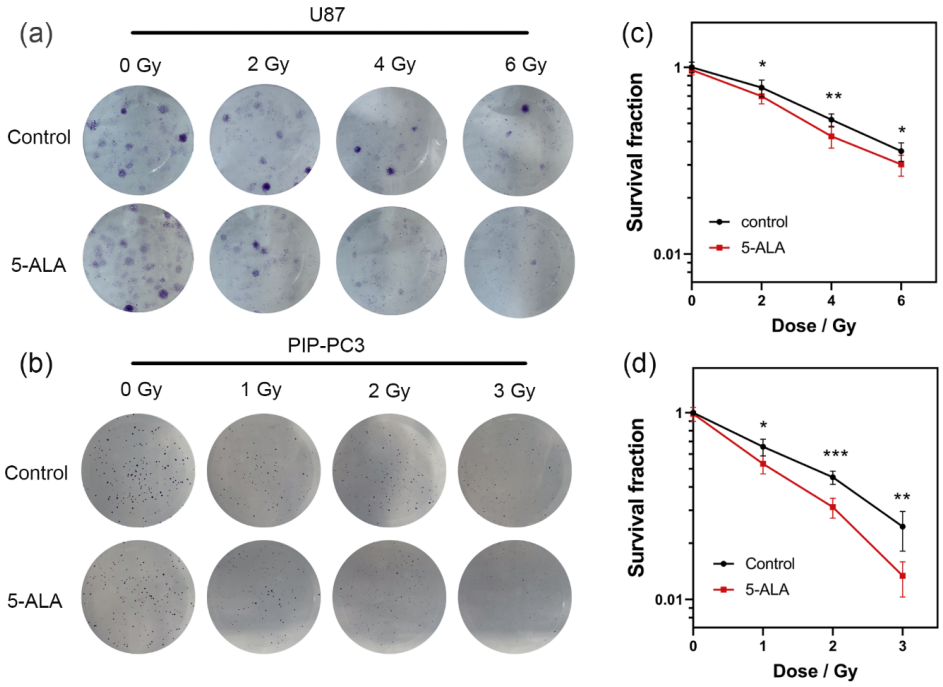

Figure 4.3. Colony formation of U87 and PIP-PC3 cells after combined 1 mM of 5-ALA pretreatment and X-ray irradiation at different doses with a dose rate of 1.5 Gy/min. (a) Representative images of U87 colonies following irradiation at 2, 4, and 6 Gy; the corresponding survival fractions are shown in (c). (b) Representative images of PIP-PC3 colonies following irradiation at 1, 2, and 3 Gy; the corresponding survival fractions are shown in (d). All data are represented as mean ± SD and analyzed by paired t-test; *$p < 0.05$, **$p < 0.01$, ***$p < 0.001$; n=6.

Table 4.1. *Survival fraction of U87 and PIP-PC3 after X-ray irradiation*

	U87				PIP-PC3			
	0 Gy	2 Gy	4 Gy	6 Gy	0 Gy	1 Gy	2 Gy	3 Gy
Control	1.00 ± 0.12	0.60 ± 0.11	0.27 ± 0.04	0.13 ± 0.03	1.00 ± 0.04	0.40 ± 0.07	0.20 ± 0.03	0.06 ± 0.02
5-ALA	0.93 ± 0.10	0.49 ± 0.07	0.18 ± 0.04	0.09 ± 0.02	0.97 ± 0.15	0.34 ± 0.07	0.10 ± 0.02	0.02 ± 0.01

DNA synthesis is essential for cell proliferation and takes place during the S phase of the cell cycle. When cells experience stress or DNA damage, they commonly undergo cell-cycle arrest in the G1 or G2 phase to give time for the repair process. To evaluate potential alterations in DNA replication following irradiation, we used 5-EdU, a thymidine analogue that is directly incorporated into newly synthesized DNA during the S phase and therefore serves as a reliable

marker of DNA synthesis. 5-EdU incorporation was assessed 48 h after 4 Gy irradiation, with or without 5-ALA, in U87 (Fig. 4.4(a)) and PIP-PC3 cells (Fig. 4.4(b)).

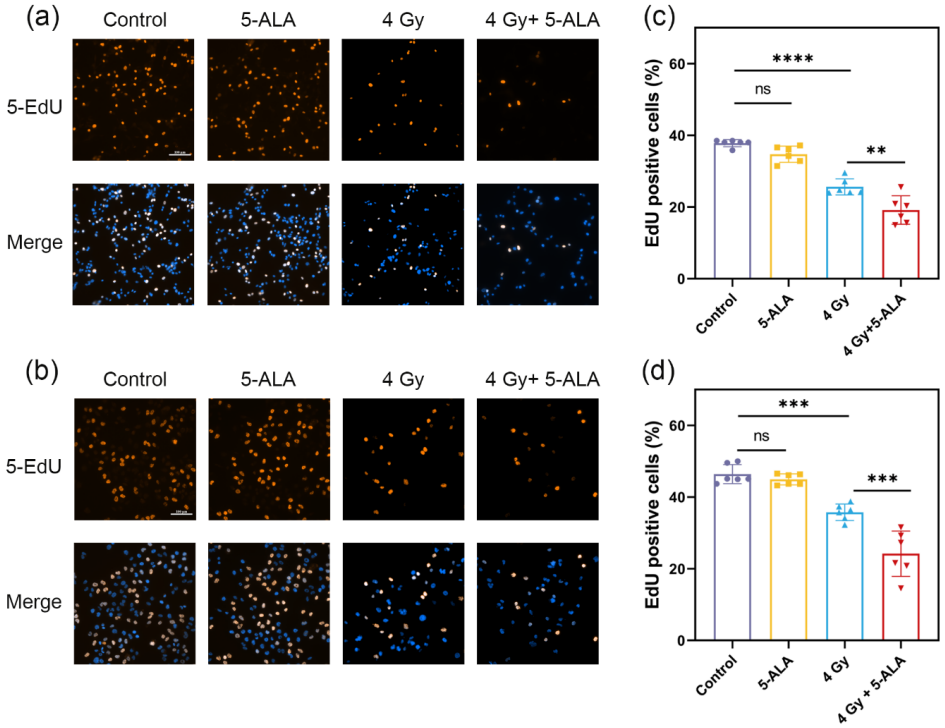

Figure 4.4. 5-EdU fluorescent staining (orange) and Hoechst 33342 nuclei staining (blue) of U87 and PIP-PC3 cells 48 h after 4 Gy X-ray irradiation with and without 1 mM 5-ALA pretreatment. (a) Fluorescence images of U87 and (c) corresponding quantification of 5-EdU positive cells. (b) Fluorescence images of PIP-PC3 and (d) corresponding quantification of 5-EdU positive cells. 6 microscope fields with over 35 cells per field were quantified. All data are represented as mean ± SD and analyzed by one-way ANOVA; ns indicates no significance, $^{**}p < 0.01$, $^{***}p < 0.0005$, $^{****}p < 0.0001$; n=6.

In U87 cells (Fig. 4.4(c)), 4 Gy irradiation significantly reduced the fraction of EdU-positive cells by 32% compared with the control group ($p < 0.0001$). Pre-treatment with 5-ALA produced an even greater reduction, decreasing the EdU-positive cell fraction by 50% compared with the control group, and a significant difference was detected between the 4 Gy and 4 Gy + 5-ALA groups ($p = 0.0018$). Similarly, in PIP-PC3 cells (Fig. 4.4(d)), 4 Gy irradiation caused a 23% decrease in EdU-positive cells compared with the control group ($p = 0.0004$). With 5-ALA pre-treatment, EdU-positive cells decreased by 48%, and the 4 Gy + 5-ALA group differed significantly from the 4 Gy group ($p = 0.0001$).

Cell proliferation following combined 5-ALA and yttrium-90 treatment

The radiosensitizing effect of 5-ALA was first demonstrated using X-rays at a dose rate of 1.5 Gy/min. We then investigated the impact of lower dose rates, comparable to those used in low-dose-rate (LDR) brachytherapy. We employed a [^{90}Y]Y foil as an external β^- radiation source, generated via neutron activation of stable ^{89}Y. By adjusting the activity of the foil, we were able to precisely control both the total dose and dose rate delivered to the cells. Dosimetric calibration was performed using EBT3 radiochromic film to establish and verify the dose rate before conducting cellular experiments. Colony formation results for U87 and PIP-PC3 cells irradiated at 2 Gy/h and 1 Gy/h, with total doses of 1 Gy and 3 Gy, are shown in Figure 5, with detailed survival fractions listed in Table 4.2.

For U87 cells receiving irradiation at a dose rate of 2 Gy/h, 1 Gy ^{90}Y irradiation alone did not suppress the growth of U87 cells compared to the non-irradiated control (Fig. 4.5(e)). In contrast, cells pretreated with 5-ALA exhibited significantly reduced growth following 1 Gy ^{90}Y irradiation compared to those receiving irradiation alone ($p = 0.0006$). At 3 Gy, ^{90}Y irradiation alone significantly inhibited U87 cell growth, and this effect was further enhanced by 5-ALA pretreatment ($p = 0.0083$). In PIP-PC3 cells (Fig. 4.5(g)), a dose-dependent growth inhibition was observed following ^{90}Y irradiation. At 1 Gy, growth was already reduced, and additional 5-ALA pretreatment did not further enhance the effect. At 3 Gy, however, 5-ALA pretreatment resulted in significantly enhanced growth inhibition compared to ^{90}Y irradiation alone ($p = 0.002$).

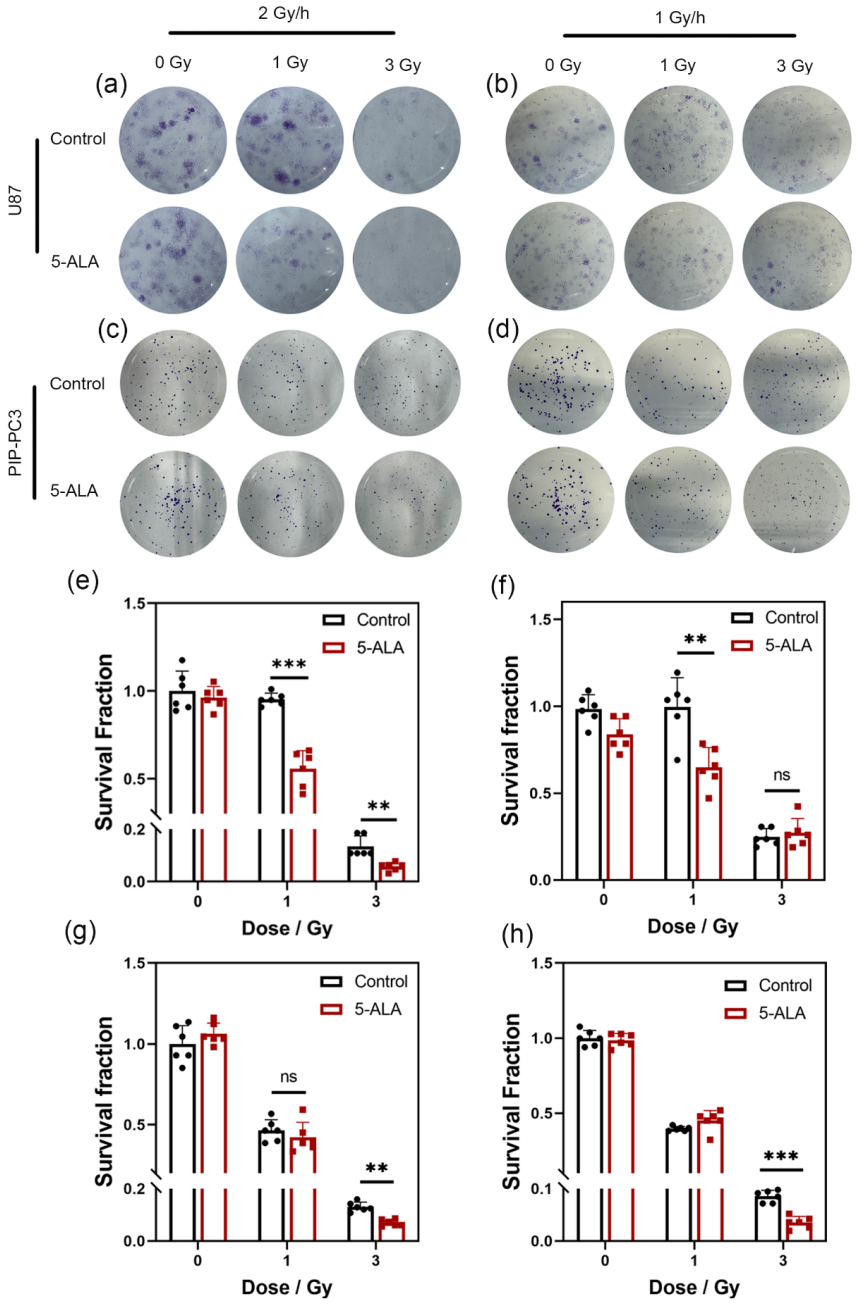

Figure 4.5. Colony formation and survival fractions of U87 and PIP-PC3 cells following treatment with 5-ALA and yttrium-90 irradiation (1 Gy and 3 Gy). Representative colony images (a–d) and corresponding survival fractions (e–h) are shown. (a, e) U87 cells irradiated at 2 Gy/h; (b, g) PIP-PC3 at 2 Gy/h; (c, f) U87 at 1 Gy/h; (d, h) PIP-PC3 at 1 Gy/h. All data are represented as mean ± SD and analyzed by paired t-test; ns indicates no significance, *p < 0.05, **p < 0.01, ***p < 0.0005; n=6.

Table 4.2. *Survival fraction of U87 and PIP-PC3 after ^{90}Y irradiation*

		U87			PIP-PC3		
		0 Gy	1 Gy	3 Gy	0 Gy	1 Gy	3 Gy
2 Gy/h	Control	1.00 ± 0.10	0.95 ± 0.03	0.13 ± 0.04	1.00 ± 0.10	0.47 ± 0.06	0.13 ± 0.02
	5-ALA	0.96 ± 0.06	0.56 ± 0.09	0.06 ± 0.01	1.06 ± 0.06	0.42 ± 0.08	0.07 ± 0.01
1 Gy/h	Control	1.00 ± 0.07	1.02 ± 0.16	0.25 ± 0.05	1.00 ± 0.05	0.40 ± 0.01	0.09 ± 0.01
	5-ALA	0.86 ± 0.08	0.66 ± 0.11	0.28 ± 0.08	0.99 ± 0.04	0.45 ± 0.06	0.04 ± 0.01

At the lower dose rate of 1 Gy/h, U87 cells did not show significant growth inhibition following 1 Gy ^{90}Y irradiation alone, whereas co-treatment with 5-ALA suppressed cell growth significantly ($p = 0.018$). At 3 Gy, the additional effect of 5-ALA was no longer observed (Fig. 4.5(f)). In PIP-PC3 cells (Fig. 4.5(h)), no difference was found between ^{90}Y irradiation alone and the combination treatment at 1 Gy. At 3 Gy, 5-ALA pre-treatment further reduced cell growth compared to irradiation alone ($p < 0.0009$).

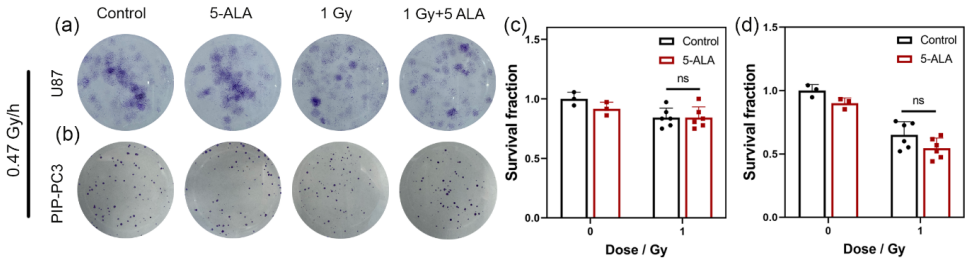

Figure 4.6. Colony formation of U87 and PIP-PC3 cells following combined treatment with 5-ALA and yttrium-90 irradiation at 1 Gy with a dose rate of 0.47 Gy/h. Representative images of colony formation are shown for (a) U87 and (b) PIP-PC3 cells. Corresponding survival fraction for U87 cells is presented in (c), and for PIP-PC3 cells in (d). All data are represented as mean ± SD and analyzed by paired t-test; ns indicates no significance; n=6.

When the dose rate was reduced to 0.47 Gy/h irradiation, the radiosensitizing effect previously observed at 1 Gy in U87 cells disappeared (Fig. 4.6(a) and 4.6(c)). PIP-PC3 cells also showed no enhancement with 5-ALA at this dose rate (Fig. 4.6(b) and 4.6(d)). At the lowest dose rate of 0.3 Gy/h, 5-ALA completely lost its radiosensitizing effect in both cell lines, and no significant difference was found between ^{90}Y irradiation alone and the combination treatment at 4 Gy in either U87 or PIP-PC3 cells (Fig. 4.7). Detailed survival fractions were listed in Table 4.3.

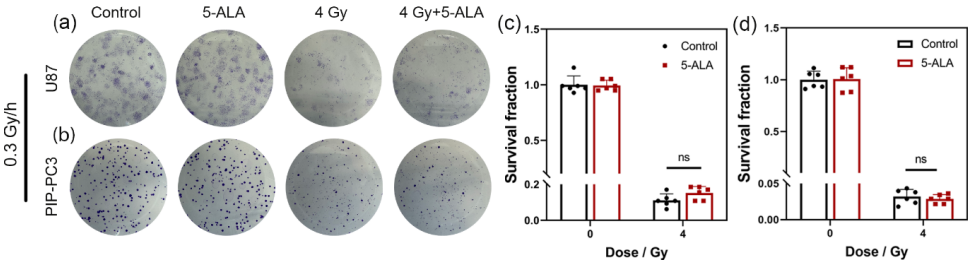

Figure 4.7. Colony formation of U87 and PIP-PC3 cells following combined treatment with 5-ALA and yttrium-90 irradiation at 1 Gy with a dose rate of 0.3 Gy/h. Representative images of colony formation are shown for (a) U87 and (b) PIP-PC3 cells. Corresponding survival fraction for U87 cells is presented in (c), and for PIP-PC3 cells in (d). All data are represented as mean ± SD and analyzed by paired t-test; ns indicates no significance; n=6.

Table 4.3. *Survival fraction of U87 and PIP-PC3 after ^{90}Y irradiation*

		U87		PIP-PC3	
		Control	5-ALA	Control	5-ALA
0.47 Gy/h	0 Gy	1.00 ± 0.05	0.91 ± 0.05	1.00 ± 0.04	0.90 ± 0.03
	1 Gy	0.84 ± 0.07	0.84 ± 0.08	0.65 ± 0.09	0.57 ± 0.06
0.3 Gy/h	0 Gy	1.00 ± 0.11	0.99 ± 0.04	1.00 ± 0.07	1.00 ± 0.10
	4 Gy	0.11 ± 0.32	0.15 ± 0.03	0.03 ± 0.01	0.03 ± 0.01

4.4 Discussion

The radiosensitizing effects of 5-ALA have been explored mainly in EBRT for the treatment of recurrent tumors, but radioresistance also remains a major challenge in other modalities, including brachytherapy and radionuclide therapy. A key distinction between these treatments and EBRT is the much lower dose rate typically involved. In this study, we first evaluated the radiosensitizing effect of 5-ALA under a clinically relevant EBRT dose rate using X-ray irradiation at 1.5 Gy/min (90 Gy/h). We then extended our investigation to low-dose-rate conditions using [^{90}Y]Y foil, which delivers initial dose rates ranging from 2 Gy/h to 0.3 Gy/h. The experiments were conducted in vitro using two human cancer cell lines, U87 glioblastoma and PIP-PC3 prostate cancer cells.

The accumulation of PpIX differed between U87 and PIP-PC3 cells. In both cell lines, PpIX fluorescence intensity peaked at 4 hours post-treatment with 5-ALA (Fig. 4.1). However, U87 cells exhibited a subsequent decline in fluorescence, whereas PIP-PC3 cells maintained relatively stable levels. In PIP-PC3 cells, increasing the 5-ALA concentration up to 2.5 mM led to a corresponding rise in PpIX fluorescence, but no further increase was observed at 5 mM or 10 mM, suggesting a saturable uptake or conversion mechanism, which is consistent with previous observations in prostate cancer cells[30]. In contrast, U87 cells showed no clear dose-dependent response to increasing 5-ALA concentrations, in line with findings reported by Bunk et al.[31] . These differences may be associated with variations in PpIX transport or metabolism, potentially involving ABC transporters such as ABCG2 and ABCB6, which have been implicated in regulating intracellular porphyrin levels.[32-34]

Three methods were used to evaluate the radiosensitizing effect of 5-ALA with X-rays on cell proliferation. Both the colony formation and 5-EdU assays demonstrated that 5-ALA enhanced the radiosensitivity of U87 and PIP-PC3 cells, indicating a clear inhibitory effect on proliferative capacity (Fig. 4.3 and Fig. 4.4). However, this effect was not detected by the CCK-8 assay (Fig. 4.2), which showed no significant differences under the same treatment conditions. The CCK-8 assay relies on the reduction of the tetrazolium salt by intracellular dehydrogenases using NADH and NADPH as electron donors.[35] As a result, it primarily reflects cellular metabolic activity rather than true proliferative potential. Previous work by Yamamori et al. demonstrated that cancer cells upregulated mitochondrial function following exposure to ionizing radiation to compensate for ROS-induced damage while sustaining mitochondrial activity.[36] Similarly, Ueta et al. reported that ionizing radiation combined with 5-ALA produced more ROS than radiation alone, which in turn led to increased mitochondrial mass and complex III activity as part of the cellular response to oxidative stresss.[18] This kind of metabolic adaptation may maintain NAD(P)H-dependent activity and hide early or moderate impairments in proliferation, thereby limiting the sensitivity of the CCK-8 assay in this context. In contrast, colony formation and 5-EdU assays reflect more direct aspects of reproductive capacity, making them more reliable in evaluating persistent cellular stress or damage.[37] The fact that both assays showed significant growth inhibition, while CCK-8 did not, suggests that 5-ALA may not immediately impair metabolic activity, but instead interferes with the ability of U87 and PIP-PC3 cells to replicate and divide. This may be explained by mitochondrial dysfunction that persists despite initial compensatory responses, eventually leading to insufficient energy production for cell proliferation and thereby reducing the proliferative capacity even when

short-term metabolic viability appears unaffected.[38,39] These findings suggest that the additional damage caused by 5-ALA involves mitochondrial and redox-mediated stress responses rather than acute cytotoxicity.

Given that this ROS-based radiosensitizing effect depends on both their generation and accumulation, it is influenced not only by the presence of intracellular PpIX and irradiation, but also by how these stress inducers are delivered over time. ROS plays a dual role in tumor biology: while excessive ROS levels can induce cell death by causing mitochondrial disfunction, DNA damage and activation of cell death pathways, low to moderate levels may support tumor proliferation by activating pro-survival signaling pathways.[40] In this context, the radiation dose rate becomes particularly important, as it influences the dynamics of ROS production.[41] The results of the clonogenic assay suggest a general trend that the radiosensitizing effect of 5-ALA tends to decrease as the dose rate is reduced in both U87 and PIP-PC3 cells. In U87 cells, the radiosensitizing effect observed at 1 Gy was still present at a dose rate of 1 Gy/h (Fig. 4.5(b) and 4.5(f)), while the effect was no longer evident at 0.5 Gy/h (Fig. 4.6(a) and 4.6(c)). In PIP-PC3 cells, the effect remained detectable at 3 Gy and 1 Gy/h (Fig. 4.5(d) and 4.5(h)) but became less obvious at lower dose rates such as 0.3 Gy/h with 4 Gy irradiation (Fig. 4.7(b) and 4.7(d)). These results suggest that at lower dose rates, the additional ROS generated by PpIX may be reduced below the threshold needed to induce sufficient cytotoxicity. This corresponds with the findings that lower dose rates produce fewer dense ROS clusters, resulting in reduced lethal damage and a greater proportion of sublethal damage, which may be more efficiently repaired by the cells.[42,43] To be noticed, in U87 cells, a radiosensitizing effect was observed at 1 Gy delivered at 1 Gy/h, but this effect was absent when 3 Gy was delivered at the same dose rate (Fig. 4.5(f)). This non-linear response, where higher doses do not produce stronger effects as expected, suggests that additional factors are involved. One possible explanation is that the prolonged irradiation time required to deliver 3 Gy at 1 Gy/h (3 h) provided sufficient time for cellular antioxidant defense activation, reducing ROS accumulation and counteracting radiosensitization.

This hypothesis is further supported by previous findings showing that low-dose-rate (LDR) irradiation activate antioxidant responses that diminish radiation-induced oxidative damage.[44-47] Godoy et al. demonstrated that U87 glioblastoma neurospheres were more resistant under LDR γ-irradiation (24 mGy/h) compared to high-dose-rate (HDR, 0.39 Gy/min).[48] They observed increased extracellular release of 8-oxo-dG in neurospheres under LDR conditions. As a marker of oxidative nucleotide clearance, elevated extracellular 8-oxo-dG indicates active

detoxification rather than increased damage, suggesting that LDR allows sufficient time for stress detection and the activation of antioxidant defenses. In contrast, HDR delivers oxidative injury more rapidly than the cell can manage, leading to more persistent intracellular damage and increased radiosensitization. These antioxidant defenses are largely regulated by the nuclear factor erythroid 2-related factor 2 (Nrf2), a transcription factor that controls the expression of key enzymes including superoxide dismutases (SODs), catalase (CAT), and glutathione peroxidase (GPx). Godoy et al. further confirmed the essential role of Nrf2 in this context by showing that Nrf2 silencing in U87 cells significantly enhanced radiosensitivity under LDR conditions. This implies that Nrf2-mediated antioxidant adaptation contributes to the reduced cytotoxicity observed at low dose rates. Although direct evidence of the relationship between Nrf2 and LDR in prostate cancer is limited, studies have shown that Nrf2 also regulates antioxidant responses in prostate cancer cells,[49,50] suggesting that similar adaptive mechanisms may exist in PIP-PC3. While mitochondrial ROS such as superoxide are critical for 5-ALA-mediated radiosensitization via PpIX,[19] their biological effects may be diminished if ROS are promptly neutralized.

Except for the dose rate effect, the concentration of PpIX should also be considered. As discussed earlier, although both glioblastoma and prostate cancer cells can accumulate PpIX, they also possess metabolic pathways that transport and remove it from mitochondria. A lower dose rate inevitably leads to a longer irradiation time, which might be unable to deliver sufficient radiation during the early phase when the PpIX concentration is at its peak. As a result, the irradiation does not fully take advantage of the optimal window concentration for ROS generation.

Another factor that has not been fully considered here is the energy of the radiation. The X-rays used in this study have lower photon energies than the β^- particles emitted by ^{90}Y. Because the higher-energy β^- radiation generally exhibits lower linear energy transfer (LET), which should also be taken into account in future studies. Additionally, for the 4 Gy irradiation delivered by [^{90}Y]Y foil at the dose rate of 0.3 Gy/h, we lack a proper comparison group irradiated with X-rays. While the reduced radiosensitizing effect of 5-ALA at lower dose rate is clear in U87 cells, the situation might be different for PIP-PC3 cells. This cell line is generally more sensitive to radiation, and a 4 Gy exposure may have already eliminated most cells, making it difficult to observe any additional radiosensitizing effect.

4.5 Conclusion

In this work, we examined the radiosensitizing effects of 5-ALA across a range of dose rates in glioblastoma U87 and prostate cancer PIP-PC3 cells, covering both the dose rate typically used in conventional EBRT (1.5 Gy/min) and the lower dose rates relevant to LDR brachytherapy (< 2 Gy/h). At 1.5 Gy/min X-ray irradiation, 5-ALA produced a pronounced radiosensitizing effect in both cell lines. However, this radiosensitizing effect progressively diminished as the dose rate decreased and ultimately disappeared under continuous low-dose-rate irradiation by ^{90}Y. Although the exact mechanism remains unclear, the loss of radiosensitization at low dose rates may be related to the balance between ROS production from 5-ALA-induced PpIX and the activation of antioxidants, and repair systems. When irradiation is delivered slowly, as in the ^{90}Y exposure, cells may have enough time to compensate for oxidative stress, reducing the impact of 5-ALA on radiation response. Future mechanistic studies examining ROS generation and antioxidant activity across different dose rates will be important to clarify this effect.

Overall, our results suggest that the radiosensitizing behavior of 5-ALA depends on the dose rate of the ionizing radiation. Considering dose-rate effects may therefore be important when integrating photosensitizers into radiotherapy strategies.

References

1 Vignard, J., Mirey, G. & Salles, B. Ionizing-radiation induced DNA double-strand breaks: A direct and indirect lighting up. *Radiotherapy and Oncology* **108**, 362-369 (2013).

2 Roots, R. & Okada, S. Estimation of life times and diffusion distances of radicals involved in x-ray-induced DNA strand breaks of killing of mammalian cells. *Radiat Res* **64**, 306-320 (1975).

3 Dizdaroglu, M. & Jaruga, P. Mechanisms of free radical-induced damage to DNA. *Free Radical Research* **46**, 382-419 (2012).

4 Lomax, M. E., Folkes, L. K. & O'Neill, P. Biological Consequences of Radiation-induced DNA Damage: Relevance to Radiotherapy. *Clinical Oncology* **25**, 578-585 (2013).

5 Hall, E. J. & Giaccia, A. J. Radiobiology for the Radiologist. *International Journal of Radiation Oncology, Biology, Physics* **66**, 627 (2006).

6 Chen, H. H. W. & Kuo, M. T. Improving radiotherapy in cancer treatment: Promises and challenges. *Oncotarget* **8**, 62742-62758 (2017).

7 Tzerkovsky, D. A., Mazurenko, A. N., Borychevsky, F. F. & Shashkouski, D. V. Radiodynamic Therapy with Photosensitizers: Mini-Review of Experimental and Clinical Studies. *Journal of Analytical Oncology* **11**, 79-85 (2022).

8 Takahashi, J. & Misawa, M. Characterization of reactive oxygen species generated by protoporphyrin IX under X-ray irradiation. *Radiation Physics and Chemistry* **78**, 889-898 (2009).

9 Schaffer, M., Ertl-Wagner, B., Schaffer, P. M., Kulka, U. *et al.* Feasibility of Photofrin II as a Radiosensitizing Agent in Solid Tumors – Preliminary Results. *Oncologie* **29**, 514-519 (2006).

10 ClinicalTrials.gov Identifier: NCT05590689.

11 Takahashi, J., Nagasawa, S., Doi, M., Takahashi, M. *et al.* In Vivo Study of the Efficacy and Safety of 5-Aminolevulinic Radiodynamic Therapy for Glioblastoma Fractionated Radiotherapy. *International Journal of Molecular Sciences* **22**, 9762 (2021).

12 Takahashi, J., Murakami, M., Mori, T. & Iwahashi, H. Verification of radiodynamic therapy by medical linear accelerator using a mouse melanoma tumor model. *Scientific Reports* **8**, 2728 (2018).

13 Ling CC, Gerweck LE, Zaider M & E., Y. Dose-rate effects in external beam radiotherapy redux. *Radiotherapy and oncology : journal of the European Society for Therapeutic Radiology and Oncology* **95**, 261-268 (2010).

14 Zhang, S., Wang, X., Gao, X., Chen, X. *et al.* Radiopharmaceuticals and their applications in medicine. *Signal Transduction and Targeted Therapy* **10** (2025).

15 Maesaka, F., Nakai, Y., Yoshida, T., Tomizawa, M. *et al.* 5-Aminolevulinic Acid: A Novel Approach to Improving Radioresistance in Prostate Cancer. *Cancers* **17**, 1286 (2025).

16 Harada, Y., Murayama, Y., Takamatsu, T., Otsuji, E. & Tanaka, H. 5-Aminolevulinic Acid-Induced Protoporphyrin IX Fluorescence Imaging for Tumor Detection: Recent Advances and Challenges. *International Journal of Molecular Sciences* **23**, 6478 (2022).

17 Hadjipanayis, C. G. & Stummer, W. 5-ALA and FDA approval for glioma surgery. *Journal of Neuro-Oncology* **141**, 479-486 (2019).

18 Ueta, K., Yamamoto, J., Tanaka, T., Nakano, Y. *et al.* 5-Aminolevulinic acid enhances mitochondrial stress upon ionizing irradiation exposure and increases delayed production of reactive oxygen species and cell death in glioma cells. *International Journal of Molecular Medicine* **39**, 387-398 (2017).

19 Owari, T., Tanaka, N., Nakai, Y., Miyake, M. *et al.* 5-Aminolevulinic acid overcomes hypoxia-induced radiation resistance by enhancing mitochondrial reactive oxygen species production in prostate cancer cells. *British Journal of Cancer* **127**, 350-363 (2022).

20 Pasciak, A. S., Manupipatpong, S., Hui, F. K., Gainsburg, L. *et al.* Yttrium-90 radioembolization as a possible new treatment for brain cancer: proof of concept and safety analysis in a canine model. *EJNMMI Research* **10**, 104 (2020).

21 Heute, D., Kostron, H., Von Guggenberg, E., Ingorokva, S. *et al.* Response of Recurrent High-Grade Glioma to Treatment with ^{90}Y-DOTATOC. *Journal of Nuclear Medicine* **51**, 397-400 (2010).

22 Ansari, S., Cantrell, D., Tate, M., Dixit, K. *et al.* in *SNIS 20th annual meeting oral abstracts* A30.31-A30 (BMJ Publishing Group Ltd., 2023).

23 Gordon, J. A., Pasli, M., Cook, C. M., Connor, R. *et al.* Novel combination of GammaTile cesium-131 brachytherapy with 5-aminolevulinic acid fluorescence-guided resection in the re-irradiation of pediatric recurrent high-grade glioma: illustrative case. *J Neurosurg Case Lessons* **6**, CASE23346 (2023).

24 Wei, S., Li, C., Li, M., Xiong, Y. *et al.* Radioactive Iodine-125 in Tumor Therapy: Advances and Future Directions. *Frontiers in Oncology* **11**, 717180 (2021).

25 Miyake, M., Tanaka, N., Ohnishi, K., Nakai, Y. *et al.* Oral 5-aminolevulinic Acid for Patients With Localized Prostate Cancer Undergoing Low-dose-rate Brachytherapy: AMBER Trial. *In Vivo* **38**, 3091-3105 (2024).

26 Leo, S., Gutierrez, N. M. C., Bulin, A.-L., Coll, J.-L. *et al.* The physicochemical and biochemical mechanisms of porphyrinoid-mediated radiodynamic therapy. *European Journal of Medicinal Chemistry* **296**, 117861 (2025).

27 Oberley, T. D. & Oberley, L. W. Antioxidant enzyme levels in cancer. *Histology and Histopathology* **12**, 525-535 (1997).

28 Hall, E. J. Radiation Dose-Rate: A Factor of Importance in Radiobiology and Radiotherapy. *British Journal of Radiology* **45**, 81-97 (1972).

29 Mazeron, J., Scalliet, P., Van Limbergen, E. & Lartigau, E. Radiobiology of brachytherapy and the dose-rate effect. *The GEC-ESTRO handbook of brachytherapy. Brussels: ESTRO*, 95-121 (2002).

30 Yamamoto, S., Fukuhara, H., Seki, H., Kawada, C. *et al.* Predictors of therapeutic efficacy of 5-aminolevulinic acid-based photodynamic therapy in human prostate cancer. *Photodiagnosis and Photodynamic Therapy* **35**, 102452 (2021).

31 Bunk, E. C., Wagner, A., Stummer, W., Senner, V. & Brokinkel, B. 5-ALA kinetics in meningiomas: analysis of tumor fluorescence and PpIX metabolism in vitro and comparative analyses with high-grade gliomas. *Journal of Neuro-Oncology* **152**, 37-46 (2021).

32 Mcnicholas, K., Macgregor, M. N. & Gleadle, J. M. In order for the light to shine so brightly, the darkness must be present—why do cancers fluoresce with 5-aminolaevulinic acid? *British Journal of Cancer* **121**, 631-639 (2019).

33 Zhao, S.-G., Chen, X.-F., Wang, L.-G., Yang, G. *et al.* Increased Expression of ABCB6 Enhances Protoporphyrin IX Accumulation and Photodynamic Effect in Human Glioma. *Annals of Surgical Oncology* **20**, 4379-4388 (2013).

34 Kobuchi, H., Moriya, K., Ogino, T., Fujita, H. *et al.* Mitochondrial Localization of ABC Transporter ABCG2 and Its Function in 5-Aminolevulinic Acid-Mediated Protoporphyrin IX Accumulation. *PloS One* **7**, e50082 (2012).

35 Chamchoy, K., Pakotiprapha, D., Pumirat, P., Leartsakulpanich, U. & Boonyuen, U. Application of WST-8 based colorimetric NAD(P)H detection for quantitative dehydrogenase assays. *BMC Biochemistry* **20**, 4

(2019).

36 Yamamori, T., Yasui, H., Yamazumi, M., Wada, Y. *et al.* Ionizing radiation induces mitochondrial reactive oxygen species production accompanied by upregulation of mitochondrial electron transport chain function and mitochondrial content under control of the cell cycle checkpoint. *Free Radical Biology and Medicine* **53**, 260-270 (2012).

37 Forgie, B. N., Prakash, R., Goyeneche, A. A. & Telleria, C. M. Vitality, viability, long-term clonogenic survival, cytotoxicity, cytostasis and lethality: what do they mean when testing new investigational oncology drugs? *Discover Oncology* **15**, 5 (2024).

38 Srinivas, U. S., Tan, B. W. Q., Vellayappan, B. A. & Jeyasekharan, A. D. ROS and the DNA damage response in cancer. *Redox Biology* **25**, 101084 (2019).

39 Yoshida, T., Goto, S., Kawakatsu, M., Urata, Y. & Li, T.-S. Mitochondrial dysfunction, a probable cause of persistent oxidative stress after exposure to ionizing radiation. *Free Radical Research* **46**, 147-153 (2012).

40 Nakamura, H. & Takada, K. Reactive oxygen species in cancer: Current findings and future directions. *Cancer Science* **112**, 3945-3952 (2021).

41 Kusumoto, T., Danvin, A., Mamiya, T., Arnone, A. *et al.* Dose Rate Effects on Hydrated Electrons, Hydrogen Peroxide, and a OH Radical Molecular Probe Under Clinical Energy Protons. *Radiation Research* **201**, 287-293 (2024).

42 Vilenchik, M. M. & Knudson, A. G. Inverse radiation dose-rate effects on somatic and germ-line mutations and DNA damage rates. *Proceedings of the National Academy of Sciences* **97**, 5381-5386 (2000).

43 Meng, Q., Zaharieva, E. K., Sasatani, M. & Kobayashi, J. Possible relationship between mitochondrial changes and oxidative stress under low dose-rate irradiation. *Redox Report* **26**, 160-169 (2021).

44 De Toledo, S. M., Asaad, N., Venkatachalam, P., Li, L. *et al.* Adaptive Responses to Low-Dose/Low-Dose-Rate γ Rays in Normal Human Fibroblasts: The Role of Growth Architecture and Oxidative Metabolism. *Radiation Research* **166**, 849-857 (2006).

45 Lee, H.-C., Kim, D.-W., Jung, K.-Y., Park, I.-C. *et al.* Increased expression of antioxidant enzymes in radioresistant variant from U251 human glioblastoma cell line. *International Journal of Molecular Medicine* **13**, 883-887 (2004).

46 Bravard, C. L., E. Moustacchi, A. Contribution of antioxidant enzymes to the adaptive response to ionizing radiation of human lymphoblasts. *International Journal of Radiation Biology* **75**, 639-645 (1999).

47 Vieira Dias, J., Gloaguen, C., Kereselidze, D., Manens, L. *et al.* Gamma Low-Dose-Rate Ionizing Radiation Stimulates Adaptive Functional and Molecular Response in Human Aortic Endothelial Cells in a Threshold-, Dose-, and Dose Rate–Dependent Manner. *Dose-Response* **16**, 155932581875523 (2018).

48 JD, H. & AT, D.-K. The Nrf2 regulatory network provides an interface between redox and intermediary metabolism. *Trends in biochemical sciences* **39**, 199-218 (2014).

49 Kalinina, E. V., Gavriliuk, L. A. & Pokrovsky, V. S. Oxidative Stress and Redox-Dependent Signaling in Prostate Cancer. *Biochemistry (Moscow)* **87**, 413-424 (2022).

50 Khandrika, L., Kumar, B., Koul, S., Maroni, P. & Koul, H. K. Oxidative stress in prostate cancer. *Cancer Letters* **282**, 125-136 (2009).

Supporting information

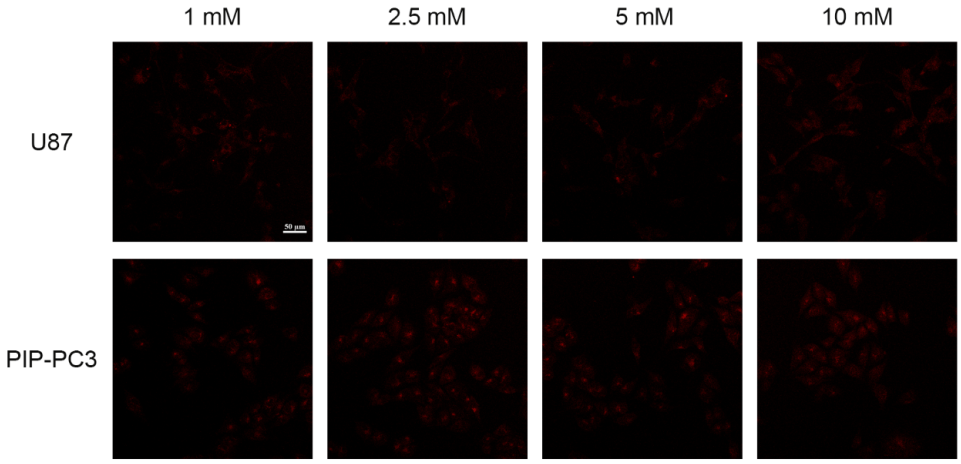

Figure S4.1. Intracellular PpIX fluorescence images of U87 and PIP-PC3 cells 4 hours after treatment with 5-ALA at concentrations of 1 mM, 2.5 mM, 5 mM, and 10 mM. Scale bar = 50 µm.

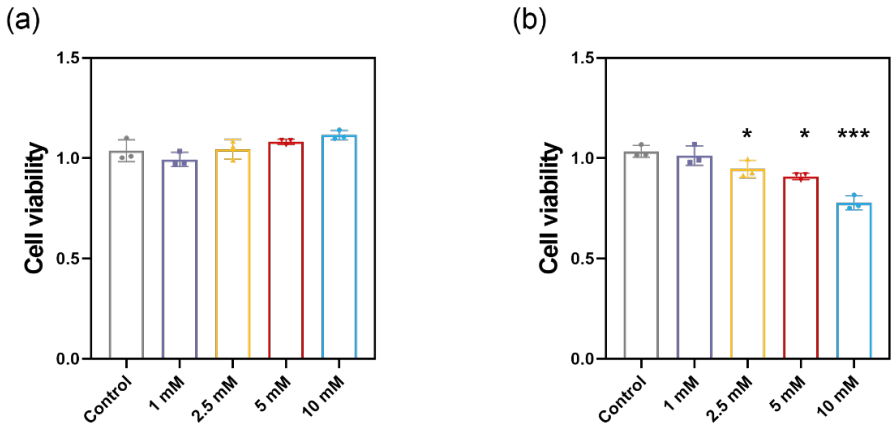

Figure S4.2. Cytotoxicity of 5-ALA at varying concentrations in (a) U87 cells and (b) PIP-PC3 cells. Cells treated with different concentrations of 5-ALA were compared with the untreated control group. All data are represented as mean ± SD and analyzed by one-way ANOVA; *$p < 0.05$, ***$p < 0.0005$; n=3.

Group	D_0 (Gy)	SER
U87	3.31	1.00
U87 + 5-ALA	2.57	1.29
PIP-PC3	1.20	1.00
PIP-PC3 + 5-ALA	0.81	1.48

Table S4.1. Radiobiological parameters D_0 and sensitizer enhancement ratio (SER) for U87 and PIP-PC3 cells with and without 5-ALA. D_0 values were obtained from the exponential portion of the survival curves, and SER was calculated as the ratio of D_0 in the absence of 5-ALA to that in the presence of 5-ALA.

Chapter 5

5-Aminolevulinic Acid Enhances the Therapeutic Effect of Lutetium-177 During Low Dose Rate Exposure in Prostate Cancer Cells

Abstract

Metastatic castration resistant prostate cancer (mCRPC) is an aggressive, androgen independent disease. Targeted radionuclide therapy with [^{177}Lu]Lu-PSMA-617 has improved outcomes, yet only about 50% of patients respond to the treatment. Docetaxel based combinations have shown to increase efficacy but are often poorly tolerated in elderly or medically compromised patients. As an alternative treatment strategy, we evaluated 5-aminolevulinic acid (5-ALA) as a potentially well tolerated radiosensitizer in combination with ^{177}Lu-based treatment. The radiosensitizing effect of 5-ALA was assessed in PIP-PC3 cells, a mCRPC driven prostate cancer model transfected to express PSMA. Cell survival after ^{177}Lu irradiation showed an inverse dose rate effect across 2 Gy/h to 0.05 Gy/h at total doses of 2 Gy and 4 Gy. 5-ALA further enhanced ^{177}Lu induced cell killing at dose rates below 0.1 Gy/h for both 2 Gy and 4 Gy, within the clinically reported dose rate range used with [^{177}Lu]Lu-PSMA-617. The preliminary three-dimensional spheroid results show that the combination of ^{177}Lu and 5-ALA reduced spheroid growth compared with either treatment alone. These findings suggest 5-ALA is a radiosensitizer with the potential to improve ^{177}Lu-based therapy for patients having mCRPC.

Keywords: Lutetium-177, 5-aminolevulinic acid, prostate cancer, radiosensitizing, low dose rate

5.1 Introduction

Prostate cancer is the most common cancer among men and remains a leading cause of cancer-related mortality.[1] Early-stage disease may be managed through surgery or radiotherapy. However, many patients experience disease progression following initial treatment, with some eventually developing advanced or metastatic disease. For these patients, hormonal therapy, initially through androgen deprivation therapy (ADT), is critical for disease control by suppressing androgen production or blocking androgen receptor signaling.[2] Despite initial effectiveness, the disease often follows a predictable course. Most patients experience a period of ADT sensitivity, but over time, usually within 18 to 24 months for metastatic cases,[3] cancer cells adapt to proliferate despite castrate levels of serum testosterone (20 ng/dL).[4] This gradual loss of sensitivity to androgen suppression leads to the development of castration-resistant prostate cancer (CRPC). Nonmetastatic CRPC is usually managed with continued ADT together with an androgen receptor pathway inhibitor (ARPI). Treatment of metastatic CRPC (mCRPC) often requires additional chemotherapy using drugs such as docetaxel and cabazitaxel.[5-7] However, these therapies show limited efficacy and elderly patients often cannot tolerate aggressive regimens, making mCRPC treatment still challenging.[8]

The novel radiopharmaceutical lutetium 177 radiolabeled PSMA-617 ([^{177}Lu]Lu-PSMA-617) has emerged as a treatment option for mCRPC by targeting prostate-specific membrane antigen (PSMA), which is overexpressed in most mCRPC cases.[9] The phase 3 VISION trial showed that [^{177}Lu]Lu-PSMA-617 improved overall survival in patients with PSMA-positive mCRPC who had previously received at least one ARPI and one taxane regimen, and it has since then been approved by the U.S. Food and Drug Administration (FDA).[10] Despite this clinical benefit, only about half of the patients responded to treatment, and tumor remission was maintained only for a short period.[11-13] The reasons for treatment failure may include tumor heterogeneity leading to low PSMA expression levels, the development of radioresistant tumor cells, or insufficient radiation dose delivery to metastatic sites.[14] Currently, potential strategies that can help express more PSMA, increase tumor radiosensitivity and complement antitumor effects, are being explored to improve [^{177}Lu]Lu-PSMA-617 based treatment.[15]

Our interest is to explore photosensitizers (PSs) as potential radiosensitizers,[16] with the aim of supporting the further potential use of ^{177}Lu-based therapy. PSs can enhance the production of reactive oxygen species (ROS) under ionizing radiation, and they have little or no toxicity in dark, which makes them more suitable for patients who cannot tolerate aggressive treatments.

Among these PSs, 5-aminolevulinic acid (5-ALA), a precursor of protoporphyrin IX, has been most widely studied in prostate cancer as a radiosensitizer with external beam radiation in both *in vitro* and *in vivo* studies.[17-19] However, no study has investigated its radiosensitizing effect when combined with therapeutic radionuclides like ^{177}Lu in the treatment of prostate cancer. One concern when moving from external radiation to radionuclide therapy is the difference in dose rate. Delbart et al. compared [^{177}Lu]Lu-DOTATATE with external beam radiation and found that, although both had radiobiological effects, [^{177}Lu]Lu-DOTATATE produced a weaker response despite the higher delivered dose, and the radiosensitizing effect of poly (ADP-ribose) polymerase inhibition (PARPi) was also reduced. This was likely due to the lower dose rate delivered by [^{177}Lu]Lu-DOTATATE. In Chapter 4, we showed that pretreatment with 5-ALA enhanced the radiosensitivity of PIP-PC3 cells under X-ray irradiation (250 kV, 1.5 Gy/min), and the effect clearly depended on dose rates, where only dose rates above 1 Gy/h delivered by yttrium-90 (β^-, average energy 935 keV) showed radiosensitization. ^{177}Lu has different properties than ^{90}Y, it has a longer half-life resulting in lower dose rate even at clinically used activities and it emits lower energy β^- particles (average energy 134 keV).[20,21] Therefore, it is unclear whether 5-ALA can still provide any radiosensitizing effect when using irradiation.

In this study, we investigated the radiosensitizing effect of 5-ALA combined with ^{177}Lu irradiation in PIP-PC3 cells. PIP-PC3 cells are PC3 cells transfected to express PSMA, while the parental PC3 line is derived from a metastatic prostate cancer patient and lacks androgen receptor expression. We first examined how the dose rate of ^{177}Lu influences the radiosensitizing effect of 5-ALA in two-dimensional cell monolayers by adjusting the activity and incubation period based on Monte Carlo simulations. The response was evaluated using clonogenic assays. We then moved to three-dimensional spheroid models to perform a preliminary test of the radiosensitizing effect of 5-ALA in a more complex cell environment.

5.2 Materials and Methods

Cell culture

Prostate cell line PIP-PC3 with stable PSMA expressions were kindly provided by ErasmusMC and were used in the experiments. PIP-PC3 cells were cultured in Roswell Park Memorial Institute (RPMI) 1640 with L-glutamine (VWR chemicals), supplemented with 10% fetal

bovine serum (Biowest) and 1X penicillin-streptomycin solution (VWR chemicals). All cells were incubated with a humidified atmosphere containing 5% CO_2 at 37 ºC.

Monto Carlo simulations

To estimate the dose rate Monte Carlo (MC) simulations were implemented, using the Geant4 toolkit (v11.3.2). In the simulation models, the radiological behavior of a standard 48-well plate (VWR 48-Well Tissue Culture Plates) was used. The computational geometry consisted of a water-filled cubic world of half-extents 15.0 cm (i.e., a 30×30×30 cm^3 box) that contained a polystyrene plate centered at the origin and oriented normal to the z axis. The plate dimensions were 12.83 cm × 8.58 cm in the x–y plane with a thickness of 2.0 cm. Within the plate were an array of 48 cylindrical wells arranged in 6 rows by 8 columns; each well had an inner radius of 0.552 cm and was filled with liquid water representing a 100 μL sample (water volume = 0.1 cm^3) (Fig. 5.1(a)). The water column height in each well was computed from the specified well volume and the circular well area (height = water_volume / (π·wellRadius^2)), which yielded a full height $\approx$ 0.1045 cm and a half-height used in geometry placement $\approx$ 0.05225 cm; the water was placed near the bottom of the plate so that the well centers were offset by z_shift = −(plate_half_height) + wellHalfHeight where plate_half_height = 1.0 cm. Well centers were laid out on a regular grid with spacing 1.3 cm in both x and y; x positions use xPos[j] = (j − 3.5)·1.3 cm for j $\in$ [0..7] and y positions use yPos[i] = (2.5 − i)·1.3 cm for i $\in$ [0..5].

The source model used a single-particle gun configured to emit radioactive ions (via Geant4's `G4IonTable`). The specific isotope was selected at runtime through the macro (for example, init_vis.mac uses `/gun/ion 71 177` to select ^{177}Lu. For each event the primary generator chose a well uniformly at random (integer index 0–47), then sampled a uniformly distributed position inside the cylindrical water volume: radius sampled as r = maxRadius·sqrt(U) (uniform disk sampling), angle θ uniform in [0, 2π), and z uniform between zMin and zMax where the code insets the sampling region to 95% of the geometric boundaries (maxRadius = 0.95·wellRadius and z bounds multiplied by 0.95) to avoid edge effects. The particle position was translated to the selected well center and the particle was located in the geometry with the navigator before vertex generation to ensure correct region assignment.

Physics processes combined an electromagnetic model tuned for low-energy accuracy with radioactive decay: specifically the physics list registers `G4EmStandardPhysics_option4`, `G4DecayPhysics`, and `G4RadioactiveDecayPhysics`. Electromagnetic parameters were adjusted for consistent behavior in multithreaded runs by setting the multiple scattering range

factor to 0.04 (`G4EmParameters::Instance()->SetMscRangeFactor(0.04)`) and enabling uniform cuts across threads (`SetApplyCuts(true)`).

Scoring was implemented through two complementary mechanisms. A per-well sensitive detector was attached to each well as a `G4MultiFunctionalDetector` with a `G4PSEnergyDeposit` primitive scorer, producing per-well energy deposition tallies. In addition, the included runtime macro init_vis.mac configured a Geant4 scoring mesh named `wellMesh` with a single bin (mesh box size 10.4 cm × 7.8 cm × 1.62 cm and `nBin 8 6 8`, Fig. 5.1(b)) and requested `energyDeposit` (eDep) quantity; the macro then executes `/run/beamOn 10000000` to ensure low statistical uncertainty and dumped the mesh results to the text file `wellMesh48Edep.txt`. In Figure 5.1(b), X-rays and gamma-rays deposited energy in neighboring wells, which can introduce small well-to-well differences in the energy deposition map. For dose rate quantification, a large statistics simulation (10,000,000 events) was used, for which the well-to-well variation in energy deposition from X-rays and gamma-rays was below 1% and therefore considered negligible. The calculated dose rates are presented in Table 5.1.

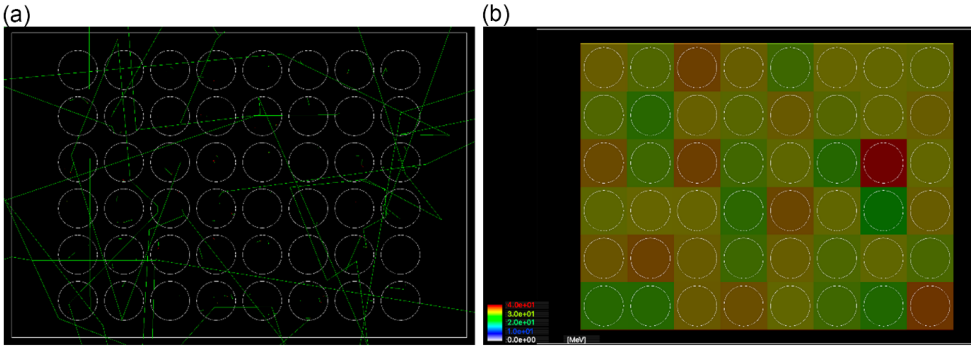

Figure 5.1. The 48 wells plate geometry, including (a) photons and electrons interactions, as produced using ^{177}Lu ion source, and (b) the energy deposition scorer, as split to extract the energy of each well (10,000 events).

Clonogenic assay

[^{177}Lu]$LuCl_3$ in 0.1 M HCl was kindly provided by ErasmusMC and used for all irradiation experiments. Typically, the stock solution of [^{177}Lu]$LuCl_3$ was diluted with sterile Milli-Q water to prepare solutions in which the desired activity was contained in a fixed volume of 10 µL. For each irradiation condition, 10 µL of the appropriately diluted [^{177}Lu]$LuCl_3$ solution was added to the cells.

To evaluate the radiosensitizing effect of 5-ALA combined with [^{177}Lu]$LuCl_3$ in PIP-PC3 cells using clonogenic assay, PIP-PC3 cells were seeded in 48-well plates at a density of 30,000 cells per well and incubated overnight for attachment. The next day, cells were treated with 500 µL of complete RPMI containing 1 mM 5-ALA for 4 h to allow intracellular accumulation, after which the medium was removed and cells were washed twice with PBS. Following 5-ALA treatment, cells were exposed to [^{177}Lu]$LuCl_3$ at different activities and incubation periods. The irradiation settings were selected based on Monte Carlo simulations to deliver absorbed doses of 2 Gy or 4 Gy, as summarized in Table 5.1. To deliver 2 Gy, cells were incubated with 2.3 MBq in 100 µL DMEM for 1 h, 0.24 MBq in 200 µL for 21 h, or 0.24 MBq in 400 µL for 42 h. To deliver 4 Gy, cells were incubated with 2.3 MBq in 100 µL DMEM for 2 h, 0.46 MBq in 200 µL for 21 h, or 0.46 MBq in 400 µL for 42 h. After incubation with [^{177}Lu]$LuCl_3$, the radioactive medium was removed, and cells were washed three times with PBS. Cells were then trypsinized and reseeded into 6-well plates with six replicates per condition (200 cells for 0 Gy, 400 cells for 2 Gy, and 800 cells for 4 Gy). Cells were allowed to grow for 7 days to form colonies and were subsequently stained with 1% Crystal Violet solution (Merck Sigma). Colonies containing more than 50 cells were counted manually. For each radiation delivery time group, a matched control was cultured in normal medium for the same duration. Plating efficiency was calculated from all matched controls and averaged, and this mean value was used to determine surviving fractions for all irradiated groups, which allows a direct comparison across various conditions.

Table 5.1 *[^{177}Lu]$LuCl_3$ activities and irradiation times for delivering 2 Gy and 4 Gy at different dose rates in 48-well plates*

Dose, Gy	Total activity, MBq	Total volume, µL	Activity per mL	Irradiation time, h	Dose rate, Gy/h
2	2.3	100	23	1	2
	0.23	200	1.2	21	0.1
	0.23	400	0.6	42	0.05
4	2.3	100	23	2	2
	0.46	200	2.3	21	0.2
	0.46	400	1.2	42	0.1

Spheroid growth inhibition

To evaluate the radiosensitizing effect of 5-ALA in spheroids, PIP-PC3 cells were seeded at 1,500 cells per well in 100 µL of complete RPMI containing 2% Matrigel (Corning) in U-bottom, low-attachment 96-well plates (Greiner Bio-One). The plates were centrifuged at 1,300 rpm at 4 °C to promote spheroid formation. Spheroids were allowed to grow for 1 day to reach an average diameter of approximately 350 µm. Cells were then treated with 2 mM 5-ALA for 4 h. After incubation, spheroids were washed three times with fresh complete RPMI and subsequently exposed to 30 kBq, 60 kBq, 120 kBq, or 230 kBq of [^{177}Lu]$LuCl_3$. Cells treated with the same amounts of [^{177}Lu]$LuCl_3$ but without 5-ALA served as comparisons. Fresh complete RPMI was added every 3 days. Images of the spheroids were taken on days 0, 3, 5 and 7 and spheroid diameters were measured using ImageJ. During spheroid size quantification, the diameter was measured from the compact solid region of each spheroid. Low density bright regions observed on day 3 were excluded because they might be attributed to trapped air bubbles in Matrigel rather than cellular structure, and they were no longer observed once the spheroids became denser from day 5 onwards.

Statistical analysis

Data with error bar were presented as mean ± SD. Statistical analyses were performed using either paired t-test or two-way ANOVA as appropriate. GraphPad Prism software (version 8.00) was used for statistical analysis and data visualization. $P < 0.05$ was considered statistically significant.

5.3 Results

As shown in Chapter 4, the radiosensitizing effect of 5-ALA was strongly influenced by the dose rate delivered by ^{90}Y. We therefore investigated its radiosensitization effect in PIP-PC3 cells upon exposure to [^{177}Lu]$LuCl_3$. Similar to ^{90}Y, ^{177}Lu is a β^- emitter, but it has a lower average energy, with a maximum β^- energy of 498 keV and an average energy of 130 keV. The highest dose rate, 2 Gy/h, used here was the same as that applied for ^{90}Y in Chapter 4, and lower dose rates, 0.2 Gy/h to 0.05 Gy/h, were included to reflect clinically relevant conditions.

Clonogenic assay

We performed a clonogenic assay to determine whether the dose-rate effect persisted in long-term cell survival following ^{177}Lu irradiation. The initial dose rates ranged from 2 Gy/h to 0.05 Gy/h. Detailed ^{177}Lu activities and the corresponding absorbed dose and dose rate are

summarized in Table 5.1. As shown in Figure 5.2(a), delivering 2 Gy and 4 Gy at different dose rates resulted in irradiation times ranging from 1 h to 42 h (Table 5.1), and clonogenic plating was initiated immediately after the completion of irradiation for each condition. Representative colony images are presented in Figure 5.2(b).

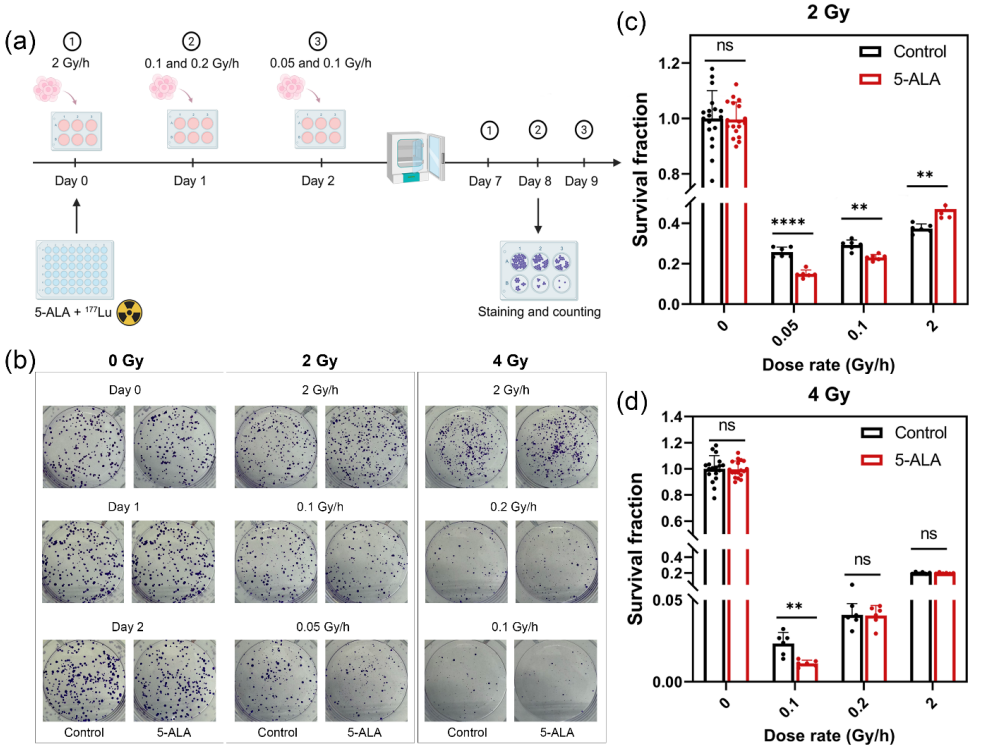

Figure 5.2. Clonogenic assay of the combined treatment of 5-ALA and [^{177}Lu]LuCl$_3$ on PIP PC3 cells. (a) Timescale of the combined treatment. Cells were pretreated with 1 mM 5-ALA, and [^{177}Lu]LuCl$_3$ at various activities was added on day 0. Irradiation at 2 Gy/h was stopped on day 0; irradiation at 0.1 and 0.2 Gy/h was stopped on day 1; irradiation at 0.05 and 0.1 Gy/h was stopped on day 2. Colonies were incubated for a total of 7 days in all groups. (b) Representative colony images. (c) Survival fraction of PIP-PC3 cells after 5-ALA and [^{177}Lu]LuCl$_3$ treatment at 2 Gy. (d) Survival fraction of PIP-PC3 cells after 5-ALA and [^{177}Lu]LuCl$_3$ treatment at 4 Gy. All data are represented as mean ± SD and analyzed by paired t-test; ns indicates no significance, **$p < 0.01$, ****$p < 0.0001$; $n = 6$.

As shown in Figure 5.2(c) and 5.2(d), significant differences in survival fractions were observed among different dose rates. For 2 Gy irradiation, the survival fraction of PIP-PC3 cells treated with [^{177}Lu]LuCl$_3$ increased with increasing dose rate. The survival fractions at 0.1 Gy/h and 2 Gy/h were significantly higher than that at 0.05 Gy/h ($p < 0.05$ and $p < 0.0001$,

respectively). A similar pattern was observed for 4 Gy irradiation, where the survival fractions at 0.2 Gy/h and 2 Gy/h were higher than that at 0.1 Gy/h ($p < 0.01$ and $p < 0.0001$, respectively).

Pre-treatment with 1 mM 5-ALA only, did not show any long-term cytotoxicity to PIP-PC3 cells compared to the control groups. For 2 Gy irradiation, cells pre-treated with 5-ALA showed a significantly lower survival fraction at dose rates of 0.05 Gy/h ($p < 0.0001$) and 0.1 Gy/h ($p = 0.0019$) compared to the groups exposed to [^{177}Lu]$LuCl_3$ alone. For 2 Gy irradiation, cells pre-treated with 5-ALA showed a significantly lower survival fraction at dose rates of 0.05 Gy/h ($p < 0.0001$) and 0.1 Gy/h ($p = 0.0019$) compared to the groups exposed to [^{177}Lu]$LuCl_3$ alone. At the highest dose rate of 2 Gy/h, no radiosensitizing effect of 5-ALA was observed and the survival fraction was found to be slightly higher than the groups exposed to [^{177}Lu]$LuCl_3$ alone ($p < 0.01$). For 4 Gy irradiation, only at the lowest dose rate of 0.1 Gy/h, cells pre-treated with 5-ALA showed a lower survival fraction compared to those receiving irradiation only ($p = 0.0079$), while no significant differences were found at 0.2 Gy/h or 2 Gy/h.

Three-dimensional spheroid growth

After identifying the radiosensitizing effect of 5-ALA in monolayer cells at lower dose rates of ^{177}Lu irradiation, we next evaluated its effect on spheroid growth, which better mimics the tumor microenvironment than 2D cell cultures.[22] The spheroid model was used preliminarily to assess whether the combination of 5-ALA and ^{177}Lu irradiation could suppress spheroid growth, without attempting to control the absorbed dose as done in the viability and clonogenic assays. In these experiments, ^{177}Lu activities of 0.23, 0.12, 0.06, and 0.03 MBq were used.

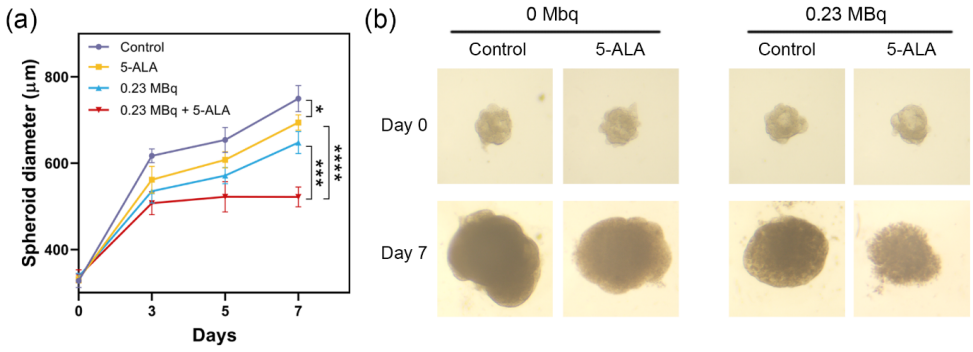

Figure 5.3. Combined treatment of 5-ALA and [^{177}Lu]$LuCl_3$ in 3D spheroid models. (a) Spheroid diameter over time after treatment with 0.23 MBq [^{177}Lu]$LuCl_3$, with or without 2 mM 5-ALA pretreatment. (b) Representative images of spheroids. All data are represented as mean ± SD and analyzed by two-way ANOVA; *$p = 0.019$, ***$p = 0.0001$, ****$p < 0.0001$; $n = 6$.

Figure 5.3(a) shows the effect of 5-ALA pretreatment combined with 0.23 MBq [^{177}Lu]LuCl$_3$ on PIP-PC3 spheroid growth. Pretreatment with 2 mM 5-ALA alone produced a slight growth inhibition from day 3 onward, resulting in a diameter of 694 ± 16 μm on day 7 compared with 749 ± 27 μm in the control group ($p = 0.019$). Treatment with 0.23 MBq [^{177}Lu]LuCl$_3$ significantly inhibited spheroid growth compared with the control group, with a diameter of 647 ± 22 μm on day 7 ($p = 0.0009$). When 2 mM 5-ALA was combined with 0.23 MBq [^{177}Lu]LuCl$_3$, spheroid growth was further suppressed, with a diameter of only 521 ± 21 μm, which was significantly smaller than spheroids treated with [^{177}Lu]LuCl$_3$ alone ($p = 0.0001$). The spheroids in the combination group also stopped growing after day 3. As shown in Figure 5.3(b), clear morphological differences were observed among the treatment groups. Control spheroids maintained a compact structure with smooth, well-defined boundaries, whereas 5-ALA treated spheroids showed slightly reduced compactness, with a dense core and a smooth but lower density outer region. [^{177}Lu]LuCl$_3$ treated spheroids remained spherical with smooth boundaries despite a reduction in size, and similarly displayed a dense core with a lower density outer region. However, spheroids treated with both 5-ALA and [^{177}Lu]LuCl$_3$ showed evidently disrupted structure, with fragmented and irregular boundaries. These spheroids appeared more disintegrated, with loose cells spreading out from a smaller center, indicating that the spheroid structure was breaking down. In the 0.12 MBq + 5-ALA groups, spheroid growth was also reduced compared with 0.12 MBq alone (Fig. S5.1(c)), and a similar disrupted morphology was observed (Fig. S5.1(d)). At lower activities the combined treatment did not significantly inhibit spheroid growth compared to other groups (Fig. S5.1(a) and Fig. S5.1(b)).

5.4 Discussion

In this study, we first investigated the dose rate effect of ^{177}Lu irradiation on the radiosensitizing effect of 5-ALA in PIP-PC3 cells at fixed doses of 2 Gy and 4 Gy (Fig. 5.2). The applied dose and dose rate were determined using a Monte Carlo simulation that incorporated the geometry of the 48 well plate and the medium volume in each well to calculate the absorbed dose per unit activity (Gy/Bq) delivered to the cells. The clonogenic assay results seemed to suggest an inverse dose-rate dependent radiosensitizing pattern of 5-ALA. At both 2 Gy and 4 Gy, a radiosensitizing effect was observed only at dose rates below 0.1 Gy/h, whereas this effect was not evident at dose rates above 0.1 Gy/h (up to 2 Gy/h). This trend differs to some extent from our previous findings in Chapter 4 using external irradiation by ^{90}Y in the same cell line, where

the radiosensitizing effect gradually weakened as the dose rate decreased (from 2 Gy/min to 0.3 Gy/h). Apart from that, an inverse dose-rate effect was also observed when using ^{177}Lu irradiation on its own, with decreasing dose-rate having lower survival of cells (dose rate < 2 Gy/h).

Before discussing the radiosensitizing effect of 5-ALA, we would like to first point out this inverse dose-rate effect. This effect does not agree with the commonly accepted concept of dose-rate sparing, in which the biological response decreases as the dose rate decreases, and therefore a higher dose is needed to achieve the same level of cell killing.[23,24] However, our results are consistent with the findings of Mitchell et al.[25], who reported the same inverse dose rate effect with low dose rates. In their study using ^{60}Co gamma-ray irradiation, PC3, T98G, and A7 cells all showed progressively lower survival as the dose rate decreased below 1 Gy/h. In PC3 cells, this inverse dose-rate effect appeared across all tested doses, including low doses of 2 and 5 Gy. Interestingly, the lowest dose rate of 0.05 Gy/h produced the strongest reduction in survival, whereas higher dose rates (0.1, 0.3, 0.6 and 1 Gy/h) produced progressively weaker effects. This inverse dose rate effect has also been reported in several other studies across different cell lines.[26-28] Although the underlying mechanism remains unclear, two main hypotheses have been proposed. One possibility is that low dose rate irradiation increases the proportion of cells in the G2/M phase, which is relatively radiosensitive.[29-31] The other explanation is the phenomenon of hyper-radiosensitivity, in which very low doses, such as below 0.5 Gy, result in greater cell killing compared with doses above 1 Gy. One mechanistic explanation is that doses in this low range may be insufficient to activate radioprotective repair processes.[32,33] Given the very low dose rates involved in our study, both mechanisms remain possible. Mitchell et al. suggested that hyper-radiosensitivity may contribute to the inverse dose-rate effect in PC3 cells, but further investigation is needed to clarify the dominant mechanism under low dose-rate β^- irradiation.[34]

Returning to the radiosensitizing effect of 5-ALA in PIP-PC3 cells, from a radiation chemistry aspect it is difficult to attribute a clear contribution of the dose rate to the radiosensitizing effect of 5-ALA. Although ROS formation from photosensitizers can arise from interactions between ionized photosensitizer species and water radiolysis products, which may be influenced by dose rate through changes in radical-radical reaction dynamics, the aqueous solution system used to study this mechanism is a simplified model (Chapter 2). It lacks the natural cellular scavengers that compete for reactive intermediates and therefore does not fully represent the complexity of biological conditions. In cells, the radiosensitizing effect of photosensitizers likely results

from the combined contributions of multiple reactive species, including radical cations or anions of the photosensitizer, superoxide, hydroxyl radicals, and singlet oxygen produced by the photosensitizer. However, these reactive species are generated and processed within a highly regulated biological environment. Normal and cancer cells both contain well-defined antioxidant systems such as superoxide dismutase and glutathione, as well as DNA and oxidative damage repair pathways, all of which continuously modulate the balance between damage and repair. As a result, the radiosensitizing effect of photosensitizers is a dynamic process shaped jointly by chemical generation of reactive species and the cellular capacity to counteract or repair the resulting damage.

Despite this complexity, our results suggest that the radiosensitizing effect of 5-ALA might be dependent on the cellular damage response and repair capacity, which is strongly modulated by dose rate. This is reflected in the results that no radiosensitizing effect was observed at the highest dose rate tested with [^{177}Lu]$LuCl_3$ (2 Gy/h), whereas a clear sensitizing effect was present at a much higher dose rate using 1.5 Gy/min X-ray irradiation (250 kV, 1 mm Cu/Al filter) in Chapter 4. The survival fraction of PIP-PC3 cells under X-ray irradiation was nearly half of that observed with [^{177}Lu]$LuCl_3$ at 2 Gy, suggesting better damage management and repair capacity at a dose rate of 2 Gy/h. However, when the dose rate is reduced to a sufficiently low level, as in the 0.1 Gy/h condition in our study, a radiosensitizing effect becomes evident even at a total dose of 2 Gy, and this effect is stronger than that observed at 4 Gy delivered at 2 Gy/h or 0.2 Gy/h, even though ROS generation by photosensitizers is generally considered to be dose dependent (Fig. 5.2). This interpretation is further supported by the spheroid growth results (Fig. 5.3). When examining the effect of ^{177}Lu irradiation alone, only the 0.23 MBq condition produced a significant inhibition of spheroid growth compared with the control groups (Fig. S5.2(a)). Although the growth of the 0.12 MBq group was not significantly reduced compared to control groups (Fig. S5.2(a)), these spheroids displayed an altered morphology, characterized by a small dense core surrounded by a low density outer region, suggesting radiation-induced damage (Fig. S5.1(d)). Consistently, a clear disruption of spheroid structure was observed at activities of 0.23 MBq and 0.12 MBq of [^{177}Lu]$LuCl_3$ when combined with 5-ALA pretreatment, as shown by the growth inhibition and fragmented spheroid boundaries.

It should also be noted that the quantitative relationship between the additional amount of ROS generated by 5-ALA and the final outcome of cell survival remains largely unknown. Although our studies support a dose-dependent increase in ROS produced by the photosensitizer under

ionizing radiation (Chapter 2), it is not clear how much additional ROS is required to shift cells from a surviving state to irreversible loss of clonogenicity, and this threshold is likely to depend on the temporal pattern of dose delivery and on the cellular defense status. In this context, hyper-radiosensitivity may provide a plausible explanation for the increased response observed at very low dose rates. However, the radiosensitizing effect observed at a much higher dose rate of 1.5 Gy/min X ray irradiation does not necessarily need to arise from the same mechanism. At such high dose rates, cells experience a large instantaneous burden of damage, and 5-ALA may contribute by adding further oxidative stress on top of an already compromised repair capacity, thereby pushing the system beyond a tolerable threshold. Thus, low dose rate and high dose rate sensitization may involve different radiobiological routes, but both point to the same underlying concept that the radiosensitizing effect of 5 ALA is strongly dependent on the dynamic radiation sensitivity state of the cells rather than on the absolute amount of ROS alone.

In [^{177}Lu]Lu-PSMA-617 therapy, tumor heterogeneity leads to a wide range of absorbed doses across metastatic lesions, with reported average tumor doses varying from as low as 1.4 to as high as 14.5 Gy/GBq.[35] When considering the physical half-life of ^{177}Lu, the corresponding dose rates fall approximately between 0.05 and 0.47 Gy/h. The dose rates used in our study lie within this clinical range, and the observed inverse dose-rate tendency together with the state-dependent radiosensitizing effect of 5-ALA suggests that photosensitizer-mediated enhancement may occur under the low dose-rate conditions typical of targeted radionuclide therapy.

While these findings suggest a potential role for 5-ALA under low dose-rate conditions, the experimental conditions (*in vitro*) used here do not fully reflect the complexity of the tumor microenvironment *in vivo*. Factors such as heterogeneous perfusion, variable antioxidant capacity, and differences in photosensitizer uptake may influence the extent of radiosensitization in patients. Moreover, this study was conducted using a single prostate cancer cell line (PIP-PC3), which may not present the full range of biological responses across different prostate cancer subtypes. Studies using additional cell lines and more physiologically relevant models will therefore be important to determine the general applicability of these observations. Another technical consideration is that [^{177}Lu]$LuCl_3$ solutions were used directly for irradiation without further chelation. Although several studies have also applied lanthanide chlorides directly in cell culture,[36,37] the presence of phosphate in culture medium may lead to partial precipitation of [^{177}Lu]Lu, potentially affecting the uniformity of dose distribution.[38]

Confirming these results using a chelated form of ^{177}Lu would therefore be valuable to ensure that the observed biological effects are not influenced by precipitation.

5.5 Conclusion

In this study, we examined how dose rate influences the radiosensitizing effect of 5-ALA under ^{177}Lu irradiation in PIP-PC3 cells. An inverse dose-rate pattern of cell survival was observed for [^{177}Lu]$LuCl_3$ at dose rates below 2 Gy/h, and the radiosensitizing effect of 5-ALA was found at dose rate below 0.1 Gy/h, a range that also corresponds to the dose-rate encountered in the clinical application of[^{177}Lu]Lu-PSMA-617. Although the underlying mechanism remains unclear, the inverse dose-rate behavior observed here may be related to hypersensitivity which needs further investigation. The 3D spheroid experiments provided preliminary evidence that combining 5-ALA with ^{177}Lu irradiation can enhance growth inhibition compared with ^{177}Lu alone. Together, these results demonstrate a potential role for 5-ALA as a well-tolerated radiosensitizer in combination with ^{177}Lu-based targeted therapies for metastatic prostate cancer, but further investigation in additional cell models and *in vivo* systems is needed.

References

1 Carles, J., Castellano, D., Climent, M. Á., Maroto, P. *et al.* Castration-resistant metastatic prostate cancer: current status and treatment possibilities. *Clinical and Translational Oncology* **14**, 169-176 (2012).

2 Nakazawa, M., Paller, C. & Kyprianou, N. Mechanisms of Therapeutic Resistance in Prostate Cancer. *Current Oncology Reports* **19**, 13 (2017).

3 Teo, M. Y., Rathkopf, D. E. & Kantoff, P. Treatment of Advanced Prostate Cancer. *Annual Review of Medicine* **70**, 479-499 (2019).

4 Higano, C. S. & Crawford, E. D. New and emerging agents for the treatment of castration-resistant prostate cancer. *Urologic Oncology: Seminars and Original Investigations* **29**, 1-8 (2011).

5 Linder, S., Poel, H. G. v. d., Bergman, A. M., Zwart, W. & Prekovic, S. Enzalutamide therapy for advanced prostate cancer: efficacy, resistance and beyond. *Endocrine-Related Cancer* **26**, R31-R52 (2018).

6 Tannock, I. F., de Wit, R., Berry, W. R., Horti, J. *et al.* Docetaxel plus Prednisone or Mitoxantrone plus Prednisone for Advanced Prostate Cancer. *New England Journal of Medicine* **351**, 1502-1512 (2004).

7 Bono, J. S. d., Logothetis, C. J., Molina, A., Fizazi, K. *et al.* Abiraterone and Increased Survival in Metastatic Prostate Cancer. *The New England journal of medicine* **364**, 1995-2005 (2011).

8 de Bono JS, Oudard S, Ozguroglu M, Hansen S *et al.* Prednisone plus cabazitaxel or mitoxantrone for metastatic castration-resistant prostate cancer progressing after docetaxel treatment: a randomised open-label trial. *Lancet* **376**, 1147-1154 (2010).

9 Paschalis, A., Sheehan, B., Riisnaes, R., Rodrigues, D. N. *et al.* Prostate-specific Membrane Antigen Heterogeneity and DNA Repair Defects in Prostate Cancer. *European Urology* **76**, 469-478 (2019).

10 Sartor, O., De Bono, J., Chi, K. N., Fizazi, K. *et al.* Lutetium-177–PSMA-617 for Metastatic Castration-Resistant Prostate Cancer. *New England Journal of Medicine* **385**, 1091-1103 (2021).

11 Hofman, M. S., Emmett, L., Sandhu, S., Iravani, A. *et al.* Overall survival with [^{177}Lu]Lu-PSMA-617 versus cabazitaxel in metastatic castration-resistant prostate cancer (TheraP): secondary outcomes of a randomised, open-label, phase 2 trial. **25**, 99-107 (2024).

12 Hofman, M. S., Violet, J., Hicks, R. J., Ferdinandus, J. *et al.* [^{177}Lu]-PSMA-617 radionuclide treatment in patients with metastatic castration-resistant prostate cancer (LuPSMA trial): a single-centre, single-arm, phase 2 study. **19**, 825-833 (2018).

13 Violet, J., Sandhu, S., Iravani, A., Ferdinandus, J. *et al.* Long-Term Follow-up and Outcomes of Retreatment in an Expanded 50-Patient Single-Center Phase II Prospective Trial of ^{177}Lu-PSMA-617 Theranostics in Metastatic Castration-Resistant Prostate Cancer. *Journal of Nuclear Medicine* **61**, 857-865 (2020).

14 Ravi Kumar, A. S. & Hofman, M. S. Mechanistic Insights for Optimizing PSMA Radioligand Therapy. *Clincal Cancer Research* **26**, 2774-2776 (2020).

15 Sandhu, S., Guo, C. & Hofman, M. S. Radionuclide Therapy in Prostate Cancer: From Standalone to Combination PSMA Theranostics. *Journal of Nuclear Medicine* **62**, 1660-1668 (2021).

16 Xu, B., Liu, J., Eelkema, R. & Denkova, A. G. Low-dose-rate ionizing radiation increases singlet oxygen production by photosensitizers. *Cell Reports Physical Science* **6**, 102976 (2025).

17 Maesaka, F., Nakai, Y., Yoshida, T., Tomizawa, M. *et al.* 5-Aminolevulinic Acid: A Novel Approach to Improving Radioresistance in Prostate Cancer. *Cancers* **17**, 1286 (2025).

18 Panetta, J. V., Cvetkovic, D., Chen, X., Chen, L., & Ma, C. C. . Radiodynamic therapy using 15-MV radiation combined with 5-aminolevulinic acid and carbamide peroxide for prostate cancer in vivo. *Physics in*

Medicine and Biology **65**, 165008 (2020).

19 Miyake, M., Tanaka, N., Hori, S., Ohnishi, S. *et al.* Dual benefit of supplementary oral 5‐aminolevulinic acid to pelvic radiotherapy in a syngenic prostate cancer model. *The Prostate* **79**, 340-351 (2019).

20 Grkovski, M., Krebs, S. S., O'Donoghue, J. A., Kuten, J. *et al.* Lesion Absorbed Dose–Response Relationship in Patients with Metastatic Castration-Resistant Prostate Cancer Undergoing [^{177}Lu]Lu-PSMA-617 Radiopharmaceutical Therapy. *Journal of Nuclear Medicine* **66**, 1622-1630 (2025).

21 Ells, Z., Grogan, T. R., Czernin, J., Dahlbom, M. & Calais, J. Dosimetry of [^{177}Lu]Lu-PSMA–Targeted Radiopharmaceutical Therapies in Patients with Prostate Cancer: A Comparative Systematic Review and Metaanalysis. *Journal of Nuclear Medicine* **65**, 1264-1271 (2024).

22 Doctor, A., Seifert, V., Ullrich, M., Hauser, S. & Pietzsch, J. Three-Dimensional Cell Culture Systems in Radiopharmaceutical Cancer Research. *Cancers* **12**, 2765 (2020).

23 Steel, G. G., Down, J. D., Peacock, J. H. & Stephens, T. C. Dose-rate effects and the repair of radiation damage. *Radiotherapy and Oncology* **5**, 321-331 (1986).

24 Dale, R. G. Dose-rate effects in targeted radiotherapy. *Physics in Medicine & Biology* **41**, 1871-1884 (1996).

25 Carlsson, J., Håkansson, E., Eriksson, V., Grawe, J. *et al.* Early Effects of Low Dose-Rate Radiation on Cultured Tumor Cells. *Cancer Biotherapy and Radiopharmaceuticals* **18**, 663-670 (2003).

26 DeWeese TL, Shipman JM, Dillehay LE & WG., N. Sensitivity of human prostatic carcinoma cell lines to low dose rate radiation exposure. *The Journal of urology* **159**, 591-598 (1998).

27 Marin, L. A., Smith, C. E., Langston, M. Y., Quashie, D. & Dillehay, L. E. Response of glioblastoma cell lines to low dose rate irradiation. *International journal of radiation oncology, biology, physics* **21**, 397-402 (1991).

28 Furre, T., Koritzinsky, M., Olsen, D. R. & Pettersen, E. O. Inverse dose-rate effect due to pre-mitotic accumulation during continuous low dose-rate irradiation of cervix carcinoma cells - PubMed. *International journal of radiation biology* **75**, 699-707 (1999).

29 Fowler, J. F. Radiobiological aspects of low dose rates in radioimmunotherapy. *International journal of radiation oncology, biology, physics* **18**, 1261-1269 (1990).

30 Vilenchik, M. M., Alfred G. Knudson, J., Vilenchik, M. M. & Knudson, A. G. Inverse radiation dose-rate effects on somatic and germ-line mutations and DNA damage rates. *Proceedings of the National Academy of Sciences* **97**, 5381-5386 (2000).

31 Barnard, S. G. R., McCarron, R., Moquet, J., Quinlan, R. *et al.* Inverse dose-rate effect of ionising radiation on residual 53BP1 foci in the eye lens. *Scientific Reports* **9**, 10418 (2019).

32 Wykes, S. M., Piasentin, E., Joiner, M. C., Wilson, G. D. & Marples, B. Low-dose hyper-radiosensitivity is not caused by a failure to recognize DNA double-strand breaks. *Radiation research* **165**, 516-524 (2006).

33 Joiner, M. C., Marples, B., Lambin, P., Short, S. C. & Turesson, I. Low-dose hypersensitivity: current status and possible mechanisms. *International Journal of Radiation Oncology, Biology, Physics* **49**, 379-389 (2001).

34 Mitchell, C. R., Folkard, M., Joiner, M. C., Mitchell, C. R. *et al.* Effects of Exposure to Low-Dose-Rate ^{60}Co Gamma Rays on Human Tumor Cells In Vitro. *Radiation Research* **158**, 311-318 (2002).

35 Jackson, P., Hofman, M., McIntosh, L., Buteau, J. P. & Kumar, A. R. Radiation Dosimetry in ^{177}Lu-PSMA-617 Therapy. *Seminars in Nuclear Medicine* **52**, 243-254 (2022).

36 Gholami, Y. H., Willowson, K. P., Forwood, N. J., Harvie, R. *et al.* Comparison of radiobiological parameters for ^{90}Y radionuclide therapy (RNT) and external beam radiotherapy (EBRT) in vitro. *EJNMMI Physics* **5**, 18

(2018).

37 Wallimann, R. H., Mehta, A., Mapanao, A. K., Köster, U. *et al.* Preclinical comparison of (radio)lanthanides using mass spectrometry and nuclear imaging techniques: biodistribution of lanthanide-based tumor-targeting agents and lanthanides in ionic form. *European Journal of Nuclear Medicine and Molecular Imaging* **52**, 1370-1382 (2025).

38 Liu, H., De Kruijff, R. M., Laan, A. C., Beekman, F. J. *et al.* Efficient Radiolabeling of Block Copolymer Micelles through Radiometal Salt Precipitation for Theranostic Applications. *Advanced Therapeutics* **5**, 2200077 (2022).

Supporting information

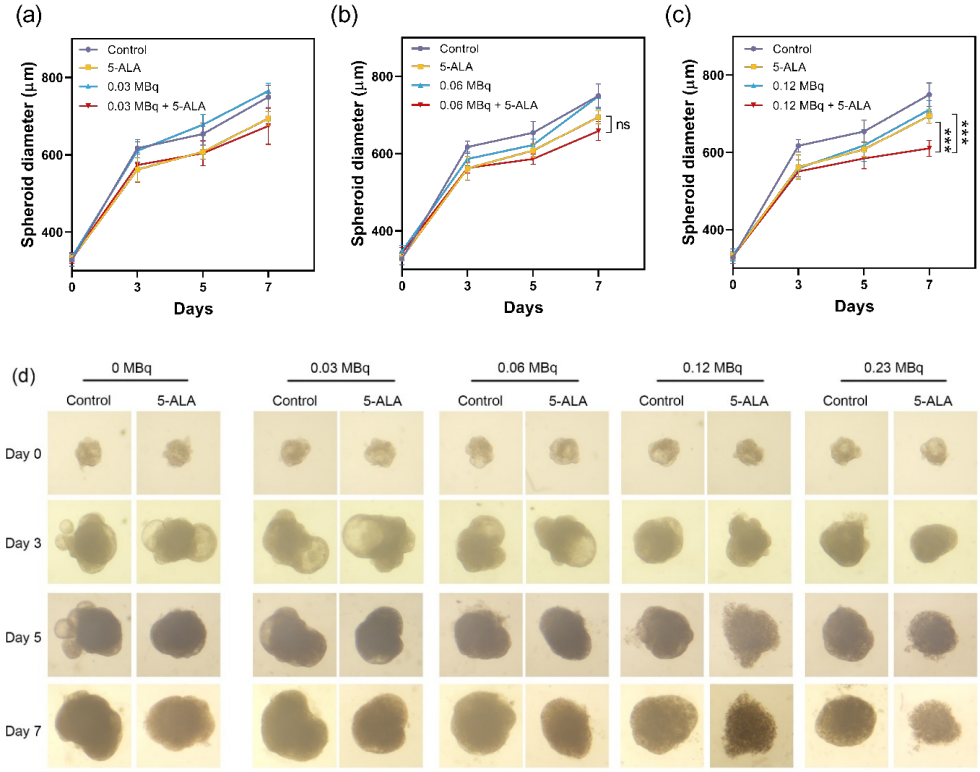

Figure S5.1. Combined treatment of 2 mM 5-ALA and ^{177}Lu in 3D spheroid models. (a) 0.03 MBq ^{177}Lu. (b) 0.06 MBq ^{177}Lu. (c) 0.12 MBq ^{177}Lu. (d) Representative spheroids images taken by light microscopy. All data are represented as mean ± SD and analyzed by two-way ANOVA; ns indicates no significance, ***p = 0.0005; n = 6.

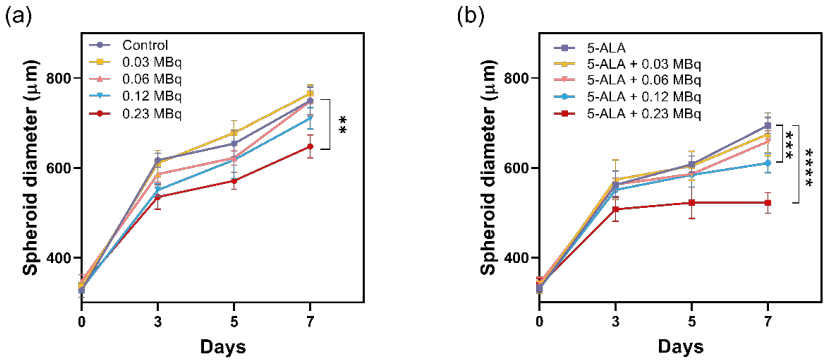

Figure S5.2. The influence of ^{177}Lu irradiation with or without 2 mM 5-ALA treatment in 3D spheroid models. (a) ^{177}Lu irradiation without pretreatment of 5-ALA. (b) ^{177}Lu irradiation. (c) 0.12 MBq ^{177}Lu irradiation with pretreatment of 5-ALA. All data are represented as mean ± SD and analyzed by two-way ANOVA; **p = 0.0013, ***p = 0.0008, ****p < 0.0001; n = 6.

Chapter 6

Conclusion and outlook

This research focuses on understanding how photosensitizers (PSs) produce reactive oxygen species (ROS), specifically singlet oxygen ($^1O_2$), under ionizing radiation. We examined two commonly proposed ideas about how photosensitizers are activated under ionizing radiation. The first is whether Cerenkov light produced during irradiation plays an important role in singlet oxygen generation by PSs. The second is whether PS activation occurs through excitation by Auger or secondary electrons. We also evaluated the PS's radiosensitizing potential *in vitro* using different radiation therapy modalities to help optimize eventual clinical application. Hereby, we focused on establishing how dose rate influences therapeutic efficacy.

Based on our previous findings that photosensitizer Chlorin e6 (Ce6) can produce $^1O_2$ in aqueous solutions upon X-ray or gamma-ray irradiation[1,2], we then used Ce6 to study its $^1O_2$ formation mechanism under ionizing radiation exposure in Chapter 2. Using X-ray and gamma-ray irradiation (0-20 Gy) combined with SOSG and imidazole/RNO detection methods, we demonstrated dose-dependent $^1O_2$ production by Ce6 in aqueous solutions. Our findings established that Cerenkov light is not essential for this process. The dose rate dependence of $^1O_2$ production (maximal at 0.005 Gy/min) and its complete elimination by superoxide dismutase (the scavenger of superoxide anions ($\cdot O_2^-$)) demonstrate that $^1O_2$ formation most probably proceeds through Ce6 interacting with radiation-generated $\cdot O_2^-$. Thus, we propose that ionizing radiation generates Ce6 radical cations, which have sufficient oxidation potential to oxidize $\cdot O_2^-$ to $^1O_2$. This work has, however, several limitations. First, we studied only Ce6, which may not be representative of all photosensitizers. The oxidation of $\cdot O_2^-$ to $^1O_2$ requires a relatively high oxidation potential. Photosensitizers such as porphyrins and chlorins are expected to reach such potentials, but many metal-based photosensitizers are designed with smaller energy gaps for more efficient triplet-mediated $^1O_2$ generation and may consequently have lower oxidation potentials. Testing these metal-based photosensitizers under ionizing radiation would help determine whether the $\cdot O_2^-$ mediated pathway is broadly applicable and distinguish ionization-driven mechanisms from triplet state-driven ones. Second, $^1O_2$ was detected only by indirect probes rather than by direct observation. More direct techniques such as electron paramagnetic resonance (EPR) spectroscopy and pulse radiolysis are needed to further verify the mechanism since the radical cation form of photosensitizers have very short lifetimes.

In Chapter 3, we further evaluated whether Auger electrons or low energy electrons could excite Ce6 by using iodine-125 (^{125}I) as the radiation source. Ce6 was positioned in the region of Auger and secondary electron emission by conjugating it close to ^{125}I on gold nanoparticles,

yet no cell-killing effect was observed. In contrast, a pronounced cell killing efficiency appeared when ^{125}I-labeled nanoparticles were simply mixed with Ce6. These results indicate that direct excitation of Ce6 by low-energy electrons is unlikely. We also observed that ^{125}I-labeled AuNPs produced a stronger cell killing effect than simply [^{125}I]NaI when both were mixed with Ce6. This suggests that AuNPs may enhance the effect of ^{125}I by depositing more energy into the surrounding medium, potentially promoting Ce6 ionization or increasing the formation of reactive species such as $\cdot O_2^-$. Further studies are needed to identify which ROS are primarily responsible for the observed effects. It is also possible that Auger electrons may damage Ce6 when the molecules are positioned too close to ^{125}I, which could be tested by monitoring $^1O_2$ formation from Ce6-conjugated ^{125}I-labeled AuNPs under light exposure. Simulations of Auger and photoelectron dose distributions, along with the resulting radical formation could further clarify which processes contribute most to the Ce6 activation and the resulting cytotoxicity.

Since we found that dose rate is relevant for the interaction of photosensitizers with ionizing radiation, we next examined how dose rate influences their behaviour as radiosensitizers *in vitro* in Chapter 4 and 5, with potential application in brachytherapy or radionuclide therapy. Considering the poor targeting ability of Ce6, we used 5-aminolevulinic acid (5-ALA), a precursor of protoporphyrin IX that can selectively accumulate in tumor cells lacking transferrin. In Chapter 4, dose rates from 2 Gy/h down to 0.3 Gy/h were delivered using a yttrium-90 foil. The radiosensitizing effect of 5-ALA was first confirmed in both U87 and PIP-PC3 cells under X-ray irradiation (250 kV) at a dose rate of 1.5 Gy/min. When we switched to β^- irradiation using [^{90}Y]Y foil, the radiosensitizing effect was still present at around 2 Gy/h, but it gradually diminished as the dose rate decreased further and eventually disappeared. In Chapter 5, we used [^{177}Lu]$LuCl_3$ to deliver even lower dose rates ranging from 2 Gy/h down to 0.05 Gy/h in combination with 5-ALA pretreatment on PIP-PC3 cells. However, we observed an inverse radiosensitizing effect of 5-ALA at these low dose rates. This radiosensitizing effect began to appear at 0.1 Gy/h for both 2 Gy and 4 Gy total doses, and at 0.05 Gy/h for the 2 Gy, while no radiosensitizing effect was observed at higher dose rates of 0.2 Gy/h or 2 Gy/h for either 2 Gy or 4 Gy. We also tested the combined treatment at selected activity levels in 3D spheroids, and preliminary results showed a suppression of tumor growth. Taken together, these findings demonstrate that 5-ALA has potential as a radiosensitizer in brachytherapy and radionuclide therapy, but its effectiveness depends strongly on dose rate. Dose rate seems to influence how cells sense and deal with radiation-induced damage, which

in turn affects whether the additional damage introduced by photosensitizers can be fully expressed. A more systematic investigation of the dose-rate survival response of prostate cancer cells, together with measurements of intracellular ROS under different dose rates in the presence of photosensitizers, would help clarify these relationships. Further validation in 3D spheroid models and in vivo studies is also required to evaluate how dose rate affects the radiosensitizing effect of 5-ALA.

References

1 Liu, H., Carter, P. J. H., Laan, A. C., Eelkema, R. & Denkova, A. G. Singlet Oxygen Sensor Green is not a Suitable Probe for $^1O_2$ in the Presence of Ionizing Radiation. *Scientific Report* **9**, 8393 (2019).

2 Liu, H., Laan, A. C., Plomp, J., Parnell, S. R. *et al.* Ionizing Radiation-Induced Release from Poly(ε-caprolactone-b-ethylene glycol) Micelles. *ACS Applied Polymer Materials* **3**, 968-975 (2021).

LIST OF PUBLICATIONS

Publications related to this thesis:

Xu, B., Liu, J., Eelkema, R. & Denkova, A. G. Low-dose-rate ionizing radiation increases singlet oxygen production by photosensitizers. *Cell Reports Physical Science* **6**, 102976 (2025).

Xu, B., Eelkema, R., Denkova, A. G. In Vitro Characterization of the Radiosensitizing Effects of 5-Aminolevulinic Acid as a Function of Dose Rate, in preparation.

Xu, B., Liu, H., Wang, R., Eelkema, R., Denkova, A. G. Radiodynamic Therapy Using Iodine-125 and Chlorin e6: Impact of Gold Nanoparticles and Component Conjugation, in preparation.

Xu, B., Chatzipapas, K., Eelkema, R., Denkova, A. G. 5-Aminolevulinic Acid Enhances the Therapeutic Effect of Lutetium-177 in Prostate Cancer, in preparation.

Other publications:

Liu, J.*, **Xu, B.***, de Geus, M. A. R., Denkova, A. G., Eelkema, R. Organochloride mediated prodrug activation induced by ionizing radiation. *Chemical Science* **17**, 1752-1760 (2026)

Liu, H., **Xu, B.**, Chen, L., Li, X., Li, H., Liang, J., Bai, Y., & Wang, M. Preparation and Characterization of Chlorin e6-Conjugated Au Nanoparticles as the Radiosensitizer for Enhanced Radiotherapy. *ACS Omega* **11**, 439–448 (2026)

Oral presentations:

Xu, B., Eelkema, R. & Denkova, A. G. Mechanistic insights into the into photosensitizer activation by ionizing radiation for enhanced radiotherapy. 33rd Miller Conference on Radiation Chemistry, Dubrovnik, Croatia, 2025.

Posters:

Xu, B., Eelkema, R. & Denkova, A. G. Investigating the $^1O_2$ generation of photo-active substances exposed to different types of ionizing radiation. 9th International Symposium on Space Radiation and Particle Radiotherapy, Suzhou, China, 2024

Xu, B., Eelkema, R. & Denkova, A. G. Investigating the mechanism behind the radiation-induced photochemical properties of photoactive substances. 19th Radiochemical Conference, Czech Technical University, Czech, 2021

ACKNOWLEDGEMENT

My PhD journey began four years ago. I still remember the day I arrived in the Netherlands, stepping into a new environment on my own, both uncertain and curious about what lay ahead. Over the past four years, it has offered me more than I had expected. I met wonderful friends, worked with good colleagues and was guided by great promoters. I feel truly lucky to have ended up in this place, and I would like to express my gratitude to everyone who guided and encouraged me along the way.

First, I would like to thank the **China Scholarship Council** (CSC) for supporting my PhD studies over the past four years in the Netherlands. I am also grateful to **TU Delft** and the **Reactor Institute Delft** for providing an open and stimulating research environment.

I would like to express my sincere gratitude to my promoter and daily supervisor, **Prof.dr.ir. Antonia G. Denkova**, for your guidance and support throughout this journey. Coming from a different background, I deeply appreciated the patience, time, and freedom you gave me to adjust to a new field, learn step by step, and gradually find my place in the research. Throughout my PhD, you provided invaluable help in many aspects of my work. Despite your busy schedule, you consistently made time for weekly meetings, during which we could discuss my progress in detail. You gave me insightful suggestions for experiments and analysis, guided me in interpreting results, and supported me through countless rounds of revisions during the publication process. Whenever I felt lost in the research, you always helped me regain clarity by discussing the problems with me in detail and guiding me patiently toward a clear direction. At the same time, you are also a warm and supportive person, who has always offered me great care and encouragement, especially during difficult moments. Your support gave me the strength to move forward when things felt overwhelming. I am truly grateful for everything I have learned from you and for all your support along the way.

I would also like to express my sincere thanks to my other promoter, **Prof.dr. Rienk Eelkema**, for all discussions on our projects. In our meetings, you consistently demonstrated clear and structured thinking, and your thought-provoking questions often led me to deeper reflection. I still remember a conversation during my first yearly progress meeting, when you asked me whether I saw myself pursuing a career in research. At the time, I said that I did not think I was suited for it and listed many reasons to support that view. However, you pointed out that most of the difficulties I mentioned could be overcome through learning and experience. This conversation has stayed with me ever since. It made me realize that I often focused too much

on my limitations, rather than considering what I could achieve through effort and growth. I am very grateful for this perspective, which has had a lasting impact on how I approach challenges.

I am grateful to the members of my **committee** for the time and careful evaluation of my thesis, as well as to all those who contributed to this work by providing materials, technical support, and valuable assistance. In particular, I would like to thank **Dr. Julie Nonnekens**, **Dr. Jeroen Essers**, **Rob Verhagen**, and **Nicole Verkaik** from Erasmus MC. Julie and Jeroen, thank you for providing the PIP-PC3, PC3, and HeLa cell lines. Rob and Nicole, thank you for your help in preparing and handling the cells. This work would not have been possible without your contributions. I would like to thank the team at HollandPTC for your support during my experiments. I am especially grateful to **Ernst van der Wal** for helping design the experimental setup, making the work possible, and to **Thomas Toet** for the patient assistance during the irradiation experiments, often carried out in the dark and late hours. I also thank **Dr. Anggraeini Puspitasari-Kokko** for the help with biological laboratory practices and for always being willing to help when needed. You all made the experience particularly pleasant. My thanks also go to **Prof.dr. A. M. Brouwer** from the University of Amsterdam for discussions on the photosensitizer project. I am also grateful to **Tim Beets** for making it possible to manually switch off the lights in the Bio-lab, which greatly helped my experiments.

I want to thank all the colleagues from ARI group. **Konstantinos**, your expertise in Monte Carlo simulations came at exactly the right moment, when I was in great need of it. Your help in calculating the energy deposition was essential to this part of my thesis, and I truly appreciate your support. I also enjoyed working with you on the bachelor student project. **Robin**, I really appreciate your help during the long holiday period in my first year, which basically saved my cell experiments. I am also very grateful for how you always made conversations feel easy and enjoyable for everyone. **Kristina**, thank you for your kindness and for bringing us together on many occasions. I especially enjoyed watching Eurovision together. **Astrid**, thank you for taking good care of the biological lab, where most of my experiments were carried out. I really appreciate all your help with ordering materials, looking after the cells, taking images of the spheroids, and performing the irradiation. **Baukje**, thank you for introducing me to the lab at the very beginning. I really appreciate all your help in setting up the amazing dark room, performing the irradiation, ICP and INNA measurements. I also still remember the time we went on a roller coaster together, which will always remain a special memory to me. **Eline and Folkert**, thank you for having shared the office with me and for helping me practice my English.

Eline, thank you for teaching me how to run column chromatography, and Folkert, for often helping me with technical issues on the lab computers. **Özlem**, thank you for your support and assistance in the lab. To everyone from **SBE**, especially **Henk**, **Misja**, **Marcel** and **Martijn**, thank you for your help with IT issues and for all the discussions that helped make my plans possible. I would like to thank **Kristen** from the PPE group for assisting me with confocal imaging. I appreciate your help in providing me with cover slips when I ordered the wrong one. I also want to thank **Sietse Kuipers** from the ASM group for guiding me in the use of FT-IR and the zeta sizer. Thanks to the **BSc** and **MSc** students I supervised for their contributions.

Next, I would like to thank all the past and present PhDs and postdocs I met. **Guanglin Wang**, I would like to start by thanking you, as I would not have had the opportunity to come here without you. **Juncheng**, it has been a great pleasure working with you. Your expertise in chemistry has been very helpful to my work, and I really appreciated our many discussions and your valuable suggestions. I would also like to thank your wife **Jiechen** for her positive energy, which always brought everyone together. **Huanhuan**, your enthusiasm has always been inspiring, and I have gained a lot from our interactions. I also really appreciate your helpful suggestions on the synthesis of gold nanoparticles. **Runze**, I really appreciate your patience and all the help you gave me with my experiments. I also thank you for sharing many useful papers related to my research. **Chao,** thank you for subletting your room to me and giving me a place to call home in Delft. **Mark**, **Hu, Alexandra, Svenja, Robin N, Rogier, Vasileios**, thanks for always being great colleagues and offered me valuable help when I needed. **Gauri**, I really appreciate how supportive and easy-going you have been. You were always there when I needed help in the lab, and you also helped me with TEM imaging. I also really enjoyed the time we spent learning swimming together and the Indian food you shared. Thank you for always being so caring, for listening to me when I needed it, and for your encouragement. **Qi**, thank you for sharing so much helpful information when I first arrived and for guiding me through the start of my PhD and life in the Netherlands. I also really appreciate your help in the lab, especially with the TEM imaging. **Esther**, thank you for correcting my Dutch summary one word by one word. **Marouscha**, thank you for taking us sailing. It was my first time, and I really enjoyed it and learned a lot. **Yirong**, thank you for being such a great gym partner. You always encouraged me to join you for workouts and kept me motivated to stay active and maintain a healthier routine. I also hope you take good care of yourself and remember to eat well. I have truly enjoyed working with you all, and I wish you all the best in the future.

These years have also brought me many wonderful friendships. The first person I want to thank

is **Xu Shan**. I still remember that you were the first person I met when I arrived in the Netherlands, and also my housemate. You opened the door for me at four in the morning when I first arrived. You also took me to the supermarket, showed me around the university, and shared so much useful information about living here. I am truly grateful for your kindness and thoughtfulness. You also introduced me to the second person I would like to thank, **Yueer**. I was very lucky that we both work in the reactor. You showed me around the city center, treated me to fries, and invited me to your home for dinner. All of this made the new place feel warmer and more familiar to me. **Qiangrui**, somehow you became the person I felt closest to here. You were always there for me when I needed support, and you have a way of bringing lightness and joy into everything. We shared so many moments together, from everyday conversations to small trips, and I truly value all of them. I also want to thank your husband **Ju Zheng,** for the wonderful driving trip we had together. I feel very lucky that our paths crossed here. **Mahmoud** and **Selvi**, thank you for inviting us to your home for hot pot. I also really appreciate how you always listened so attentively and helped me relax when I was under stress. **Marco**, thank you for sharing the wild goose meat. **Min Li**, thank you for being such a reliable neighbor and for always being willing to help. **Justin**, thank you for sharing the snacks from Taiwan. **Wencan**, **Guofeng**, **Lifei**, **Jianxin**, **Kai** and **Hang**, it has been really nice knowing you. The times we spent playing badminton, cards, and Avalon were always full of laughter. **Mengjie**, I would also like to thank you especially for the cakes you brought to our gatherings, which were honestly the best I have had in Delft. **Zhaojiang**, **Changchun**, **Chaofan**, **Yifan**, **Qi Shen**, **Ziying**, and **Na**, it has been really nice knowing you. I would also like to thank my friends in China, **Biting**, **Yan Zhou**, **Yunfan**. Although we are far apart, your companionship has never been absent. I wish you all a wonderful future.

I also met someone very important in my life here, my fiancé, **Shihao Fu**. Being with you has brought so much joy and color into my life. You have taken such good care of me, and I am deeply grateful for your constant love and support. You have also supported me in my studies, patiently helping me work through problems and reminding me to stay on track when I tended to procrastinate. Over time, you have helped me grow and become a better version of myself. Thank you for everything you have done for me.

最后，我要感谢我的家人们对我的支持和陪伴。尤其是我的母亲，**夏建勤**。感谢你多年来的辛勤付出，为我创造了稳定的生活基础，让我可以没有后顾之忧地走向更远的世界。也是你一直在背后默默守护，让我有勇气去尝试、去选择自己的方向。没有你，就不会有今天的我。

CURRICULUM VITAE

Bing Xu was born in 1995 in Suzhou, China. After graduating from high school, she enrolled in Xuzhou Medical University in 2013, where she studied Medical Imaging. After five years of study, she obtained her medical degree in 2018. In the same year, she was admitted to Soochow University to pursue a Master's degree in Radiation Medicine. Her research focused on how radiation-responsive tumor proteins modulate radiosensitivity and the underlying mechanisms. She obtained her Master's degree in 2021. Subsequently, she joined the groups of Prof.dr.ir. A. G. Denkova and Prof.dr. R. Eelkema at TUDelft in 2021. Her research focused on the activation mechanisms of photosensitizers by ionizing radiation and their application as radiosensitizers in radiotherapy.


N
NH
HN
N
O
OH
O
OH